

UNIVERSITY OF WOLLONGONG

DOCTORAL THESIS

---

## Thesis Title

---

*Author:*  
Jesse GREENSLADE

*Supervisor:*  
Dr. Jenny FISHER

*A thesis submitted in fulfilment of the requirements  
for the degree of Doctor of Philosophy  
in the*

**Center for Atmospheric Chemistry  
Department of Chemistry**

October 19, 2016



# **Declaration of Authorship**

I, Jesse GREENSLADE, declare that this thesis titled, "Thesis Title" and the work presented in it are my own. I confirm that:

- This work was done wholly or mainly while in candidature for a research degree at this University.
- Where any part of this thesis has previously been submitted for a degree or any other qualification at this University or any other institution, this has been clearly stated.
- Where I have consulted the published work of others, this is always clearly attributed.
- Where I have quoted from the work of others, the source is always given. With the exception of such quotations, this thesis is entirely my own work.
- I have acknowledged all main sources of help.
- Where the thesis is based on work done by myself jointly with others, I have made clear exactly what was done by others and what I have contributed myself.

Signed:

---

Date:



*“Thanks to my solid academic training, today I can write hundreds of words on virtually any topic without possessing a shred of information, which is how I got a good job in journalism.”*

Dave Barry



UNIVERSITY OF WOLLONGONG

*Abstract*

Chemistry  
Department of Chemistry

Doctor of Philosophy

**Thesis Title**

by Jesse GREENSLADE

The Thesis Abstract is written here (and usually kept to just this page). The page is kept centered vertically so can expand into the blank space above the title too...



## *Acknowledgements*

The acknowledgements and the people to thank go here, don't forget to include your project advisor...

Thanks to my supervisor Jenny Fisher, the whole Atmospheric Chemistry team at Wollongong who made me feel at home: Clare Murphy, Dagmar, Elise, Joel, Kaitlyn, Max, Nick Deutcscher, Nick Jones, Stephen Wilson,

Thanks also to my personal saviour and his noodly appendages.



# Contents

<b>Declaration of Authorship</b>	iii
<b>Abstract</b>	vii
<b>Acknowledgements</b>	ix
<b>1 Background</b>	1
1.1 What are Volatile Organic Compounds (VOCs)? . . . . .	1
1.2 Natural gas and aerosol emissions in Australia . . . . .	1
1.2.1 Australia . . . . .	1
1.2.2 Satellite Measurements . . . . .	2
1.3 Isoprene . . . . .	2
1.3.1 Structure . . . . .	2
1.3.2 Sources and Sinks . . . . .	2
1.3.3 Isoprene From HCHO . . . . .	3
1.3.4 Measurements . . . . .	5
1.3.5 Estimates . . . . .	5
1.3.6 Radiative Forcing . . . . .	6
1.4 Formaldehyde . . . . .	6
1.4.1 Structure . . . . .	6
1.4.2 Sources and sinks . . . . .	6
1.4.3 Measurements . . . . .	6
1.5 Dust . . . . .	6
1.6 Models . . . . .	7
1.6.1 Chemical Transport Models . . . . .	7
1.6.2 GEOS-Chem . . . . .	8
1.7 Satellites . . . . .	9
1.7.1 Useful satellites . . . . .	9
1.7.2 Comparisons with Models . . . . .	10
1.7.3 DOAS . . . . .	10
<b>2 Stratosphere to Troposphere Transport of ozone</b>	11
2.1 Background . . . . .	11
2.1.1 Historical estimates . . . . .	11
2.1.2 Tropospheric production . . . . .	11
2.1.3 Stratosphere to Troposphere ozone Transport (STT) . . . . .	13
2.2 Instruments and data sets . . . . .	14
2.2.1 Atmospheric Infrared Sounder (AIRS) . . . . .	14
2.2.2 Sondes . . . . .	14
2.2.3 European Centre for Medium-Range Weather Forecasts (ECMWF) Re-Analysis - Interim data set (ERA-I) . . . . .	14
2.3 STT Detection . . . . .	15
2.3.1 Aim . . . . .	15

2.3.2	Tropopause Heights . . . . .	15
2.3.3	Fourier bandwidth (or bandpass) Filtering . . . . .	15
2.3.4	Bandwidth filter applied to ozonesondes . . . . .	16
2.3.5	Case Studies . . . . .	18
2.3.6	Site summaries . . . . .	18
2.4	Stratosphere to Troposphere flux analysis . . . . .	21
2.4.1	Determining a minimum estimate of stratospheric influence . . . . .	21
2.5	Non-STT influences on ozone at southern latitudes . . . . .	23
2.5.1	Fire Plumes . . . . .	23
2.5.2	Transport Exclusion . . . . .	24
2.6	GEOS-Chem ozonesonde comparison . . . . .	24
2.6.1	Comparing data to GEOS-Chem . . . . .	24
2.6.2	Determining tropospheric ozone from GEOS-Chem . . . . .	26
2.6.3	Ozone profiles compared with GEOS-Chem . . . . .	27
2.6.4	Estimation of southern ocean STT flux . . . . .	39
<b>3</b>	<b>Isoprene Emissions in Australia</b>	<b>41</b>
3.1	Australian Biogenic Volatile Organic Compounds (BVOCs) . . . . .	41
3.1.1	Isoprene, Monoterpenes . . . . .	41
3.1.2	Products and HCHO yield . . . . .	41
3.1.3	Biomass Burning . . . . .	42
3.1.4	MEGAN . . . . .	43
3.2	Satellite HCHO measurements . . . . .	43
3.2.1	Satellite Retrievals . . . . .	43
3.2.2	OMI Algorithm (not DOAS) . . . . .	45
3.2.3	Optical Depth ( $\tau$ ) . . . . .	46
3.2.4	Scattering . . . . .	46
3.2.5	Absorption cross section and number density . . . . .	46
3.2.6	Air Mass Factors . . . . .	47
3.2.7	OMI HCHO data products . . . . .	47
3.2.8	HCHO Vertical Column Calculation . . . . .	47
3.2.9	Reference sector correction for comparison of products to various models . . . . .	50
3.3	Creating a top-down isoprene inventory . . . . .	50
3.3.1	Process Outline . . . . .	50
3.3.2	Quality filtering OMI HCHO slant columns . . . . .	52
3.3.3	Reading OMHCHO daily slant columns . . . . .	54
3.3.4	Regridding to 0.25 by 0.3125 8-day averaged vertical columns . . . . .	54
3.3.5	Filtering pyrogenic HCHO . . . . .	55
3.3.6	Filtering anthropogenic HCHO . . . . .	55
3.3.7	Recalculating the AMF to create our own vertical HCHO columns . . . . .	55
3.3.8	Determining and applying the pacific ocean reference sector normalisation . . . . .	59
3.3.9	Determining S, the isoprene emissions . . . . .	62
3.3.10	Extrapolating the circadian cycle . . . . .	62
3.3.11	Comparison with MEGAN . . . . .	62
3.3.12	Comparison with in-situ measurements . . . . .	62
3.4	Model comparison with and without satellite HCHO based inventory . . . . .	62
<b>Bibliography</b>		<b>63</b>

# List of Figures

1.1	Part of a figure from Guenther et al., (2006) showing global isoprene emission factors. . . . .	4
1.2	Standard box model parameters, image taken from Jacob, (1999). . . . .	8
1.3	An example spectrum showing interferences used for species concentration measurements by GOME-2. Image by EUMETSAT and ESA (EU-METSAT, 2015). . . . .	9
2.1	NEPM standards taken from National Environment Protection Council annual report 2012-2013 (Environment and the National Environment Protection Council), 2015). . . . .	12
2.2	Monthly mean tropopause altitudes (minimum of lapse-rate and ozone defined tropopauses). Dashed lines show 'event only' seasonal tropopause altitudes. . . . .	16
2.3	Seasonally averaged ozone over Davis, Macquarie, and Melbourne measured by ozonesondes. Black solid lines show seasonal tropopause heights. . . . .	17
2.4	(a) An ozone profile between 2km altitude and the tropopause (indicated by the dashed vertical line). The 'flux' area shows the estimate of stratospheric impact on tropospheric ozone. (b) The 99th percentile of filtered ozone perturbations (green dashed line) and the technique for determining the vertical extent of the 'event' (red dashed and solid lines). . . . .	19
2.5	Vertical profiles show ozone ppbv (black line), relative humidity (blue line), and temperature (red line) for (a) 3 February 2005 and (c) 13 January 2010. Synoptic weather maps show the 500 hPa pressure level taken from the ERA-Interim reanalysis on (b) 3 February 2005 and (d) 13 January 2010. Vectors show wind direction and speed while the colour indicates the geopotential height. Also visible are the line contours of potential vorticity units, 1 PVU in purple and 2 PVU (often used to determine dynamical tropopause height) in white. . . . .	20
2.6	The climatology of STT events at Melbourne: (A) Events sorted by month from the entire Melbourne ozonesonde dataset. The events filtered out as possibly smoke plume influenced are indicated in red. (B) The occurrence distribution of the ozone peak altitude. (C) The distance between the ozone peak and the tropopause (bars) and the cumulative probability function of these distances (blue line). . . . .	21
2.7	As for Figure 2.6 except showing the Macquarie Island STT events. . . . .	22
2.8	As for Figure 2.6 except showing the Davis STT events. . . . .	22
2.9	Fraction of total tropospheric column ozone attributed to stratospheric air intrusions during STT events. Error bars indicate one standard deviation. . . . .	23
2.10	AIRS total column CO image showing two days separate days of swathes. The top panel shows an example of an excluded ozone event which could have been caused by a transported biomass burning plume on October 17th, 2007. . . . .	25

2.11 Tropospheric ozone in molecules $\text{cm}^{-2}$ every six hours simulated by GEOS-Chem (blue line) from January 1 2004 until December 31 2010. The ozonesonde calculated tropospheric ozone columns are shown as stars, each representing one measurement. . . . .	28
2.12 Tropospheric ozone in molecules $\text{cm}^{-2}$ seasonal cycle simulated by GEOS-Chem from January 1 2004 until December 31 2010. The monthly averages are taken for each year and the mean plotted with one standard deviation shaded. . . . .	28
2.13 Tropospheric ozone (ppb) simulated by GEOS-Chem over Davis from January 1 2004 until December 31 2010, averaged monthly. Horizontal dotted line shows the mean tropopause height, shaded areas show one standard deviation. . . . .	29
2.14 As figure 2.16 over Macquarie Island. . . . .	30
2.15 As figure 2.16 over Melbourne. . . . .	31
2.16 Tropospheric ozone (ppb) measured by ozone sonde over Davis, averaged monthly. Horizontal dotted line shows the mean tropopause height, shaded areas show one standard deviation. . . . .	32
2.17 As figure 2.16 over Macquarie Island. . . . .	33
2.18 As figure 2.16 over Melbourne. . . . .	34
2.19 Ozonesonde profiles (black) against GEOS-Chem profiles (red) for three different dates, one over each site. The dates were picked based on subjective visual analysis as follows: left is the best match - May 19th 2004 over Macquarie, middle is an average case - January 15th, 2007 over Davis, and right is the worst match - February 3rd 2005 over Melbourne. . . . .	35
2.20 Simulated and recorded ozone profiles above Davis, Melbourne, and Macquarie Island respectively from top to bottom. The column on the left shows the best matching profile, while the right shows the worst (determined qualitatively). . . . .	36
2.21 Correlation between tropospheric ozone column modelled by GEOS-Chem (vertical axes) and calculated from ozone sondes (horizontal axes). Points are coloured based on their season, shown by the colour bar on the right. The line of best fit (black) and one to one line (dashed) is also shown, note the axes are different for Melbourne. . . . .	37
2.22 Correlation between relative difference of tropospheric ozone column from the monthly mean between profiles modelled by GEOS-Chem (vertical axes) and profiles calculated from ozone sondes (horizontal axes). The line of best fit (black) and one to one line (dashed) is also shown. . . . .	38
2.23 Top panel shows the estimated STT contribution to tropospheric ozone VC. Bottom panel shows the three factors multiplied together in order to produce the estimation. Units for l and f are on the right, while units for ozone VC amounts are on the left. . . . .	40
3.1 MEGAN schematic, copied from Guenther, ( <a href="#">MEGAN</a> ) . . . . .	44
3.2 Solar and viewing zenith angles, image copied from Wikipedia, ( <a href="#">Solar zenith angle</a> ), originally from a NASA website. . . . .	48
3.3 Column density histograms for a subset of OMI swaths over Australia on the 18th of March 2013. Negative entries are shown in the left panel, positive in the right, note the different scale between negative and positive panels. . . . .	54

3.4	Example of grid space change using 0.5x0.5 and 0.25x0.3125 latitude by longitude resolution. . . . .	56
3.5	Example of MODIS 8 day grid interpolation from 0.5x0.5 to 0.25x0.3125 latitude by longitude resolution. This example uses MODIS fire counts for 1-8 January 2005. . . . .	57
3.6	Vertical column HCHO calculated using OMI satellite swaths with GEOS-Chem aprioris, averaged over 1-8 January 2005 with and without fire affected squares removed. . . . .	58
3.7	Example of track correction interpolations for January 1st 2005, points represent satellite slant column measurements, with lines interpolating and extrapolating along the latitudinal direction. . . . .	61



# List of Tables

2.1	Correlations between GEOS-Chem and ozonesonde tropospheric ozone column. and normalised to monthly mean from GEOS-Chem and ozone sonde for respective data.	
3.1	HCHO yields from various species averaged over Australia during Summer. using GEOS-Chem emissions over Australia in January 2005. <sup>c</sup> determined by dividing emission*yield by the sum of all VOC emissions*yields.	43
3.2	HCHO yields from various species. through change in concentration of parent and product linear least squares regression. from satellite detected concentrations of HCHO. using PTR-MS and iWAS on SENEX campaign data. . . . .	53
3.3	OMI quality flag values table from Kurosu and Chance, (2014) . . . . .	43

<sup>a</sup> Produc  
<sup>b</sup> Product  
<sup>c</sup> Produc



# List of Abbreviations

**CTM** Chemical Transport Model  
**DOAS** Differential Optical Absorption Spectroscopy



# Physical Constants

Speed of Light  $c = 2.997\,924\,58 \times 10^8 \text{ m s}^{-1}$  (exact)



# List of Symbols

$a$	distance	m
$P$	power	$\text{W} (\text{J s}^{-1})$
$\omega$	angular frequency	rad



*Dedicated to my broken toe, little piggy number 5*



# Chapter 1

# Background

(TODO: where do I chuck the thesis discussion stuff?) In this thesis I will combine satellite and ground based atmospheric measurements with chemical transport modelling to clarify the impact of Australian natural emissions on atmospheric composition and chemistry.

## 1.1 What are Volatile Organic Compounds (VOCs)?

Organic compounds are members of a large class of chemicals whose molecules contain carbon, with the exception of a few compounds such as carbides, carbonates, simple oxides of carbon and cyanides. Organic compounds can be categorised based on their vapour pressure, which is the tendency of a liquid or solid to vaporise. Compounds with high vapor pressures at standard temperature are classed as volatile, and have a facility to evaporate at low temperatures.

Atmospheric organic compounds are legion and differ by orders of magnitude with respect to their fundamental properties, such as volatility, reactivity, and cloud droplet formation propensity. VOCs have vapor pressure greater than  $10^{-5}$  atm, and are mostly generated naturally by plants, which emit around 1000 Tg per year (Guenther et al., 1995; Glasius and Goldstein, 2016). Due to their high volatility these compounds are generally seen in the gas phase, organic compounds with lower volatility classed as semi-volatile organic compounds (SVOCs: vapor pressure between  $10^{-5}$  and  $10^{-11}$  atm) are seen in both gas and particle phase depending on temperature and pressure. Organic compounds with even lower vapor pressure are generally found in the particle phase in aerosol particulate matter (Glasius and Goldstein, 2016).

Understanding the drivers of trends in biogenic volatile organic compound emissions is needed in order to estimate future carbon fluxes, changes in the water cycle, air quality, and other climate responses (Yue, Unger, and Zheng, 2015).

TODO read and reference <https://orbi.ulg.ac.be/bitstream/2268/174025/1/amt-8.pdf>

## 1.2 Natural gas and aerosol emissions in Australia

### 1.2.1 Australia

Australia is largely covered by environments which are not heavily influenced by human activity. These environments are sources of naturally released trace gases which make up less than 1% of earth's atmosphere. Naturally occurring trace gases in the atmosphere can have a large impact on living conditions. They react in complex ways with other elements (anthropogenic and natural), as well as affecting various ecosystems upon which life depends. Natural emissions affect surface pollution levels and

can alter the radiative and particulate matter distribution of the atmosphere with harmful results. For example, ozone in the lower atmosphere is a serious hazard that causes health problems (Hsieh and Liao, 2013), damages agricultural crops worth billions of dollars (Avnery et al., 2013), and increases the rate of climate warming (Myhre and Shindell, 2013). Particulate matter in the atmosphere is also a major problem, causing an estimated 2-3 million deaths annually (Hoek et al., 2013; Krewski et al., 2009; Silva et al., 2013; Lelieveld et al., 2015).

The Australian outback includes extremely large and diverse environments. Much of the landscape outside of urban areas is undeveloped and sparsely inhabited. In Australia most long term air quality measurements are performed in or near large cities. However, estimates of atmospheric gas and particulate densities and distributions over much of the rest of the continent are uncertain and lack in-situ measurements.

## 1.2.2 Satellite Measurements

Natural emissions from areas with little anthropogenic influence and no ground based measurements characterise the majority of Australian land mass (VanDerA et al., 2008). One source of information which covers the entirety of Australia is remote sensing performed by instruments on satellites which overpass daily recording reflected solar radiation (and emitted terrestrial radiation). These can be used to quantify the abundance of several chemical species as well as estimate their distribution in vertical columns over the land. While satellite data is effective at covering huge areas (the entire earth) it only exists at a particular time of day, is subject to cloud cover, and generally does not have fine horizontal or vertical resolution. Concentrations retrieved from satellite have large uncertainties.

The existence of satellite data covering remote areas provides an opportunity to develop more robust models of global climate and chemistry. Understanding of emissions from these areas is necessary to inform national policy on air pollution levels. Satellite data allow us to verify large scale model estimates of natural emissions. These measurements can be used to improve models, inform national policy, and predict harmful events.

## 1.3 Isoprene

### 1.3.1 Structure

TODO: image of compound and description (probably wikipedia based source)

### 1.3.2 Sources and Sinks

Methane and isoprene each comprise around a third of the yearly global total emission of VOCs. However, methane is relatively long lived (years) and is well mixed in the atmosphere while isoprene levels are very volatile and spatially diverse due to a life time of around an hour. Estimates put global isoprene emission at roughly  $550 \text{ Tg yr}^{-1}$  (Guenther et al., 2006; Monks et al., 2015), emitted mostly by trees and shrubs during the day. Isoprene is hard to measure directly due to its short lifetime and weak spectral absorption, instead formaldehyde is often used as a proxy (Marais et al., 2012; Bauwens et al., 2013; Kefauver, Filella, and Peñuelas, 2014).

Biogenic isoprene emissions are far greater than anthropogenic emissions of VOCs (Guenther et al., 2006; Kefauver, Filella, and Peñuelas, 2014). The lack of accuracy

in BVOC emissions estimates has a large effect on determining with confidence the sources and distribution of pollutants including ozone and organic aerosols. Accuracy in VOC measurements is important: it has been shown that even the diurnal pattern of isoprene emissions has an effect on modelling ground level ozone (Hewitt et al., 2011; Fan and Zhang, 2004). These uncertainties could explain why models of HCHO over Australia are poor at reproducing satellite measurements (Stavrakou et al., 2009).

Guenther et al., (2006) estimates that the Australian outback is among the world's strongest isoprene emitters with forests in SE Australia having emission factors greater than  $16 \text{ mg m}^{-2} \text{ h}^{-1}$  (see figure 1.1).

These emissions factor estimates are not well verified as there is little coverage of isoprene (or other BVOC) emissions measurements over Australia. However, comprehensive coverage of one of the products of isoprene chemistry in the atmosphere over Australia exists in the form of satellite measurements.

It is important to note that many estimates of isoprene emission are based on a few algorithms of isoprene emission which can depend greatly on input parameters (Niinemets et al., 2010). Yue, Unger, and Zheng, (2015) has shown that this is still a problem by looking at land carbon fluxes and modelling the sensitivity to VOC emissions estimates using two independent models of VOC emission. One model is photosynthesis based and estimates isoprene emissions based, while the other (MEGAN) uses the light and canopy temperature (Niinemets et al., 1999; Arneth et al., 2007; Unger et al., 2013).

### 1.3.3 Isoprene From HCHO

Formaldehyde formed in the troposphere is mostly due to VOC oxidation. We can model this oxidation process in order to work out how much VOC is present based on the total HCHO. This requires among other things an idea of which VOCs are present and their yeilds of HCHO. In the remote troposphere HCHO production is dominated by methane oxidation, while in the continental boundary layer production is normally due to NMVOCs (Abbot, 2003; Kefauver, Filella, and Peñuelas, 2014)

Satellites recording reflected solar spectra use Differential Optical Absorption Spectroscopy (DOAS) to measure various trace gases in the atmosphere, including formaldehyde. Formaldehyde levels in the continental boundary layer are generally dominated by chemical formation due to VOC (largely isoprene) emissions (Kefauver, Filella, and Peñuelas, 2014).

Using satellites allows a broad measure of seasonal and interannual variability of HCHO over Australia. These records can be compared with modeled estimates of HCHO and used as a proxy to estimate isoprene emissions. This has been done in North America, South America, and Africa, with satellite and aircraft data combined for validation (Millet et al., 2006; Marais et al., 2014).

TODO: Read and add this list of sources on the hcho to isop process : taken from Wolfe2015 Early studies utilized linear steady-state relationships (Palmer et al., 2003), while recent computational advances have permitted full inversions that more fully account for transport, multiple sources and varying chemical regimes (Fortems-Cheiney et al., 2012). Such techniques have informed isoprene emission inventories in North America (Abbot et al., 2003; Millet et al., 2008, 2006; Palmer et al., 2006, 2003), South America ((Barkley et al., 2013), 2008), Europe (Curciel et al., 2010; Dufour et al., 2009), Africa (Marais et al., 2012), Asia (Fu et al., 2007; Stavrakou et al., 2014), and globally (Fortems-Cheiney et al., 2012; Shim et al., 2005; Stavrakou et al., 2009).

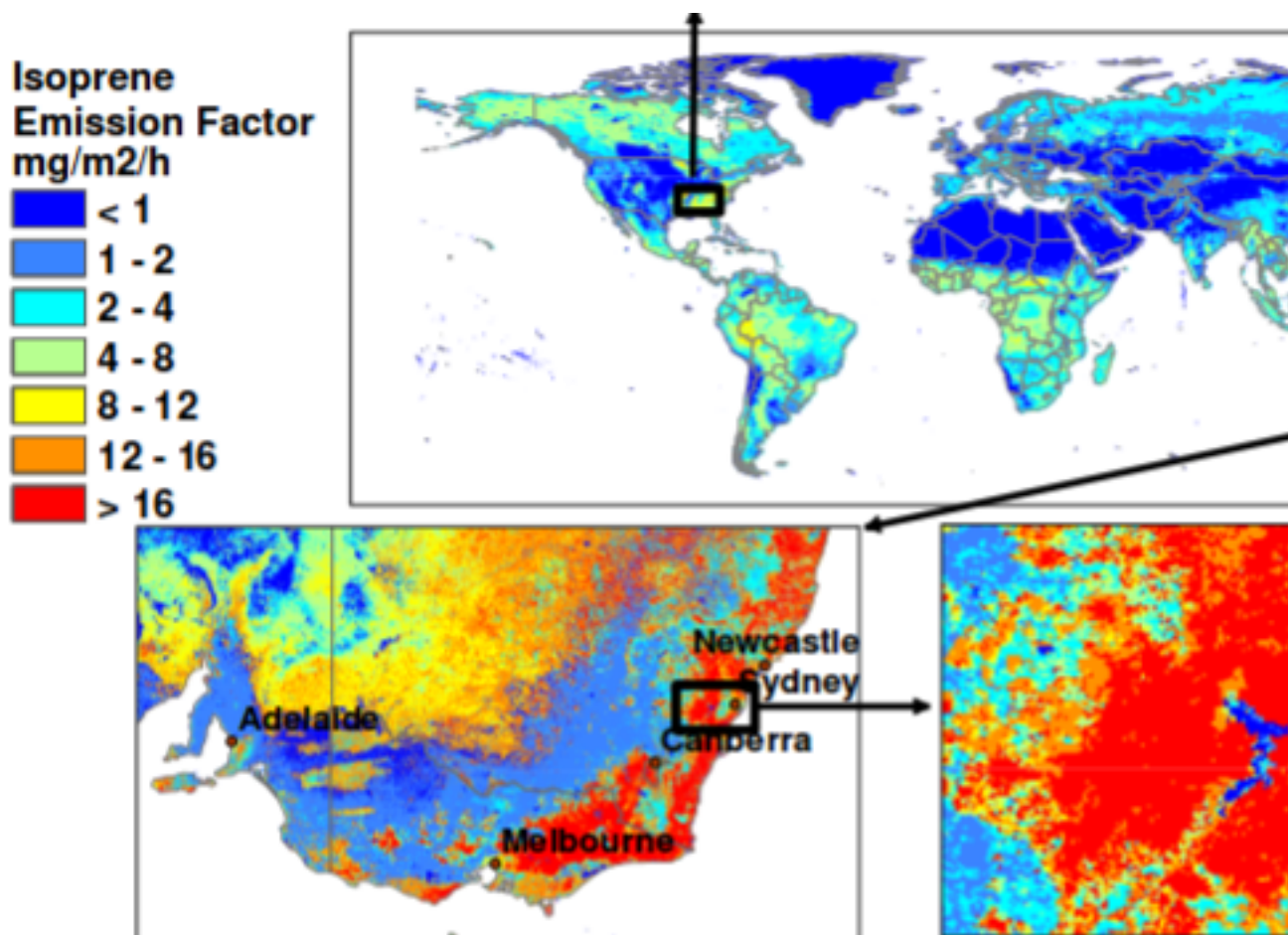
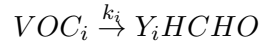


**Fig. 2.** Global distribution of landscape-average isoprene emission factors ( $\text{mg isoprene m}^{-2} \text{ h}^{-1}$ ). Spatial resolution ( $\sim 1 \text{ km}$ ) is shown by regional images of the southeastern U.S. and southeastern Australia.

FIGURE 1.1: Part of a figure from Guenther et al., (2006) showing global isoprene emission factors.

The methodology for calculating VOCs from HCHO is laid out in Palmer, (2003), and takes into account the expected lifetime and reaction rates of the precursor VOCs and HCHO. Assuming HCHO is produced quickly from short-lived intermediates we get



Where  $Y_i$  is HCHO yield per C atom (a measure of how much HCHO will form per gram of C from a VOC within a system). Then assuming a steady state of atmospheric HCHO ( $\Omega$  molecules  $cm^{-2}$ ) produced by oxidation of VOCs ( $VOC_i$ ) and no horizontal transport:

$$\Omega = \frac{1}{k_{HCHO}} \sum_i Y_i E_i$$

Where i indexes a chemical species, and  $E_i$  is emission fluxes (C atoms  $cm^{-2}s^{-1}$ ).

Inferring the VOC emissions then requires estimates of the HCHO yield ( $Y_i$ ) which can be attained via modelling as layed out in Millet et al., (2006).

During low NO<sub>x</sub> conditions, the precursor HCHO has a longer lifetime (days). This allows horizontal transport to occur and complicates the algorithms. Horizontal transport 'smears' the HCHO signal so that source location would need to be calculated using windspeeds and loss rates. For conditions where VOCs have a lifetime of days determining the major HCHO contributors requires a complex inversion to map HCHO columns to VOC emissions.

In high NO<sub>x</sub> environments where HCHO has a lifetime on the order of 30 minutes, it can be used to map isoprene emissions with spatial resolution from 10-100 kms. This can be determined using the calculations from (TODO: cite and formula for spatial resolution)

### 1.3.4 Measurements

There are relatively few measurements of isoprene in the southern hemisphere, including MUMBA(TODO CITE), other campaigns?, and very recently that girl from Macquarie University with an instrument in the daintree rainforest(TODO CITE, DESCRIBE?). Since 1997, when GOME first measured HCHO over Asia (TODO cite thomas 1998), satellites have been able to provide a total column measurement of one of the primary products of isoprene.

### 1.3.5 Estimates

There are two commonly used ways of estimating isoprene emissions, top-down or bottom-up. Bottom-up emission estimates generally model the flora and events which emit isoprene, like Eucalypts, factories, fires, etc. Understanding how much isoprene is emitted, when and by what is more complicated than it sounds, and since little data exists with which to verify these bottom-up emission inventories they are hard to verify on a large scale. Top-down estimates look at how much of a chemical is in the atmosphere and try to work out how much isoprene was emitted. Generally this is done by looking at atmospheric HCHO enhancement, which can be largely attributed to isoprene emissions.

### 1.3.6 Radiative Forcing

## 1.4 Formaldehyde

### 1.4.1 Structure

TODO: image and description

### 1.4.2 Sources and sinks

### 1.4.3 Measurements

There are a few ways to measure HCHO, including FTIR and MAX-DOAS. As a trace gas HCHO interferes with light over a few wavelength bands, which allows instruments to detect concentrations along a path between a sensor and a known light source like a lamp or the sun.

## 1.5 Dust

Australia is the greatest source of dust in the southern hemisphere producing around 120 Tg yr<sup>-1</sup> (Li, Ginoux, and Ramaswamy, 2008), however model validation and analysis over Australia is relatively scarce with more focus applied to the northern hemisphere (Duncan Fairlie, Jacob, and Park, 2007; Ridley et al., 2013). Atmospheric dust has many direct effects including reduced surface insolation, mineral transfer to remote ocean regions, and health degradation in populated areas (Shao et al., 2007). Direct and indirect effects of dust have many implications which are not fully understood, with many models still struggling to explain the atmospheric cycling of dust at larger scales (Rotstayn et al., 2011).

Australian dust emissions involve various weather conditions, convolving the ENSO cycle with flooding, droughts, and winds. Rivers and rain build up the particulate matter in many areas, these are referred to as fluvial deposits. Fluvial deposits in the Eyre basin increase the dust base load, which will only have mobility during suitable dry weather conditions. These deposits are saltated (loosened from the surface) and transported by strong winds(Zender, 2003).

Synoptic scale measurements of dust concentrations in Australia are made by the Bureau of Meteorology (BOM) and can be used to estimate dust transport caused by large storms. Single storms have been estimated to move up to 2.5 Tg of dust off shore in a single day. Yearly dust emissions in Australia are somewhere between 10 and 110 Tg yr<sup>-1</sup>. These estimates exemplify the large variability in Australian annual dust transport.

Dust plays a large role in the oceanic carbon cycle, as dust is a major source of oceanic iron (Fe) deposition. Some regions in the ocean are high in nutrients, but low in chlorophyll (HNLC), due to a lack of Fe. Oceanic carbon cycling is a complex system in which Fe is a limiting factor, required by plankton in order to fix atmospheric nitrogen into a more bioavailable form such as ammonia. Atmospheric deposition into the oceans is a very poorly constrained variable in global models (Grand et al., 2015). Model estimates of trace element oceanic deposition are required to quantify the atmospheric impact due to a dearth of in situ measurements in remote open ocean regions.

Measurements of dissolved iron (DFe) at very low concentrations like those found in surface ocean waters are very easily contaminated, which has contributed the the

fragmentary and scarce nature of DFe ocean data sets (Rijkenberg et al., 2014). Recent analysis of the US Climate Variability and Predictability (CLIVAR)-CO<sub>2</sub> Repeat Hydrography Program predicted total deposition flux with uncertainty at a factor of 3.5 (Grand et al., 2015). Some headway has been made with the recent GEOTRACES program which has several transects of the major oceans and measures trace elements over multiple depths including Al, Ba, Cu, Cd, Fe, Mn, Ni, Pb, and Zn.

Total iron (TFe) emissions from dust and combustion sources are estimated (by average of several global models) at approximately 35 Tg yr<sup>-1</sup> and 2 Tg yr<sup>-1</sup> respectively. A two fold increase in Fe dissolution may have occurred since 1850 due to increased anthropogenic emissions and atmospheric acidity. This increase may revert by 2100 due to the affects of emission regulations (Myriokefalitakis et al., 2015). Dust, TFe and DFe have strong temporally and spatial variability, with changes having most impact upon HnLC regions.

Another environmental impact of dust is its contribution to fine particulate matter in the atmosphere. Several studies have shown that long term exposure to fine particulate matter (PM2.5) increases mortality. Estimates of yearly premature deaths related to PM2.5 are ~ 2-3 million (Hoek et al., 2013; Krewski et al., 2009; Silva et al., 2013; Lelieveld et al., 2015). These estimates are made using global atmospheric models or model ensembles to quantify population exposure before applying epidemiological models to estimate the increased death rates. The main source of uncertainty in premature death rates arises from the difference and uncertainties between and within the atmospheric models.

Dust affects global climate change through direct radiative forcing. Uncertainties in the atmospheric dust concentrations make accurate determination of radiative forcing from other sources more difficult (Myhre and Shindell, 2013).

## 1.6 Models

### 1.6.1 Chemical Transport Models

Chemical Transport Models (CTMs) simulate production, loss, and transport of chemical species. This is generally calculated using one or both of the Eulerian (box) or Lagrangian (puff) frames of reference. CTMs normally solve the continuity equations simultaneously with chemical production and loss for chemicals under inspection. The continuity equations describe transport of a conserved quantity such as mass, which, solved together with production and loss of a chemical forms the basis for a CTM. This basis enables a record of the chemical densities and transport over time as a model runs. The general continuity equation links a quantity of a substance ( $q$ ) to the field in which it flows and can be described by the formula:

$$\frac{\partial \rho}{\partial t} + \nabla \cdot j = \sigma$$

where  $\rho$  is density of  $q$  in the field,  $t$  is time,  $\nabla$  is divergence,  $j$  is the flux (the amount of  $q$  per unit area per unit time entering or leaving the field), and  $\sigma$  is the generation of  $q$  per unit volume per unit time. Note that  $\sigma$  can be positive or negative due to sources and sinks.

The type of model best suited to modelling the entire earth uses the Eulerian frame of reference, where the atmosphere is broken up into 3-D boxes with densities and transport calculated and stored for arbitrary sequential steps in time at each location.

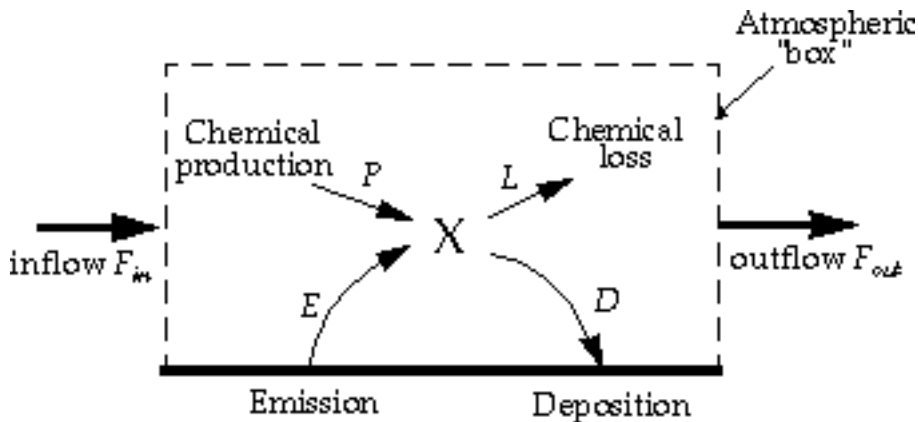


FIGURE 1.2: Standard box model parameters, image taken from Jacob, (1999).

The mass balance equation must be satisfied in any realistic long term box model and is as follows:

$$\begin{aligned}\frac{dm}{dt} &= \sum \text{sources} - \sum \text{sinks} \\ &= F_{in} + E + P - F_{out} - L - D\end{aligned}$$

where m is mass of a chemical, E and D are emission and deposition, P and L are production and loss, and F is chemical transport in and out, as shown in figure 1.2. Many chemical species interact with each other through production and loss. Any large chemical model will solve this mass balance equation over highly coupled arrays of partial differential equations which can be complex and time consuming.

In many CTMs the isoprene emissions are calculated elsewhere with their own models (EG: Guenther et al., (2006)). These estimates can then be used as boundary conditions. Trace gases with short lifetimes and complex chemistry such as isoprene are often hard to measure which makes verifying model estimates difficult.

### 1.6.2 GEOS-Chem

GEOS-Chem is a well supported global, Eulerian CTM with a state of the science chemical mechanism, with transport driven by meteorological input from the Goddard Earth Observing System (GEOS) of the NASA Global Modeling and Assimilation Office (GMAO). GEOS-Chem simulates more than 100 chemical species from the earth's surface up to the edge of space (0.01 hPa) and can be used in combination with remote and in-situ sensing data to give a verifiable estimate of atmospheric gases and aerosols. It was developed, and is maintained, by Harvard University staff as well as users and researchers worldwide. Several driving meteorological fields exist with different resolutions, the finest at 0.25 by 0.3125° horizontally at 5 minute time steps with 72 vertical levels.

Combining satellite data with model outcomes provides a platform for the understanding of natural processes to be tested now and into the future over Australia and anywhere with few in-situ measurements. Due to the low availability of in-situ data covering most of the Australian continent, a combination of the models with satellite data may provide improved understanding of emissions from Australian landscapes. Improved emissions estimates will in turn improve the accuracy of CTMs, providing

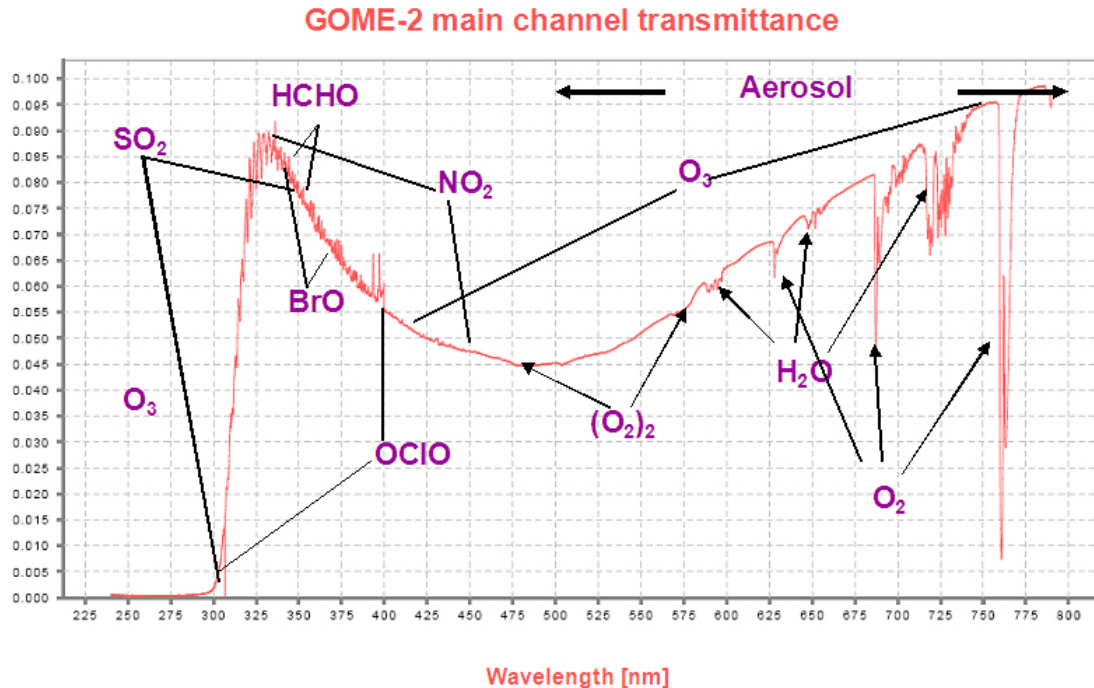


FIGURE 1.3: An example spectrum showing interferences used for species concentration measurements by GOME-2. Image by EUMETSAT and ESA (EUMETSAT, 2015).

better predictions of atmospheric composition and its response to ongoing environmental change.

## 1.7 Satellites

### 1.7.1 Useful satellites

Several satellites provide long term trace gas observations with near complete global coverage, including the ERS-2 launched in April 1995 which houses the GOME ultraviolet and visible (UV-Vis) spectrometer, the AURA launched in July 2004 which houses the OMI UV-Vis spectrometer, the MetOp-A and B launched in October 2006 and September 2012 respectively both housing a GOME-2 UV-Vis spectrometer. These satellites are on Low Earth Orbit (LEO) trajectories and overpass any area up to once per day. They record near nadir (nearly vertical) reflected spectra between around 250-700 nm split into spectral components at around 0.3 nm in order to calculate trace gases including  $\text{O}_3$ ,  $\text{NO}_2$ , and  $\text{HCHO}$ . An example of a spectrum retrieved from the GOME-2 instrument is given in figure 1.3.

Formaldehyde ( $\text{HCHO}$ ) is often used as a proxy to estimate isoprene emissions (Marais et al., 2012; Bauwens et al., 2013). Satellites can use DOAS techniques with radiative transfer calculations on solar radiation absorption spectra to measure column  $\text{HCHO}$  (eg: Leue et al., (2001)). Several public data servers are available which include products from the satellites just mentioned, including NASA's Mirador (<http://mirador.gsfc.nasa.gov>, and the Belgian Institute for Space Aeronomy (IASB-BIRA) Aeronomie site (<http://h2co.aeronomie.be>

Instruments including MODIS on board the AQUA and TERRA satellites are able to determine aerosol optical depth (AOD), a measure of atmospheric scatter and absorbance. An AOD of under 0.05 indicates a clear sky, while values of 1 or greater indicate increasingly hazy conditions. This is an important atmospheric property allowing us to track dust storms and pollution events as well as determine where measurements from other instruments may be compromised by high AOD. Satellite measured AOD requires validation by more accurate ground based instruments like those of AERONET which uses more than 200 sun photometers scattered globally.

### 1.7.2 Comparisons with Models

DOAS methods can be heavily influenced by the initial estimates of a trace gas profile (the a priori) which is often produced by modelling, so when comparing models of these trace gases to satellite measurements extra care needs to be taken to avoid introducing bias from unrealistic a priori assumptions. A way to remove these a priori influences in order to compare models and satellites is through the satellite's averaging kernel, which is a measure of the sensitivity of the instrument to the trace gas's radiance at various heights multiplied by the sensitivity of the DOAS technique's forward radiative transfer model (RTM) to the amount of trace gas at various heights near the a priori (Eskes and Boersma, 2003).

### 1.7.3 DOAS

TODO: some of this is repeated in isoprene chapter satellite section.

The DOAS technique uses solar radiation absorption spectra to measure trace gases through paths of light. The RTM used in DOAS techniques is based on Beer's law relating the attenuation of light to the properties of the medium it travels through. Beer's law states that  $T = I/I_0 = e^{-\tau}$  with  $T$  being transmittance,  $\tau$  being optical depth, and  $I, I_0$  being radiant flux received at instrument and emitted at source respectively. Using  $\tau_i = \int \rho_i \beta_i ds$  gives us:

$$I = I_0 \exp \left( \sum_i \int \rho_i \beta_i ds \right)$$

Where  $i$  represents a chemical species index,  $\rho$  is a species density(molecules per  $\text{cm}^3$ ),  $\beta$  is the scattering and absorption cross section area ( $\text{cm}^2$ ), and the integral over  $ds$  represents integration over the path from light source to instrument. The forward RTM used for satellite data products also involves functions representing extinction from Mie and Rayleigh scattering, and the efficiency of these on intensities from the trace gas under inspection, as well as accounting for various atmospheric parameters which may or may not be estimated (e.g. albedo).

To convert the trace gas profile from a reflected solar radiance column (slanted along the light path) into a purely vertical column requires calculations of an air mass factor (AMF). In satellite data, the AMF is typically a scalar value for each horizontal grid point which will equal the ratio of the total vertical column density to the total slant column density. This value should also account for instrument sensitivities to various wavelengths at various altitudes, and is unique for each trace gas under consideration.

# Chapter 2

## Stratosphere to Troposphere Transport of ozone

### 2.1 Background

#### 2.1.1 Historical estimates

Tropospheric ozone is important for both air quality and climate change. The impact of stratospheric ozone on the troposphere is dependent on weather, season, temperature, and many other factors. For example changing ozone in the tropical tropopause layer by 5% causes  $0.5 \text{ K dec}^{-1}$  radiative heating (Forster et al., 2007). In Australia, records of ozone profiles provided by the Department of the Environment can be used to determine how often stratospheric ozone descends into the troposphere.

Over the industrial period, tropospheric ozone, which is the third most potent greenhouse gas, has been estimated to exert a radiative forcing equivalent to a quarter of the CO<sub>2</sub> forcing. Ozone is present in the troposphere due to a variety of dynamical and photochemical processes, including downward transport from the ozone-rich stratosphere and anthropogenic pollution. The primary sources of tropospheric ozone are chemical creation and stratospheric input, estimated using a model ensemble to be  $5100 \pm 600 \text{ Tg/yr}$  and  $550 \pm 170 \text{ Tg/yr}$ , respectively (Stevenson et al., 2006). The primary sinks are chemical destruction and dry deposition, estimated to be  $4700 \pm 700 \text{ Tg/yr}$  and  $1000 \pm 200 \text{ Tg/yr}$ , respectively (Stevenson et al., 2006).

#### 2.1.2 Tropospheric production

Ozone is a toxic trace gas which increases mortality rates when populations are exposed for extended periods of time. The amount of global premature deaths per year due to atmospheric ozone exposure has recently been estimated at  $\sim 150\text{-}470$  thousand (Silva et al., 2013; Lelieveld et al., 2015). Long term effects of ozone overexposure increase the risk of respiratory disease and may also increase other cardiopulmonary risks (Jerrett et al., 2009).

The Ambient Air Quality (AAQ) National Environment Protection Measure (NEPM), which is the Australian framework for air quality measurement and reporting aiming for “adequate protection of human health and well-being” has set national standards and benchmarks for reporting. The NEPM covers six chemical groups including Ozone (O<sub>3</sub>), and the benchmarks are shown in figure 2.1.

The primary source of ozone in the lower troposphere is chemical formation following emissions of precursor gases, including VOCs, and NO<sub>X</sub>. Globally the greatest sources of NO<sub>X</sub> include fossil fuel combustion ( $\sim 50\%$ ), biomass burning ( $\sim 20\%$ ), lightning, and microbial activity in soils (Delmas, Serca, and Jambert, 1997). Estimates

NEPM standards and goals specified in Schedule 2 of the AAQ NEPM			
Pollutant	Averaging period	AAQ NEPM standard (maximum concentration)	AAQ NEPM goal (maximum number of allowable exceedences)
Carbon monoxide	8-hour rolling average	9.0 ppm	1 day a year
Nitrogen dioxide	1-hour average	0.120 ppm	1 day a year
	1-year average	0.030 ppm	None
Photochemical oxidants – as ozone	1-hour average	0.100 ppm	1 day a year
	4-hour rolling average	0.080 ppm	1 day a year
	1-hour average	0.200 ppm	1 day a year
Sulfur dioxide	1-day average	0.080 ppm	1 day a year
	1-year average	0.020 ppm	None
Particles as PM <sub>10</sub>	1-day average	50.0 µg/m <sup>3</sup>	5 days a year
Lead	1-day average	0.50 µg/m <sup>3</sup>	None
Particles as PM <sub>2.5</sub> <sup>1</sup>	1-day average	25.0 µg/m <sup>3</sup>	Gather sufficient data nationally to facilitate a review of the Advisory Reporting Standard
	1-year average	8.0 µg/m <sup>3</sup>	

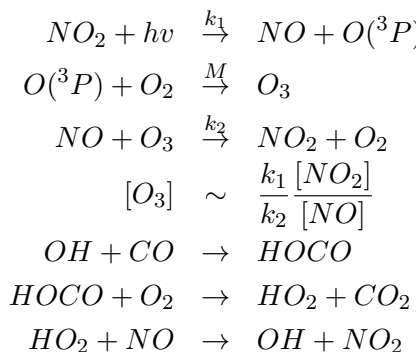
<sup>1</sup> Reporting standard only

FIGURE 2.1: NEPM standards taken from National Environment Protection Council annual report 2012-2013 (Environment and the National Environment Protection Council), 2015).

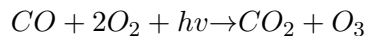
using CHASER (a global Chemical Transport Model (CTM)) constrained by measurements from two satellites as well as the in-situ measurements taken through LIDAR and aircraft (INTEX-B) put global tropospheric NO<sub>x</sub> emissions at 45.4 TgN yr<sup>-1</sup> in 2005 (Miyazaki, Eskes, and Sudo, 2011).

The majority of this chemical formation is due to photochemical oxidation of carbon monoxide (CO), methane (CH<sub>4</sub>), and other Volatile Organic Chemicals (VOCs) in the presence of nitrogen oxides (NO<sub>x</sub> ≡ NO + NO<sub>2</sub>) (Stevenson et al., 2006).

Photolysis of NO<sub>2</sub> forms NO + O(3P), which combines with O<sub>2</sub> to form O<sub>3</sub>, leading to reaction with NO to form NO<sub>2</sub> + O<sub>2</sub>. These reactions reach a steady state where O<sub>3</sub> is proportional to the ratio between NO<sub>2</sub> and NO (Sillman, 2002). The following formulae show an example of this with CO, however, similar reactions occur for many VOCs:



where  $k_1$  and  $k_2$  are reaction rates, and  $h\nu$  represents photons. The balance of these reactions is:



Note that this reaction pathway only occurs during the day.

Isoprene ( $C_5H_8$ ) is a precursor to ozone through radical oxidative chemistry. Isoprene in the atmosphere reacts rapidly with hydroxyl radicals ( $OH$ ) and then  $O_2$  to form peroxy radicals ( $RO_2$ ). These react with nitrogen oxides and can lead to ground-level ozone formation similarly to the CO reaction listed prior.

Formaldehyde ( $HCHO$ ) together with  $NO_2$  regulate tropospheric oxidation capacity through  $O_3$  production, as well as being health hazards. The  $HCHO/NO_2$  ratio can be used to determine whether surface  $O_3$  is  $NO_2$  or VOC limited (Mahajan et al., 2015). If  $O_3$  is  $NO_2$  limited then an increase in  $NO_2$  will increase  $O_3$  levels while an increase in  $HCHO$  will not, and vice versa when  $O_3$  is  $HCHO$  limited.  $NO_2$  is a common pollutant in populated areas, released primarily by combustion in power generation and transport. Outside of cities in Australia, VOCs and  $NO_x$  are emitted from biogenic sources, although lightning, and biomass burning (most clearly in the Northern Territory) also play a role (Guenther et al., 2006; VanDerA et al., 2008).

### 2.1.3 Stratosphere to Troposphere ozone Transport (STT)

While the amount of tropospheric ozone is small compared with that found in the stratosphere, it is an important constituent. Ozone-rich air mixes irreversibly down from the stratosphere during meteorologically conducive conditions (Sprenger, Croci Maspoli, and Wernli, 2003; Mihalikova et al., 2012); these are referred to as Stratosphere - Troposphere Transport events (STTs). In the extra-tropics, STTs most commonly occur during synoptic-scale tropopause folds (Sprenger, Croci Maspoli, and Wernli, 2003) and are characterised by tongues of high Potential Vorticity (PV) air descending to low altitudes. PV is a metric which can be used to determine whether a parcel of air is stratospheric, based on its local rotation and stratification. Within the troposphere PV values are typically low, increasing rapidly into the stratosphere due to the increased static stability.

These ozone rich tongues become elongated and filaments separate from the tongue which mix into tropospheric air. Stratospheric ozone brought deeper (lower) into the troposphere is more likely to affect the surface ozone budget and tropospheric chemistry (Zanis et al., 2003; Langford et al., 2009). A high correlation is found between lower stratospheric and tropospheric ozone (Terao et al., 2008) with the highest STT associated with the jet-streams over the oceans in winter. Irreversible STT of ozone is important for explaining tropospheric ozone variability (Tang and Prather, 2010). Stratosphere to Troposphere ozone transport can potentially increase regional surface ozone levels above safe levels (Zhang et al., 2014).

While photochemical production is the dominant source, stratosphere to troposphere transport of ozone is also important and climate change may drastically increase this quantity (Hegglin and Shepherd, 2009). In a future climate, a warmer, wetter troposphere will change the chemical processing of ozone. Dynamical processes such as STT, boundary layer ventilation and convection changes will alter tropospheric ozone distributions. Hegglin and Shepherd, (2009) estimate that climate change will lead to increased STT of the order of 30 (121)  $Tg\ yr^{-1}$  relative to 1965 in the southern (northern) hemisphere due to an acceleration in the Brewer Dobson circulation.

STT events are characterised in the ozonesondes' vertical profiles of ozone as altitudes in the troposphere where the ozone mixing ratio exceeds a specified threshold. Usually stratospheric ozone mixes irreversibly down into the troposphere in a synoptic-scale tongue of air: the vertical ozone profile observed by the ozonesonde depends upon the time in this cycle that it is observed (Sprenger, Croci Maspeli, and Wernli, 2003). As such, the altitude of the tropospheric ozone peak due to an STT event, and the amplitude of the event above the background tropospheric ozone profile, vary in space and time.

## 2.2 Instruments and data sets

### 2.2.1 Atmospheric Infrared Sounder (AIRS)

AIRS is an instrument on board NASA's AQUA satellite, which overpasses the globe roughly daily on a sun-synchronous orbit gathering measurements at 1:30pm local time. AIRS is a high spectral resolution spectrometer with 2378 bands in the thermal infrared (3.7 - 15.4  $\mu\text{m}$ ) and 4 bands in the visible (0.4 - 1.0  $\mu\text{m}$ ). One of the products shared by NASA is total column carbon monoxide (AIRS3STD ([AIRS3STD 2013](#))). Using this product to exclude possible fire plume transport from STT analysis is done in section [2.5.2](#).

### 2.2.2 Sondes

Ozonesondes are weather balloons with an attached instrument which measures ozone concentrations roughly every 100m up to around 30km. These ozonesondes provide a high-vertical resolution profile of ozone.

In this work sonde data from three sites are utilised: Davis (lat, lon, UTC +7), Macquarie Island (lat, lon, UTC +11), and Melbourne (lat, lon, UTC +11). Ozonesondes are launched approximately weekly from these three sites, we examine data from up to 2013, starting in 2004 at Melbourne and Macquarie Island, and 2006 at Davis. More frequent ozonesonde launches occur at Davis during the spring ozone hole season than at other times of the year (Alexander, Murphy, and Klekociuk, 2013).

### 2.2.3 European Centre for Medium-Range Weather Forecasts (ECMWF) Re-Analysis - Interim data set (ERA-I)

Ozonesondes provide much higher vertical resolution profiles of ozone than that available from reanalyses products. The downside is that one data point per week from an ozonesonde release is too low to be in itself useful to diagnose the evolution of STT exchange over time-scales associated with normal synoptic scale weather patterns present in the extra-tropics. The ECMWF provides a useful meteorological model based on assimilated data. Here, ozonesonde data are supplemented with the ERA-I dataset (Dee et al., 2011) to enable construction of an STT exchange climatology. The dataset is called a re-analysis due to the fact that the whole timeline gets re-run when the climatological model is updated. This provides uniform data output over a long time period.

The ERA-I data we used for synoptic weather was of one degree horizontal resolution with pressure levels at 200, 300, 400, and 500 hPa. For individual cases ERA-I data was downloaded at .25 degree horizontal resolution with the full 34 pressure levels from 1000 to 1 hPa. Note that 34 levels up to the top of the atmosphere is not enough to

determine vertical transport when considering only a single vertical profile, however a precise view of coincident weather can determine probable cause of ozone flux.

## 2.3 STT Detection

### 2.3.1 Aim

Using several years of ozonesonde flights from three locations spanning the latitudes of the Southern Ocean, we create and examine a quantitative method for detecting ozone STT events from ozone vertical profiles. With a quantitative method of STT detection characterisation of the seasonal cycle of STT events and determination of their contribution to the total amount of tropospheric ozone is possible. Examination of the ozone intrusions and case studies allows us to relate these STT to meteorological events. Finally we use the same filtered sonde data in order to extract a lower bound estimate of how much of the tropospheric column ozone is due to STT events.

### 2.3.2 Tropopause Heights

Two definitions of the tropopause height are calculated: the standard lapse rate tropopause (WMO, 1957), and the ozone tropopause (Bethan, Vaughan, and Reid, 1996). At Davis, the ozone tropopause defintion is modified for polar sites, following Tomikawa, Nishimura, and Yamanouchi, (2009) and Alexander, Murphy, and Klekociuk, (2013). While the ozone tropopause can be less robust during stratosphere-troposphere exchange, it performs better than the lapse rate tropopause at polar latitudes in winter and near jet streams in the lower stratosphere (Bethan, Vaughan, and Reid, 1996). The lower of these two tropopause altitude-definitions is referred to as the tropopause for this study. This choice of the lowest altitude of the tropopause avoids occasional unrealistically high tropopause heights due to perturbed ozone or temperature measurements.

The monthly mean tropopause altitudes at each location are shown in Figure 2.2, along with the subset of altitudes from profiles for which an STT event was determined. The seasonal cycle in tropopause altitude at Melbourne is clearly apparent, as is the decreasing tropopause altitude poleward. Seasonally averaged ozone as recorded over the three stations (Figure 2.3) shows increased ozone extending down through the stratosphere during the peak STT months over Melbourne. It is worth noting that tropopause altitudes at Davis may exceed 11 km altitude under certain synoptic conditions (Alexander, Murphy, and Klekociuk, 2013): the relation of tropopause altitude with individual STT events will be investigated in detail below.

### 2.3.3 Fourier bandwidth (or bandpass) Filtering

A Fourier bandwidth filter can remove components of a line based on the components frequency. For example: a noisy ozone profile can be 'cleaned' by removing the high frequency components, while growth of ozone with altitude in the profile can be removed as a low frequency component.

TODO: Add description, equation(s) and maybe a simple example plot here as well as limits of filter. The basic idea of a Fourier bandwidth filter is that any finite length function can be written as a series of trigonometric functions:

$$f(t) = \sum_i C_{w_i} \cos(w_i t - \theta_i) \quad (2.1)$$

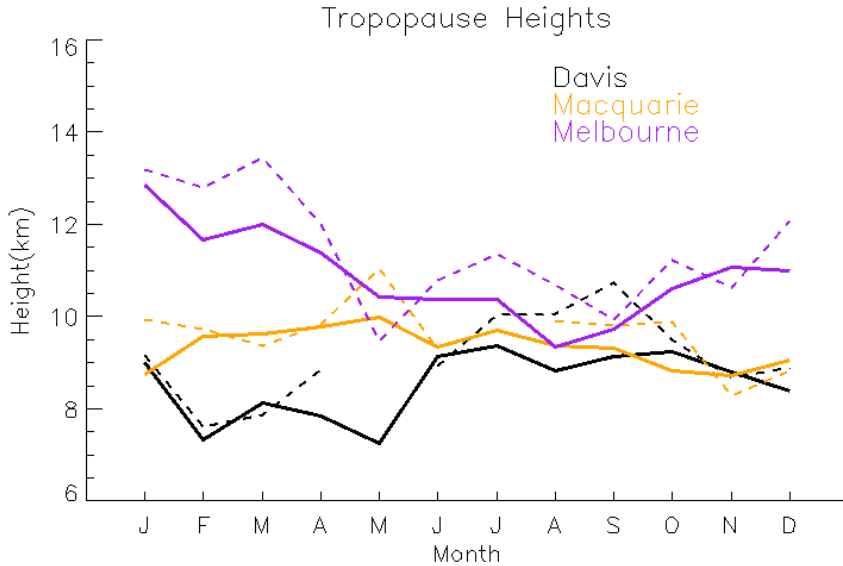


FIGURE 2.2: Monthly mean tropopause altitudes (minimum of lapse-rate and ozone defined tropopauses). Dashed lines show 'event only' seasonal tropopause altitudes.

Once we split our function into specific frequencies ( $w_i$ ) we can simply remove the terms which fall outside our desired wavelength range. One limitation is that the reconstructed function may be quite different at either end of the input range.

In the continuous spatial domain, this is done through taking the Fourier transform which can convert our function to a complex frequency domain:

$$F(w) = \frac{1}{\sqrt{2\pi}} \int_{-\infty}^{\infty} f(t) e^{-iwt} dt$$

where  $t$  describes the spatial input range (in our case altitude). Then it's possible to remove the portion of the function outside the desired frequency before inverting the Fourier transform:

$$f(t) = \frac{1}{\sqrt{2\pi}} \int_{-\infty}^{\infty} F(w) e^{iwt} dw$$

This whole process is slightly changed when we consider discrete dimensions as we must whenever solving numerically or handling real world resolved datasets. There is a "shortcut" method which

### 2.3.4 Bandwidth filter applied to ozonesondes

With a Fourier bandwidth filter used on ozone profiles over Davis, Macquarie, and Melbourne we quantitatively determine instances of Stratosphere to Troposphere Transport events through the following method. The vertical profiles of ozone volume mixing ratio are linearly interpolated to a regular grid with 20m resolution up to 14km altitude and are then bandpass filtered so as to retain perturbations which have vertical scales between 0.5km - 5km. The choice of band limits is set empirically, but we note that to define an STT event, a clear increase above the background ozone level is needed, and a vertical limit of  $\sim 5$  km removes seasonal-scale effects. The ozone

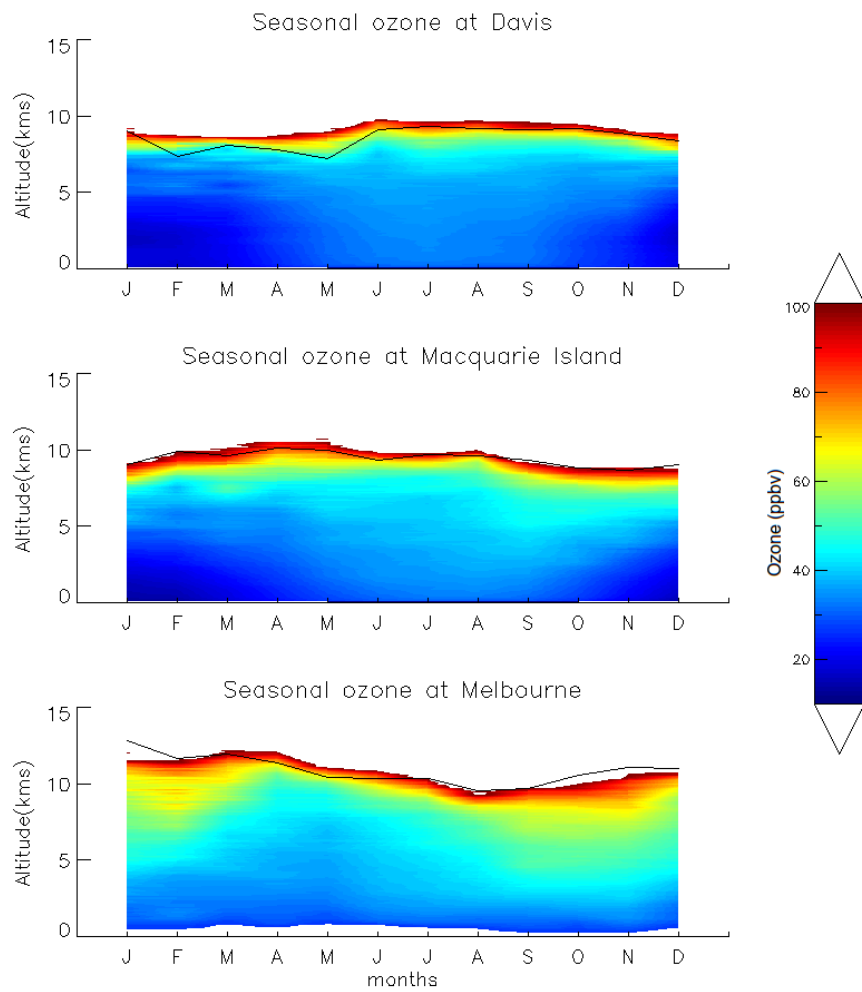


FIGURE 2.3: Seasonally averaged ozone over Davis, Macquarie, and Melbourne measured by ozonesondes. Black solid lines show seasonal tropopause heights.

perturbation profile is analysed at altitudes from 4 km above the surface (to avoid surface pollution events) and 1 km below the tropopause (to avoid the sharp transition to stratospheric air producing spurious false positives). Perturbations above the 99 th percentile (locally) of all ozone levels are initially classified as STT events.

In order to remove unclear 'near tropopause' anomalies we remove events where the gradient between the maximum ozone peak and the ozone at 1 km below the tropopause is greater than  $-20 \text{ ppbv km}^{-1}$  and simultaneously require that the perturbation profile does not drop below zero between the event peak and the tropopause. The addition of these filters removes several events, each with an ozone peak which could not be definitively said to be separated from the stratosphere.

To provide a conservative estimate of ozone flux into the troposphere for each event, the ozone concentration is integrated vertically over the interval for which an STT event is identified. An example of an ozone profile is illustrated in Figure 2.4 and indicates how the algorithm detects an STT event, defines the event boundaries, and calculates the ozone flux.

### 2.3.5 Case Studies

We examine two STT case studies in detail to illustrate the synoptic scale conditions in which they can occur above Melbourne.

A cut-off low pressure system passed over Melbourne on 3 February 2005 (Figure 2.5b). The ozonesonde profile indicated low lapse-rate and ozonesonde tropopauses (both  $> 450 \text{ hPa}$ , see Figure 2.5a). An ozone intrusion into the troposphere is identified by our detection algorithm at  $\sim 520 \text{ hPa}$ .

STT events also occur during frontal passages, an example of which is illustrated in Figure 2.5d over south-eastern Australia. The tropopauses are much higher at this time and an ozone intrusion is identified centred around 200 hPa. Note the separation between this intrusion and the ozone tropopause (marked by the green dashed line), indicating the start of the stratosphere above Melbourne. During the frontal passage, stratospheric air descends and streamers of ozone-rich air likely break off and mix into the troposphere (Sprenger, Croci Maspeli, and Wernli, 2003). TODO: talk about pvu lines here.

The relative humidity profiles are anticorrelated with ozone in the upper troposphere for these events, indicating again the stratospheric origin of the ozone-rich air mass. TODO: show latlon plots for the sites and describe lowered tropopause in more detail here. Some of this stratospheric air gets mixed into the troposphere, with one ozonesonde column showing an intrusion at around 200 hPa, with dry ozone rich air peaking below the tropopause (Figure 2.5c).

### 2.3.6 Site summaries

Running the ozonesonde dataset through our bandpass filter and analysing the results allows an overview of the yearly cycle and event characteristics. These seasonal cycles and event characteristics for each of the three locations are presented in Figure 2.6 to Figure 2.8. There is an annual cycle in the occurrence frequency of STT events (with a summertime peak) above Melbourne and Macquarie Island. However, the occurrence frequency of STT events above Davis is relatively constant throughout the year.

The majority of events occur within 3 km of the tropopause at both Melbourne and Macquarie Island, and within 2 km of the tropopause at Davis. STT event altitudes

# Ozone at Melbourne

## 2004/01/08

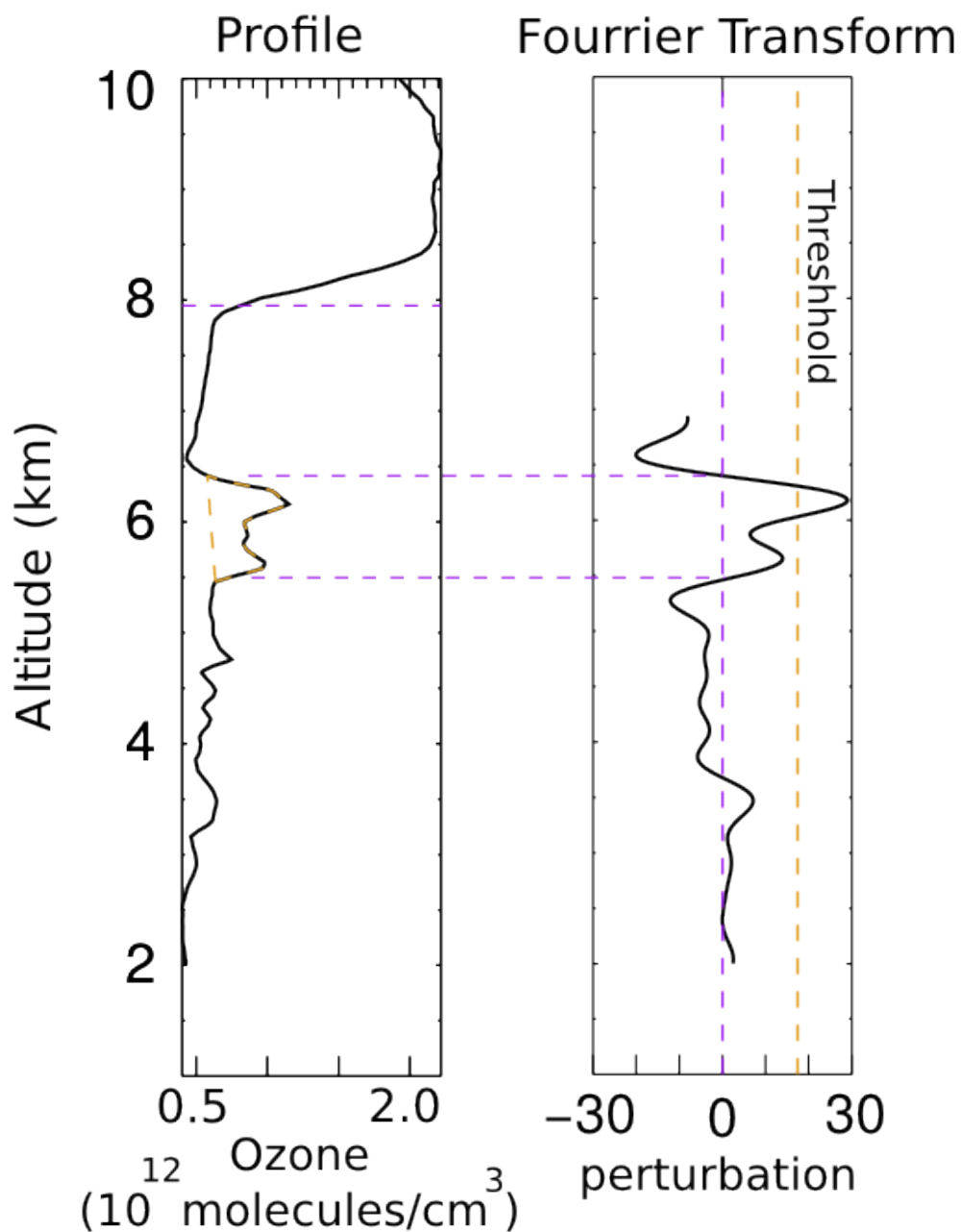


FIGURE 2.4: (a) An ozone profile between 2km altitude and the tropopause (indicated by the dashed vertical line). The 'flux' area shows the estimate of stratospheric impact on tropospheric ozone. (b) The 99th percentile of filtered ozone perturbations (green dashed line) and the technique for determining the vertical extent of the 'event' (red dashed and solid lines).

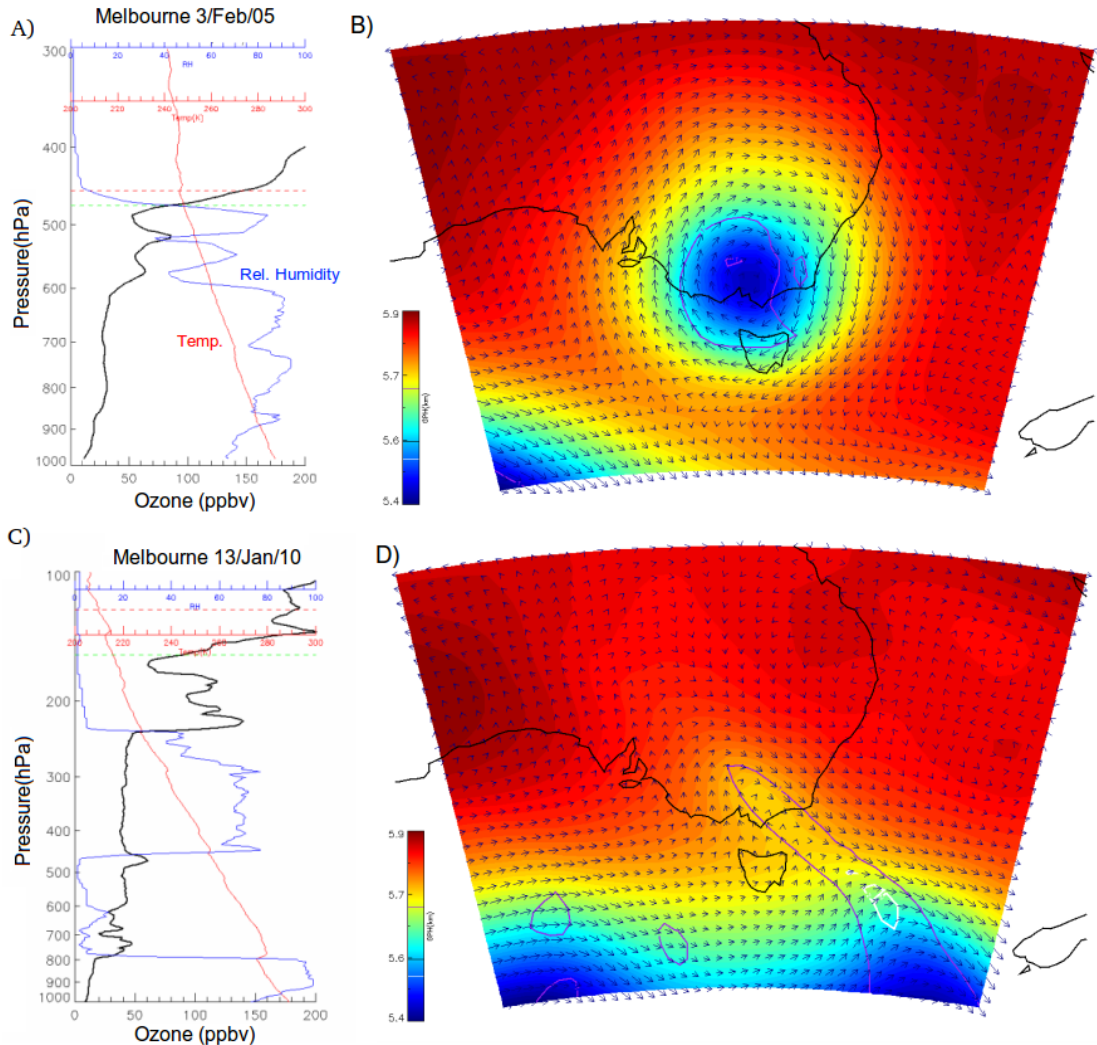


FIGURE 2.5: Vertical profiles show ozone ppbv (black line), relative humidity (blue line), and temperature (red line) for (a) 3 February 2005 and (c) 13 January 2010. Synoptic weather maps show the 500 hPa pressure level taken from the ERA-Interim reanalysis on (b) 3 February 2005 and (d) 13 January 2010. Vectors show wind direction and speed while the colour indicates the geopotential height. Also visible are the line contours of potential vorticity units, 1 PVU in purple and 2 PVU (often used to determine dynamical tropopause height) in white.

most commonly occur at 6 – 10 km above Melbourne and below 8 km at Davis but are distributed more evenly in altitude at Macquarie Island.

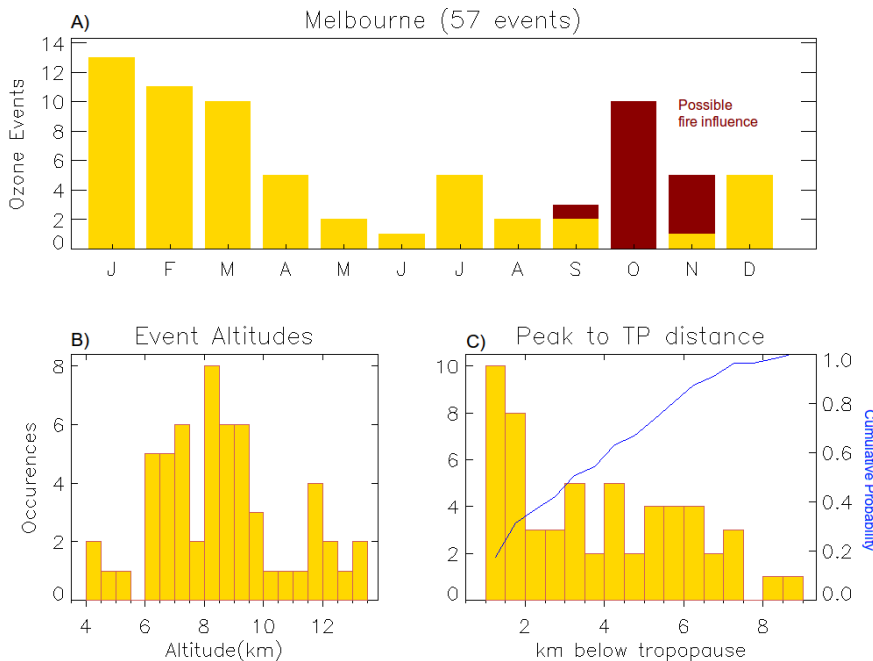


FIGURE 2.6: The climatology of STT events at Melbourne: (A) Events sorted by month from the entire Melbourne ozonesonde dataset. The events filtered out as possibly smoke plume influenced are indicated in red. (B) The occurrence distribution of the ozone peak altitude. (C) The distance between the ozone peak and the tropopause (bars) and the cumulative probability function of these distances (blue line).

## 2.4 Stratosphere to Troposphere flux analysis

### 2.4.1 Determining a minimum estimate of stratospheric influence

Determining how much ozone is transported from the stratosphere with only a two dimensional line vector of ozone concentrations is questionable. It is assumed that the two dimensional profile is a vertical straight line, which accurately represents the ozone profile in the horizontal dimensions. A conservative estimate on stratospheric ozone influence is determined through analysis of the ozone spike above a baseline amount for each column. This is a lower bound as it ignores dispersed ozone, baseline enhancements, and any secondary peaks which may also be due to stratospheric transport.

Using our estimate of STT ozone flux (see section 2.3.3) we find a lower bound for the STT ozone flux over each of our three sites, excluding possible fire influence. Figure 2.9 shows the climatological mean fraction of total tropospheric column ozone attributed to stratospheric ozone intrusions at each site, on days when an STT event occurs. These flux amounts are calculated after removal of the biomass burning events, although leaving the burning events in changes the means by less than 5%. The mean fractions of stratospheric ozone are 2–4%, although the largest fractional ozone in the tropospheric column attributed to stratospheric air exceeds 10% at all locations.

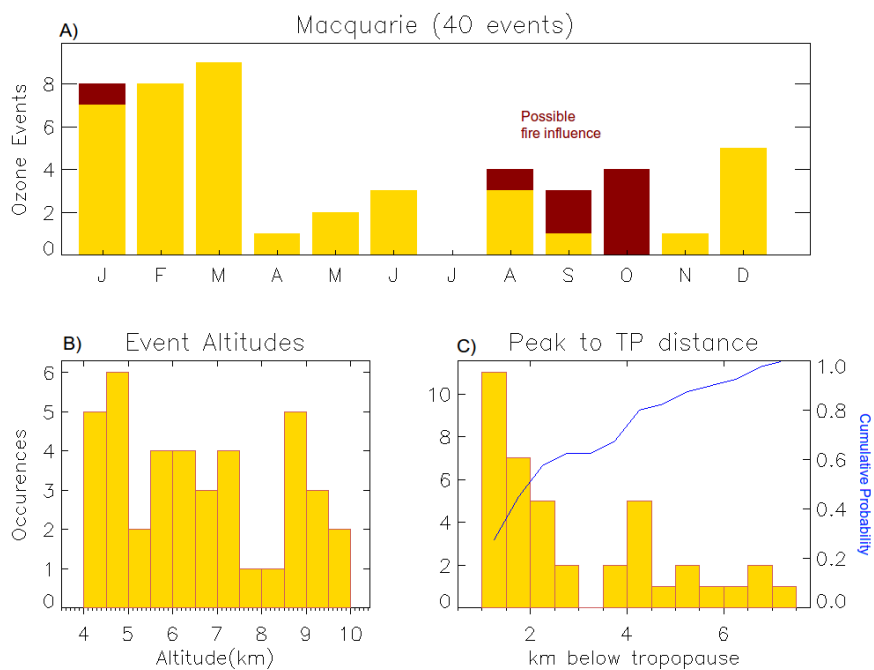


FIGURE 2.7: As for Figure 2.6 except showing the Macquarie Island STT events.

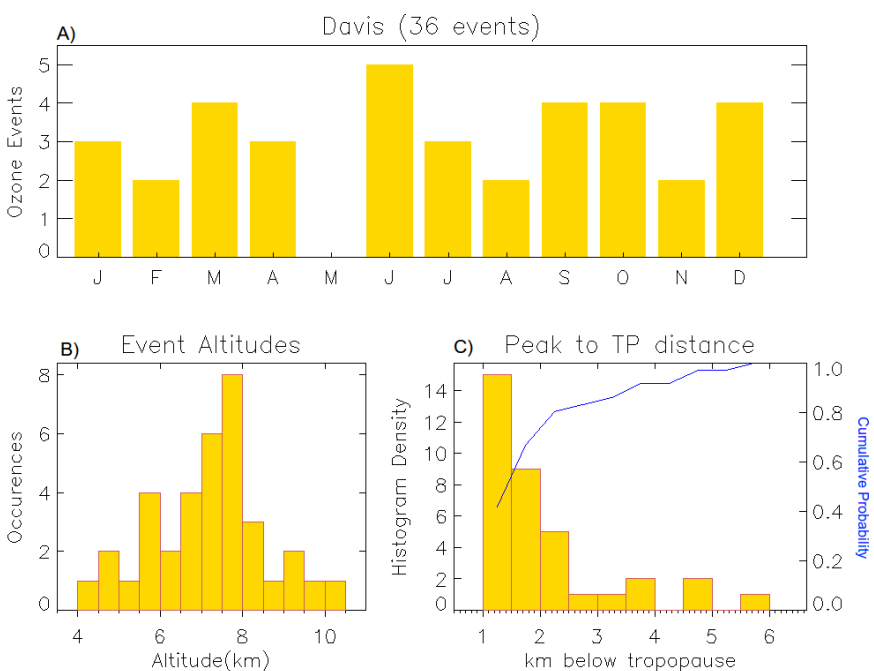


FIGURE 2.8: As for Figure 2.6 except showing the Davis STT events.

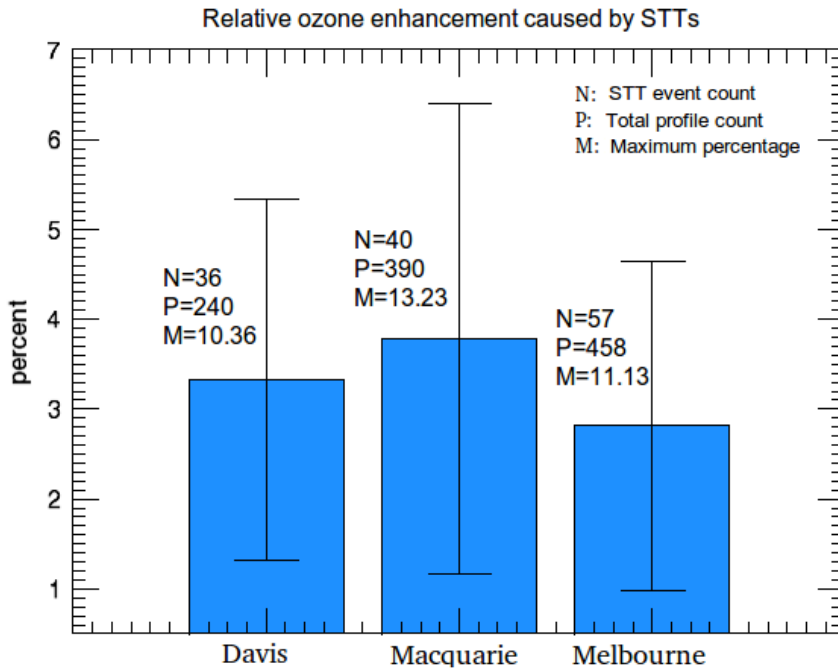


FIGURE 2.9: Fraction of total tropospheric column ozone attributed to stratospheric air intrusions during STT events. Error bars indicate one standard deviation.

## 2.5 Non-STT influences on ozone at southern latitudes

### 2.5.1 Fire Plumes

Ozone production due to fire smoke plumes is complex and affected by photochemistry, fuel nitrogen load, and atmospheric plume interactions both during transport and at the plume's destination. Ozone precursors include nitrogen oxides ( $NO_x = NO + NO_2$ ) and non methane volatile organic compounds (NMVOCs). Large biomass burning events emit substantial ozone precursors, some of which are capable of being transported far from their origins.  $NO_x$  can be transported far downwind due to peroxyacetyl nitrate (PAN) thermal decomposition and this can lead to enhanced ozone far from the source of a fire (Jaffe and Wigder, 2012).

Pak et al., (2003) show a tropospheric ozone spike over SE Australia in September and using back trajectories suggest that the air masses over Melbourne on this day also passed over South Africa and the higher altitude air also passed through South America. The Australian fire season spans most of the year, sweeping southwards as shown in figure and may occasionally affect the ozone columns above either of Macquarie and Melbourne. However, the influence from regional burning is unlikely to affect the ozone concentration above 4 km altitude and most of the smoke from the northern half of Australia is not transported over these sites.

South of  $10^\circ S$ , Jaffe and Wigder, (2012) estimates that 158 and 54 Tg per year of CO and ozone are emitted emitted and produced respectively by wildfires, with 50% uncertainty in the ozone production. Due to this possible source of ozone column perturbation, care must be taken to exclude biomass burning influence when analysing STE impacts.

### 2.5.2 Transport Exclusion

Biomass burning from the southern tropics (South Africa and South America) is a likely source of interference to and perturbation of ozone measurements. Transported BB plumes influence the southern mid latitudes generally between July and December, as indicated by the methane and CO enhancements ratio ( $\Delta CH_4/\Delta CO$ ) which averages 0.31 in this time (Pak et al., 2003).

One method of detecting transported emissions influences is through satellite column analysis as done in Sinha et al., (2004). Smoke plumes from biomass burning create a heavy haze as well as elevated CO concentrations which can be seen from satellites.

Ozone production due to fire smoke plumes is complicated and dependent on many chemical and meteorological factors. Using high CO levels as a proxy in order to determine where fire smoke plumes exist has been done in several studies (eg: (Edwards, 2003; Sinha et al., 2004; Edwards et al., 2006; Mari et al., 2008)). The AIRS (Atmospheric Infrared Sounder) instrument on board the AQUA satellite records, among other trace gases, column CO. The AQUA satellite overpasses most of the globe twice per day, using the data from the ascending mode swathes at local time 1330 allows some idea of the atmospheric CO on a given day.

In this work a visual inspection of vertical columns of CO (provided by NASA (AIRS3STD 2013)) over the southern hemisphere is used to exclude possible foreign smoke plume influence on the ozone profile at our three sites. Whenever high CO concentrations coincide with sonde detected ozone events it's possible that the tropospheric ozone spike could be due to transported chemicals. All occasions where these coincidences occur are removed. Using a scale of  $1e18$  up to  $3.5e18$  molecules/ $cm^2$  can show burning influence as exemplified in figure 2.10. Using 458 ozonesonde profiles over Melbourne, 72 ozone events are detected, of which 15 are discarded as possibly caused by transported fire smoke plumes. Over Macquarie island 48 events are detected from 380 ozonesondes of which 8 are discarded due to possible smoke influence. We also include on Figure 2.6 to Figure 2.8 the events which have possible fire influence. These events are concentrated in Spring at melbourne and Macquarie Island.

## 2.6 GEOS-Chem ozonesonde comparison

### 2.6.1 Comparing data to GEOS-Chem

Ozone sondes are useful for looking at specific locations with high resolution, and in this work they provide an estimate of both STT occurrence rates and STT ozone flux. This information can be used in conjunction with global scale information in order to extrapolate ozone transport over a large area. GEOS-Chem is used to simulate the global ozone concentrations. In order to check that the model is reasonable, some simple validation is performed comparing sonde data to colocated grid boxes in GEOS-Chem, using the tropospheric columns of ozone as the metrics. After the model is validated this way, an extrapolation is performed and the stratospherically sourced ozone is estimated over the latitude range from  $30^\circ S$  to  $75^\circ S$  (TODO: Update these numbers with final decided ones, and give a reason). Examination of the GEOS-Chem output also gives us an insight as to whether the simulation can be used on its own in order to estimate STT event distribution and magnitude.

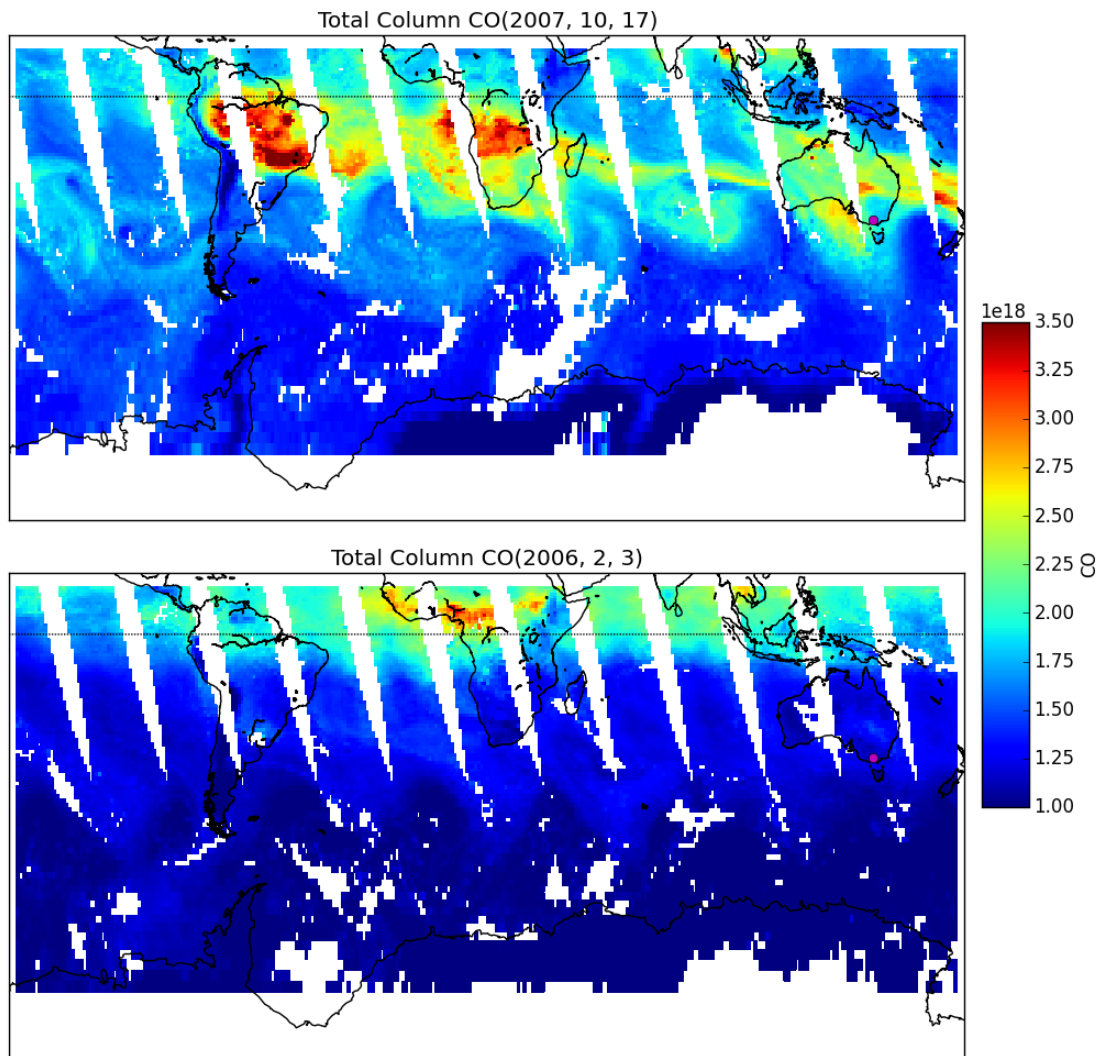


FIGURE 2.10: AIRS total column CO image showing two days separate days of swathes. The top panel shows an example of an excluded ozone event which could have been caused by a transported biomass burning plume on October 17th, 2007.

A secondary reason to compare ozonesondes to GEOS-Chem is to check that GEOS-Chem chemistry is reasonable and robust. Model validation at any scale increases confidence in the model as well as providing background information to scientists who seek to expand or improve the model.

GEOS-Chem is a global chemical transport model (Bey et al., 2001), which includes transport, emission, deposition, chemical production and destruction of ozone and 103 other trace gases throughout the troposphere along with stratospheric chemistry, including photolysis. Stratosphere-troposphere coupling is calculated using the stratospheric unified chemistry extension (UCX) (Eastham, Weisenstein, and Barrett, 2014), which includes a further 28 trace gases. Transport is driven by assimilated meteorological fields from the Goddard Earth Observing System (GEOS-5) maintained by the Global Modeling and Assimilation Office (GMAO) at NASA.

GEOS-Chem values used within this chapter are based on a simulation using UCX from 2004-2013, with 2004 used as a spinup year. The simulation uses  $2^{\circ}$  latitude by  $2.5^{\circ}$  longitude horizontal resolution, with 72 vertical levels from the surface to 0.1 hPa. Biogenic emissions of organic chemicals are determined by the Model of Emissions of Gases and Aerosols from Nature (MEGAN) version 2.1 extended by Guenther et al (Guenther et al., 2012). Anthropogenic emissions are given by the Emissions Database for Global Atmospheric Research (EDGAR) version 4.2. Our simulation was modified from the standard v10-01 to a fix a bug in the treatment of the Total Ozone Mapping Spectrometer (TOMS) satellite data used to calculate photolysis (see TODO:wiki entry for fix or supplementary). GEOS-Chem uses measurements from the Total Ozone Mapping Spectrometer (TOMS) satellite instrument with the Fast-JX photolysis rate solver customised for use in the stratosphere in order to simulate stratospheric ozone photolysis.

## 2.6.2 Determining tropospheric ozone from GEOS-Chem

GEOS-Chem allows certain diagnostics, along with any tracer, to be output at higher temporal resolution for a list of latitude and longitude based boxes. Storing output every six hours allows an examination of vertical profiles at a list of specific latitudes and longitudes during both day and night. Using the ozone mixing ratio ( $C_{O_3}$  in molecules  $O_3$  per molecule of air) at 72 vertical layers and the air density ( $N_{Air}$  in molecules per  $cm^3$ ), provides us with the ozone density profile ( $N_{O_3}$ ):

$$N_{O_3}[z] = C_{O_3}[z] \times N_{Air}[z]$$

where z is the vertical level index.

In order to determine the tropospheric ozone column ( $TC_{O_3}$  in molecules  $cm^{-2}$ ), we first use the modelled tropopause pressure (TPP in hPa) to determine where the troposphere ends. The TPP is used to determine how many vertical levels exist in the troposphere. This is done through comparison with the pressure edges of each level. The linear fraction (frac) of the level containing the TPP is then obtained from the pressure edges below and above the TPP (pb and pa respectively):

$$frac = \frac{p_b - TPP}{p_b - p_a}$$

At every time step, using the above calculations along with the layer heights (H in cm), the tropospheric ozone ( $TVC_{O_3}$  in molecules  $cm^{-2}$ ) is determined as follows:  $N_{O_3}[z] \times H[z]$  gives the vertical profile of molecules  $cm^{-2}$ , which is then summed up

to the TPP:

$$TVC_{O_3} = \sum_{z=0}^{z_{TPP}-1} (N_{O_3}[z] \times H[z]) + frac \times N_{O_3}[z_{TPP}] \times H[z_{TPP}]$$

where  $z_{TPP}$  is the index of the level containing the tropopause.

Figure 2.11 shows the time series of tropospheric ozone ( $TVC_{O_3}$ ) simulated over our three stations from January 1 2005 to January 1 2011. Coplotted as stars are the measured tropospheric ozone columns calculated using the GPH and ozone partial pressure recorded by the ozone sondes. The GEOS-Chem simulation uses horizontal resolution of  $2^\circ$  latitude by  $2.5^\circ$  longitude, and the profiles and totals above each site are actually the average over the horizontal area containing each station. There is good agreement between the modelled tropospheric ozone columns and the measurements, with matching seasonal cycles and magnitude. All three sites have a discernable yearly cycle, with Davis having the least spread as well as the greatest outliers. These outlying tropospheric ozone columns all occur during the July to September months (TODO: reasons for why? simulated summer turbulence?). Both Macquarie Island and Melbourne have more variance in their tropospheric columns. For both sites the data is more spread out over the winter months. This variability is shown in more detail in figure 2.12.

Figure 2.12 shows the yearly averaged tropospheric ozone column over our three sites. This figure is created using the monthly averages along with their standard deviations. Melbourne has the largest tropical ozone column throughout the year, with a summer peak and winter minimum. Davis has the lowest ozone levels, with an opposite seasonal cycle to that of Melbourne. At Macquarie Island, there is a more subtle seasonal cycle, with slightly more ozone occurring in winter than in summer.

### 2.6.3 Ozone profiles compared with GEOS-Chem

GEOS-Chem provides 72 vertical levels of data, of which about 30 will be in the troposphere. The ozone sondes generally have more than 100 vertical levels below the tropopause. Interpolating the vertical levels to a standard set of altitudes allows an examination of both the mean ozone profiles and the standard deviation at each altitude. For each of the GEOS-Chem and sonde vertical profiles, the data is interpolated to 100 points between 0 and 14 km, at which the mean and standard deviation is determined for each month.

Figures 2.16-2.18 show the simulated monthly averaged ozone profile at Davis, Macquarie Island, and Melbourne respectively. The shaded areas show  $\pm 1$  standard deviation, while the horizontal dotted line shows the mean tropopause height. The effect of pollution and mainland influence can be seen over Melbourne, mostly during the summer months (DJF), as the lower altitudes have increased ozone mean as well as more variance. Also the yearly cycle of tropopause height for each site is noticeable, and it matches the ozonesonde recorded tropopause seasonal cycle. Examining the mean profiles at particular hours only shows a noticeable difference (not shown unless someone tells me to) over Melbourne, the other two stations are very similar regardless of which hour we examine.

Figures ??-?? show the measured monthly averaged ozone profile at Davis, Macquarie Island, and Melbourne respectively. At Davis, the tropopause level is slightly lower in summer and autumn than in winter and spring. This yearly variation matches the tropopause heights simulated by GEOS-Chem, and is opposite to the yearly tropopause height cycle seen in Melbourne. Macquarie does not have a seasonal cycle of tropopause

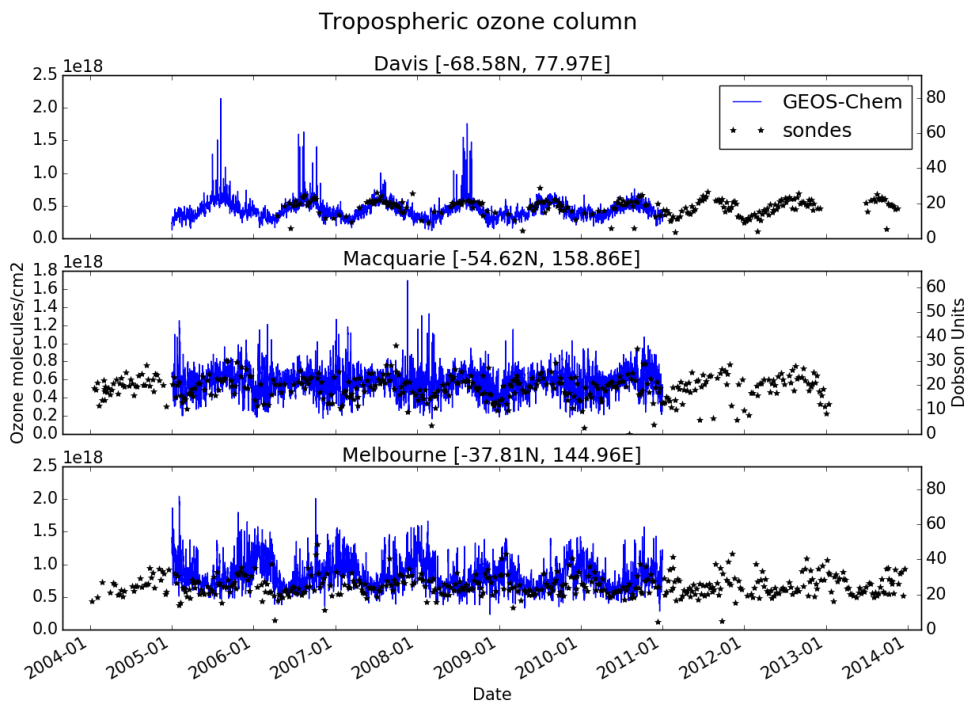


FIGURE 2.11: Tropospheric ozone in molecules  $\text{cm}^{-2}$  every six hours simulated by GEOS-Chem (blue line) from January 1 2004 until December 31 2010. The ozonesonde calculated tropospheric ozone columns are shown as stars, each representing one measurement.

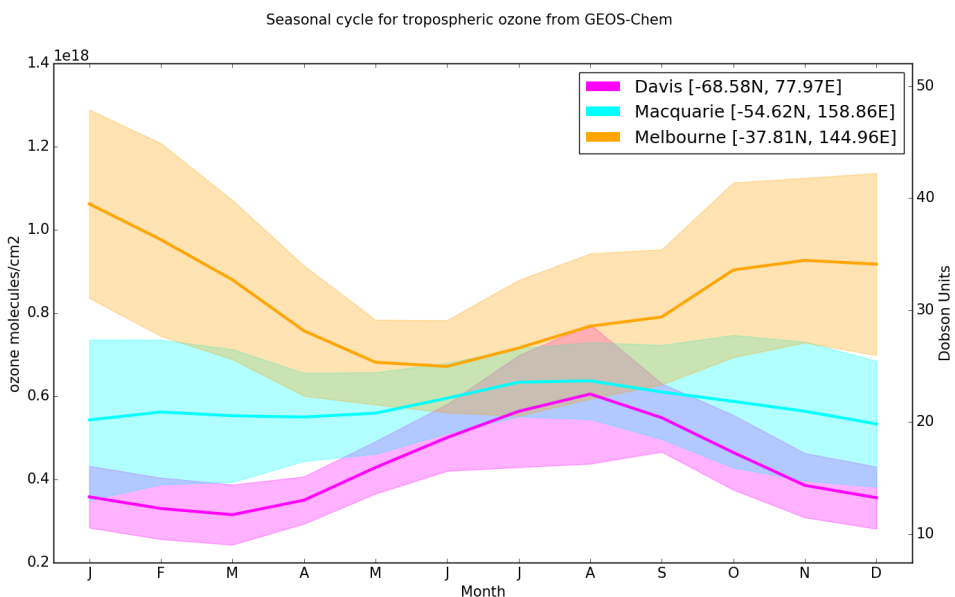


FIGURE 2.12: Tropospheric ozone in molecules  $\text{cm}^{-2}$  seasonal cycle simulated by GEOS-Chem from January 1 2004 until December 31 2010. The monthly averages are taken for each year and the mean plotted with one standard deviation shaded.

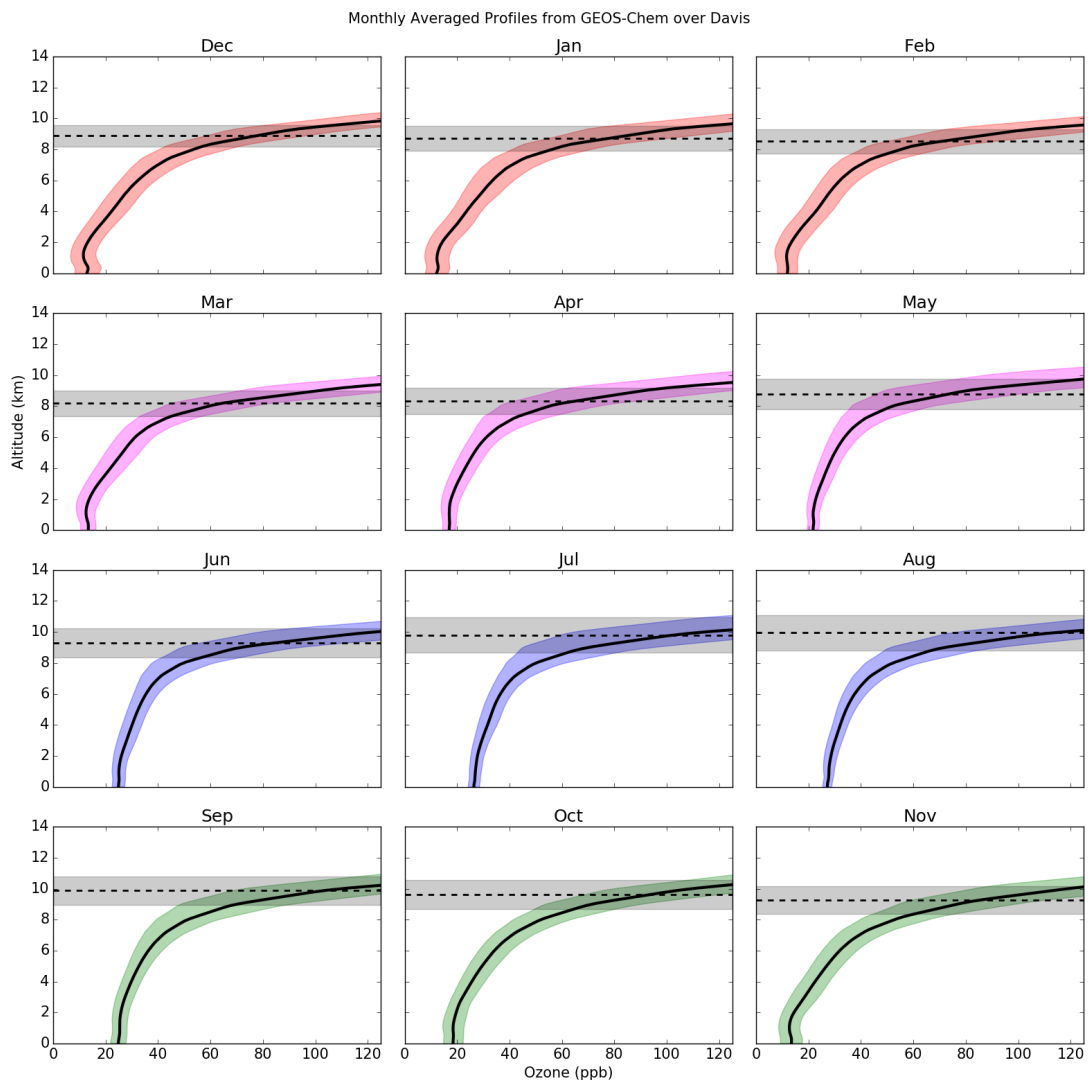


FIGURE 2.13: Tropospheric ozone (ppb) simulated by GEOS-Chem over Davis from January 1 2004 until December 31 2010, averaged monthly. Horizontal dotted line shows the mean tropopause height, shaded areas show one standard deviation.

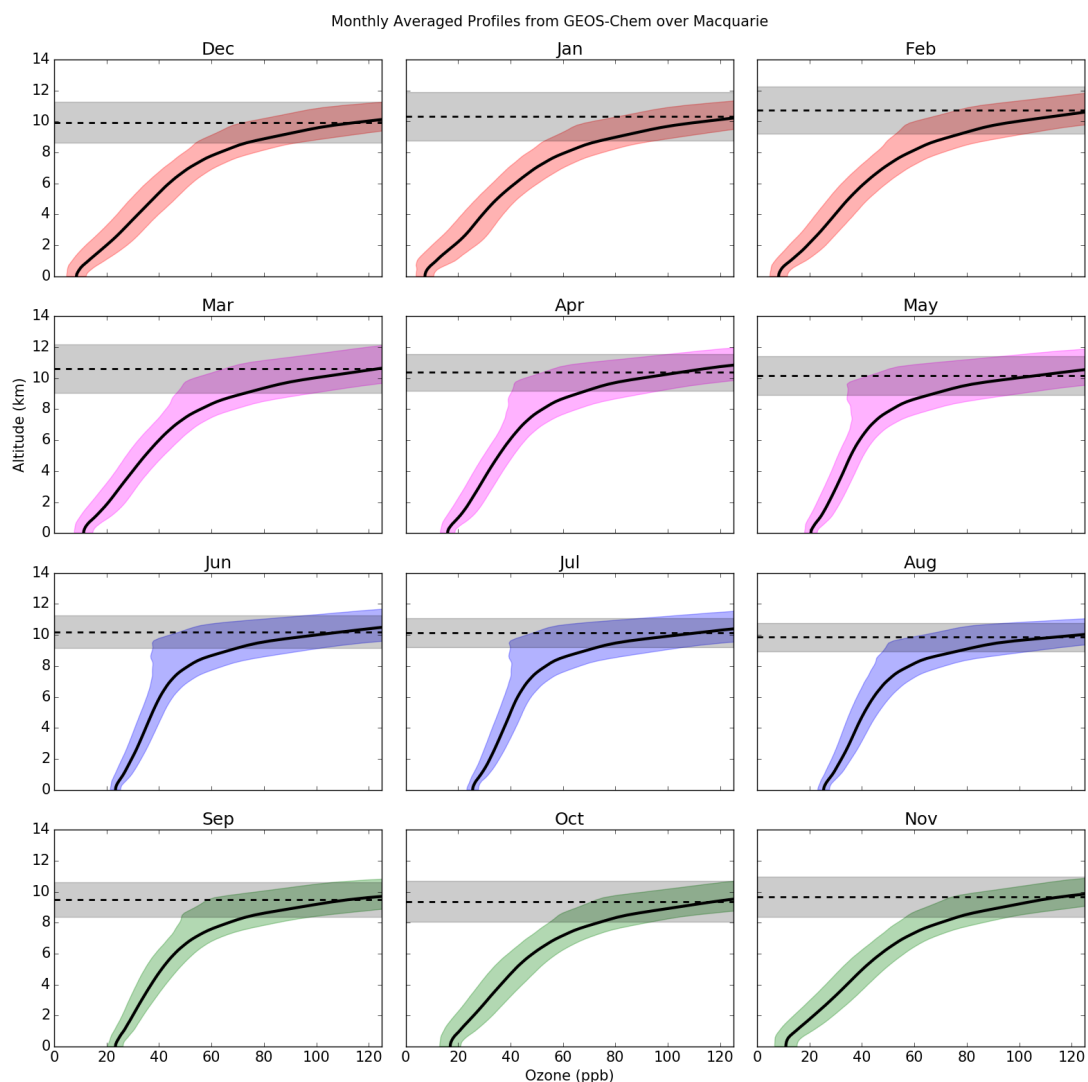


FIGURE 2.14: As figure 2.16 over Macquarie Island.

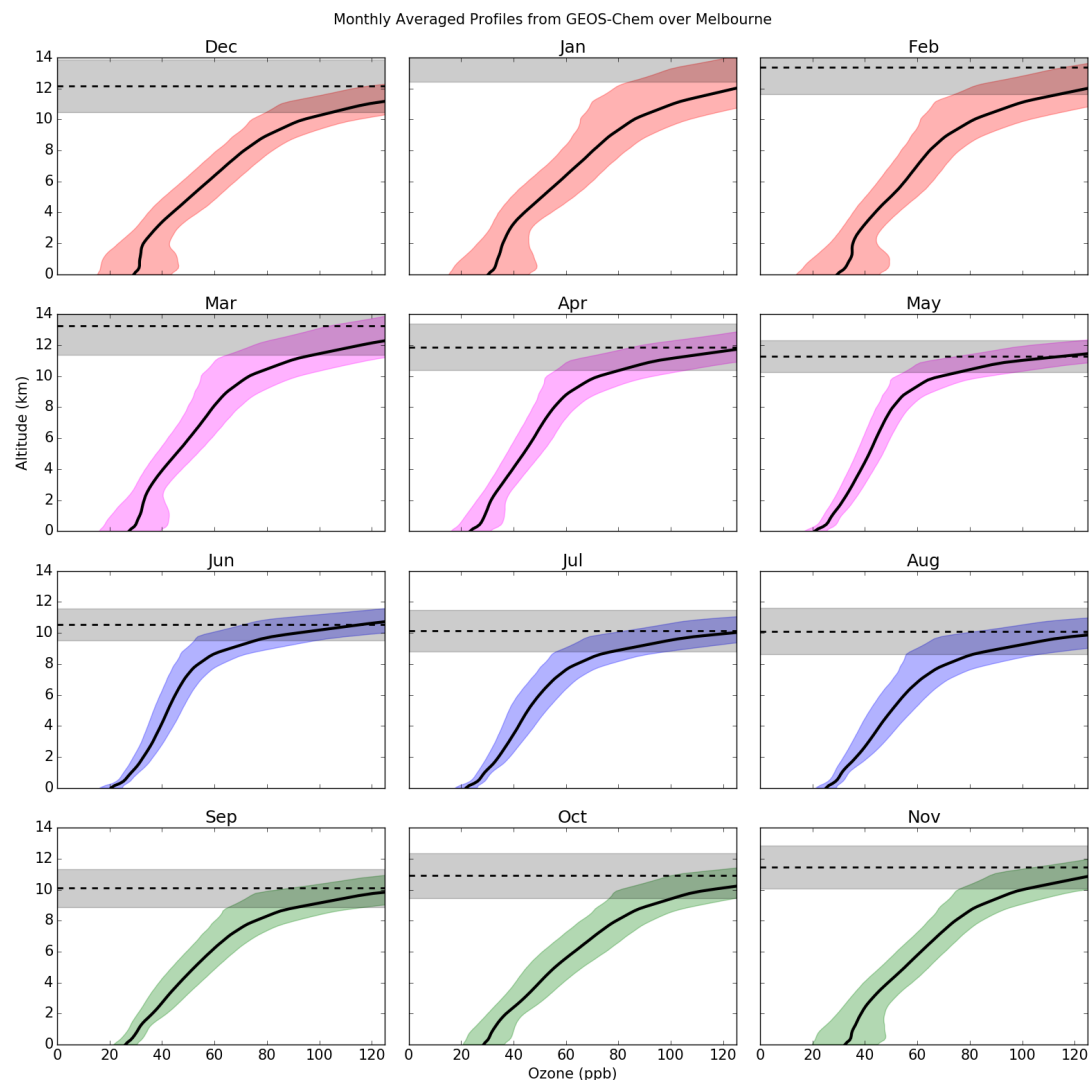


FIGURE 2.15: As figure 2.16 over Melbourne.

heights, which agrees with the GEOS-Chem profiles, although the GEOS-Chem tropopause heights are slightly higher at all months. For Melbourne the gradient of increasing ozone with increasing altitude is stronger in the GEOS-Chem output than the sonde measurements.

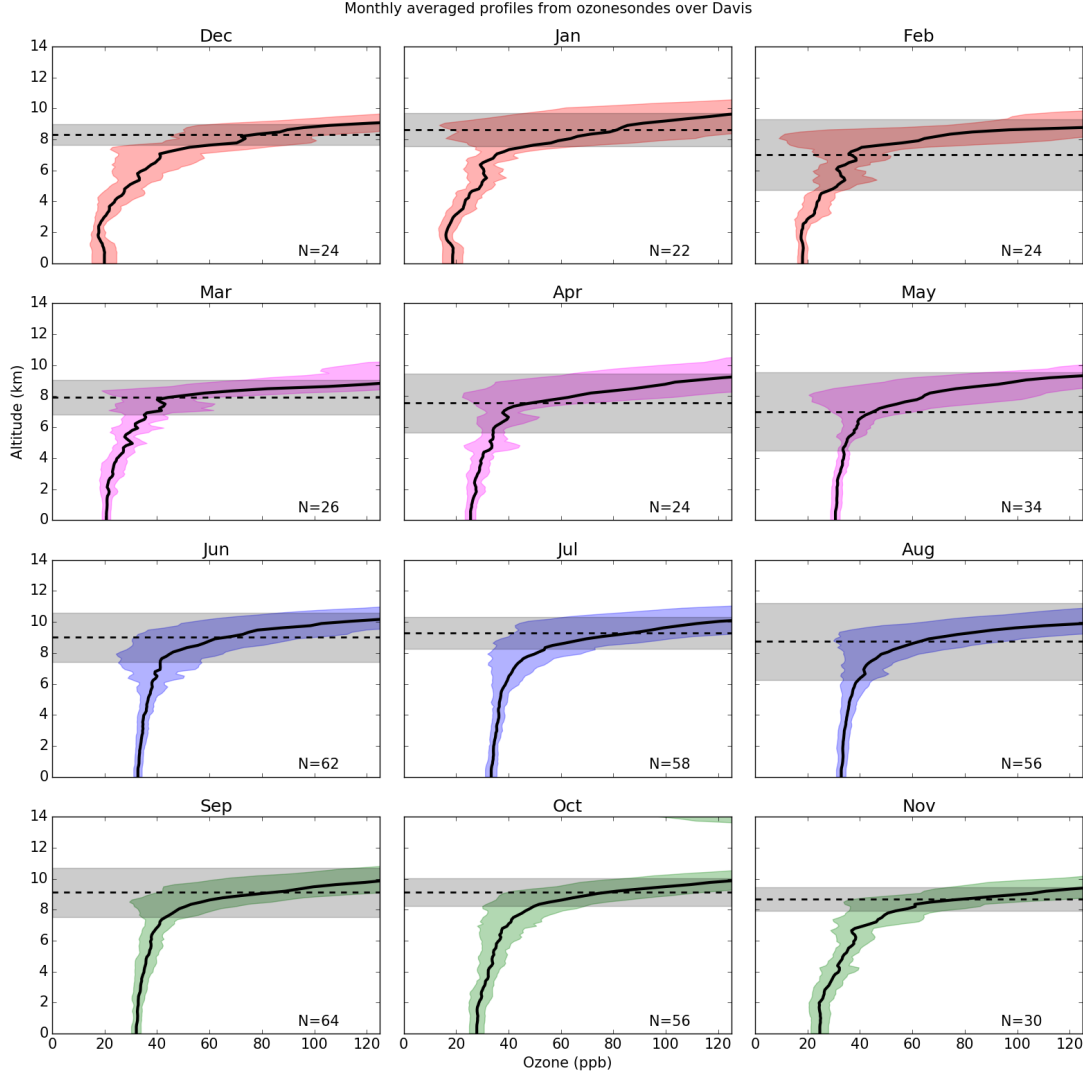


FIGURE 2.16: Tropospheric ozone (ppb) measured by ozone sonde over Davis, averaged monthly. Horizontal dotted line shows the mean tropopause height, shaded areas show one standard deviation.

Although GEOS-Chem reasonably matches the ozonesonde tropospheric ozone column, it does not have the resolution required to capture STTs. Figure 2.19 shows the best and worst comparisons of ozone profiles up to 14 km between the ozonesondes and GEOS-Chem. The model output is shown in red, and is the average over  $2^{\circ}$  latitude by  $2.5^{\circ}$  longitude which contain the respective sonde release site. The vertical resolution from GEOS-Chem is too low to allow detection of STTs, there are roughly 30 vertical levels up to the tropopause, while sondes have upwards of 100. These best and worst examples are determined qualitatively, and are shown as examples of the model-measurement differences.

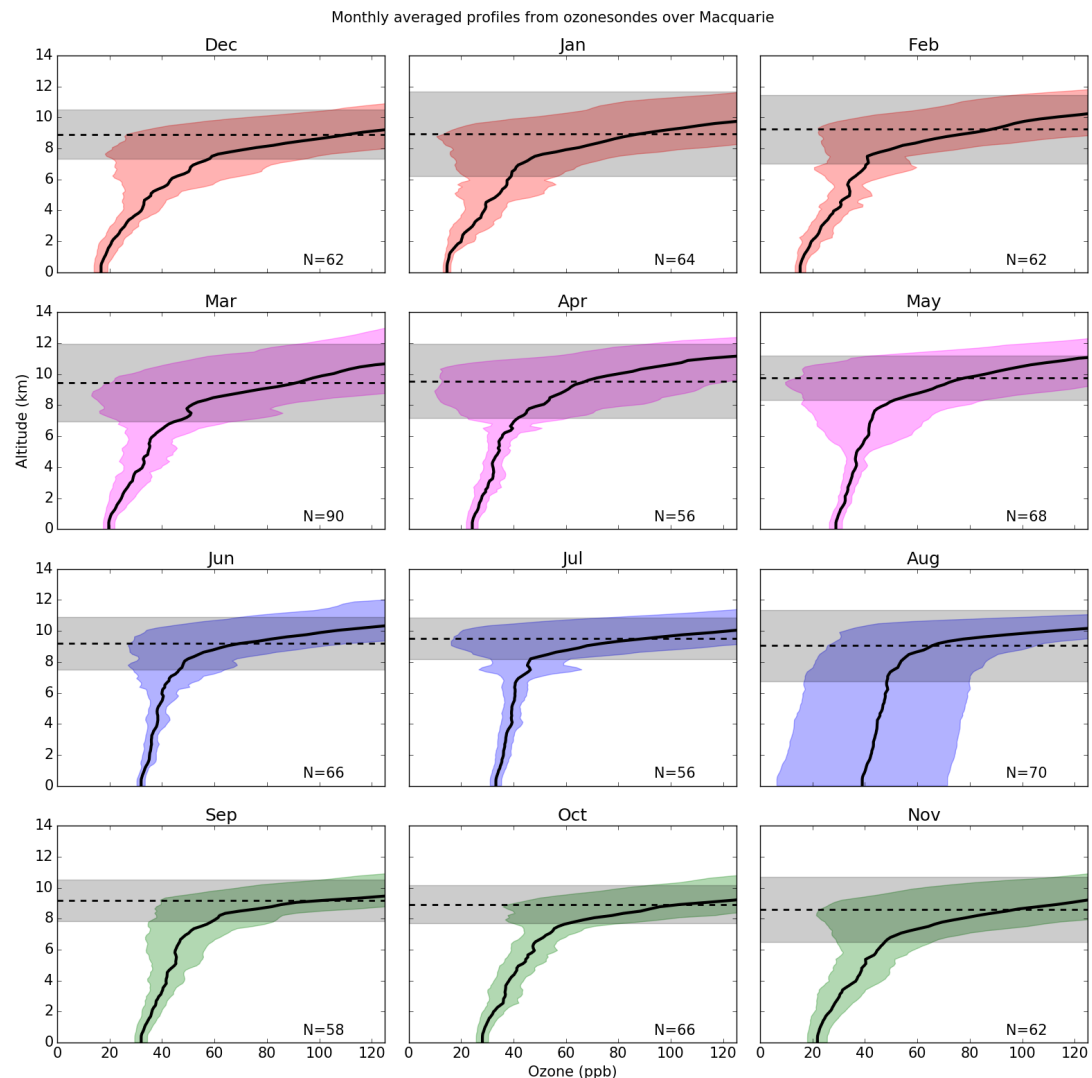


FIGURE 2.17: As figure 2.16 over Macquarie Island.

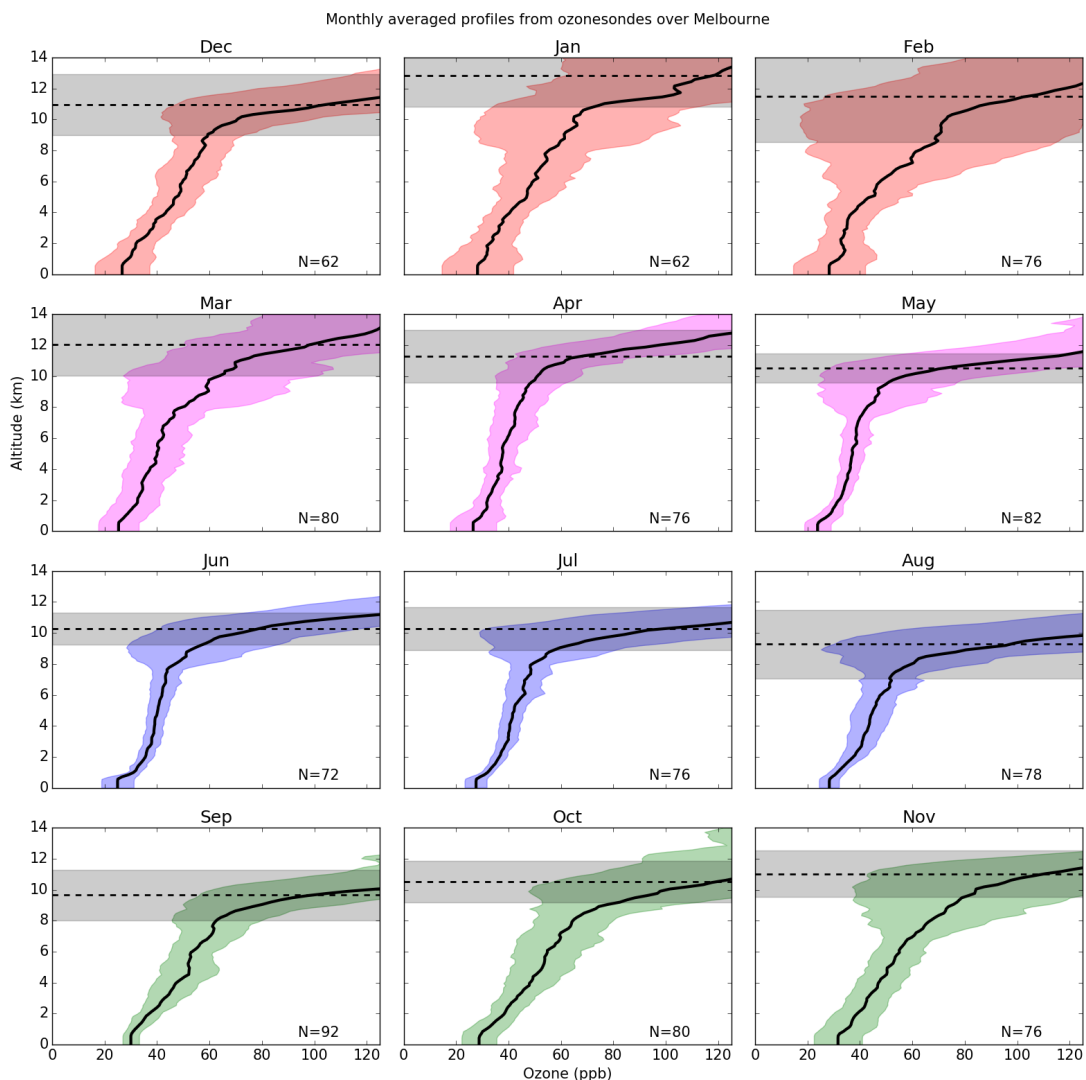


FIGURE 2.18: As figure 2.16 over Melbourne.

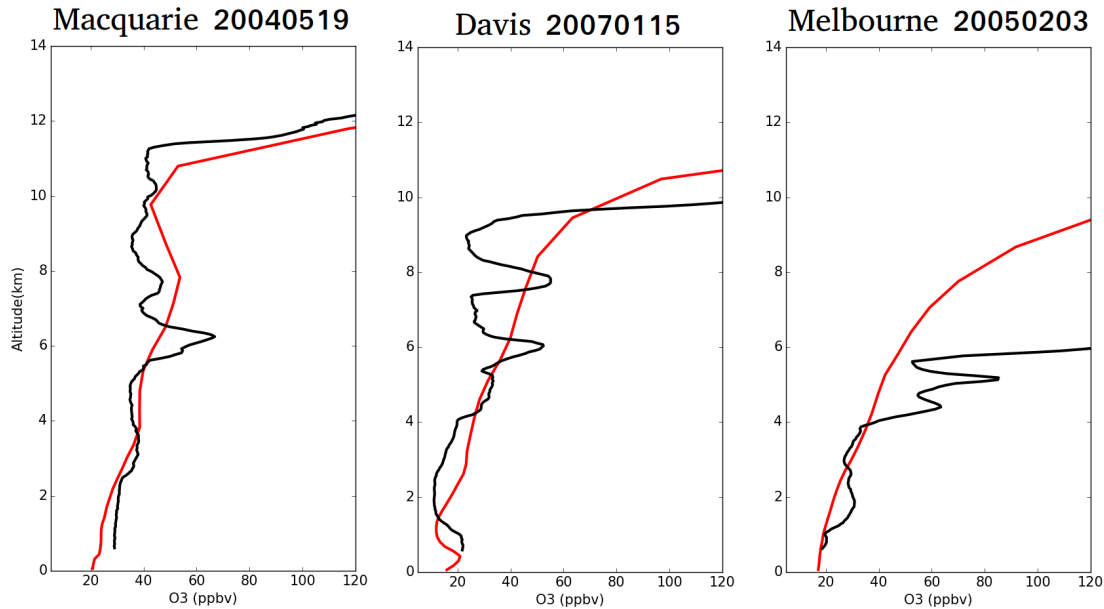
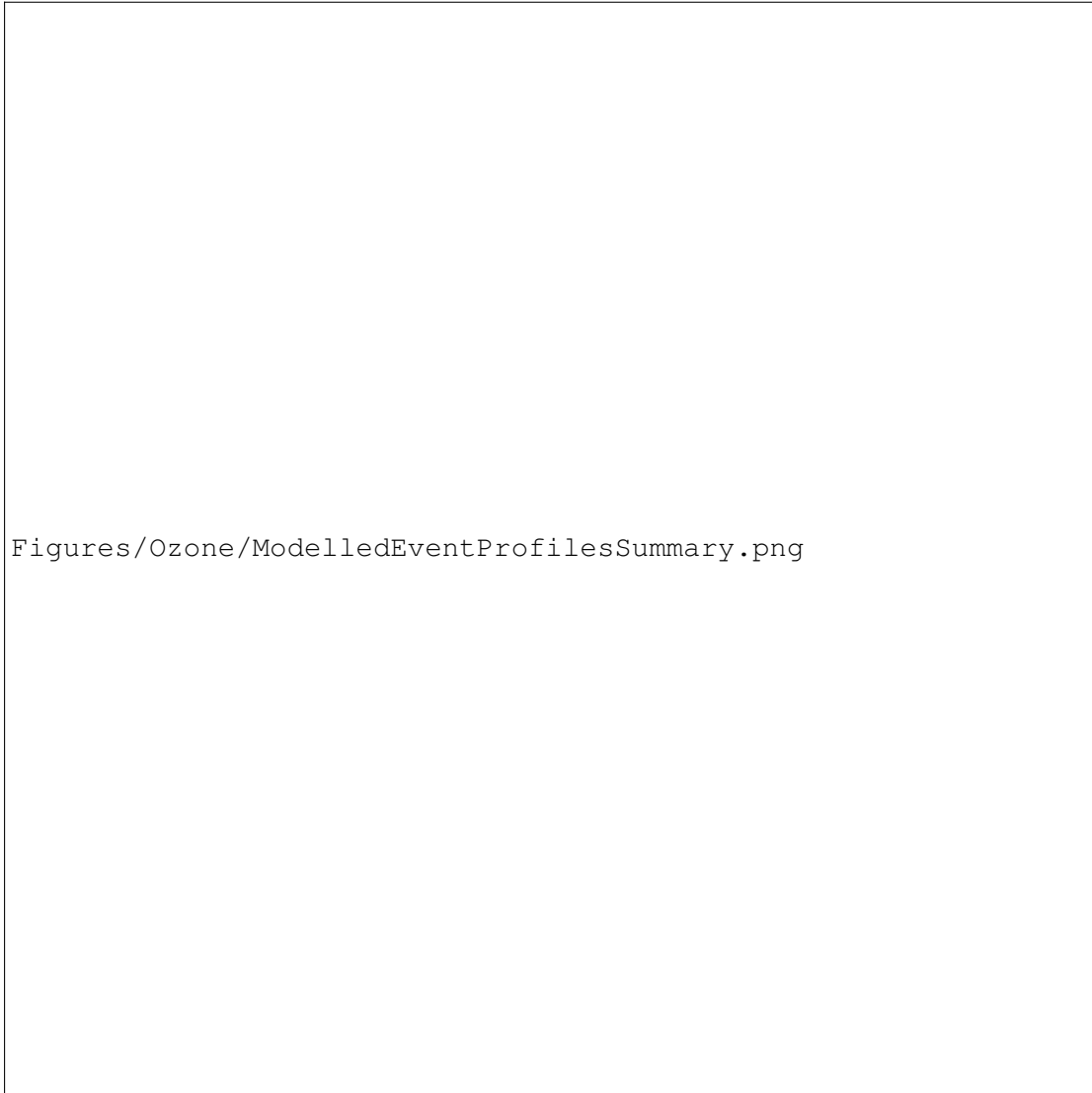


FIGURE 2.19: Ozonesonde profiles (black) against GEOS-Chem profiles (red) for three different dates, one over each site. The dates were picked based on subjective visual analysis as follows: left is the best match - May 19th 2004 over Macquarie, middle is an average case - January 15th, 2007 over Davis, and right is the worst match - February 3rd 2005 over Melbourne.

Considering the tropospheric ozone column, I determine the correlation between the GEOS-Chem simulated profiles and the ozone sondes using least squares linear regression. This assumes that the ozonesondes are the true values, while the model output is linearly dependant on them with the addition of some random error. This correlation is determined between simulated and measured tropospheric ozone in molecules  $\text{cm}^{-2}$ , for each site, for each day where there exists both a measurement and model output. Figure 2.21 shows the correlation between mean modelled tropospheric ozone column. The colours show which season the datapoints lie within, and suggest that seasonality plays a large role in this correlation; since summer and winter points are clumped at opposite ends.

Removing the monthly mean from each dataset, and dividing by that mean gives the relative monthly difference of each datapoint from the respective dataset determined annual cycle. Figure 2.22 shows the least squares correlation between ozonesonde relative monthly anomalies and their GEOS-Chem counterparts. Again the season is coloured, and removal of the monthly mean removes the summer and winter clumping which could be seen in figure 2.21. The correlation coefficients are lower, since the model and the measurement both show the same seasonal trends this is expected. What this plot shows is the correlation between simulated tropospheric columns being above (or below) average as well as the ozonesonde measured columns being above (or below) average. The slopes are not one to one, which suggests the variance in sondes is not well matched by variance in simulated output. This effect is strongest at the Davis and Macquarie Island stations, and is exacerbated when the seasonal cycle is removed.

(TODO: Update after model is rerun) Quantitatively, the modelled tropospheric



Figures/Ozone/ModelledEventProfilesSummary.png

FIGURE 2.20: Simulated and recorded ozone profiles above Davis, Melbourne, and Macquarie Island respectively from top to bottom. The column on the left shows the best matching profile, while the right shows the worst (determined qualitatively).

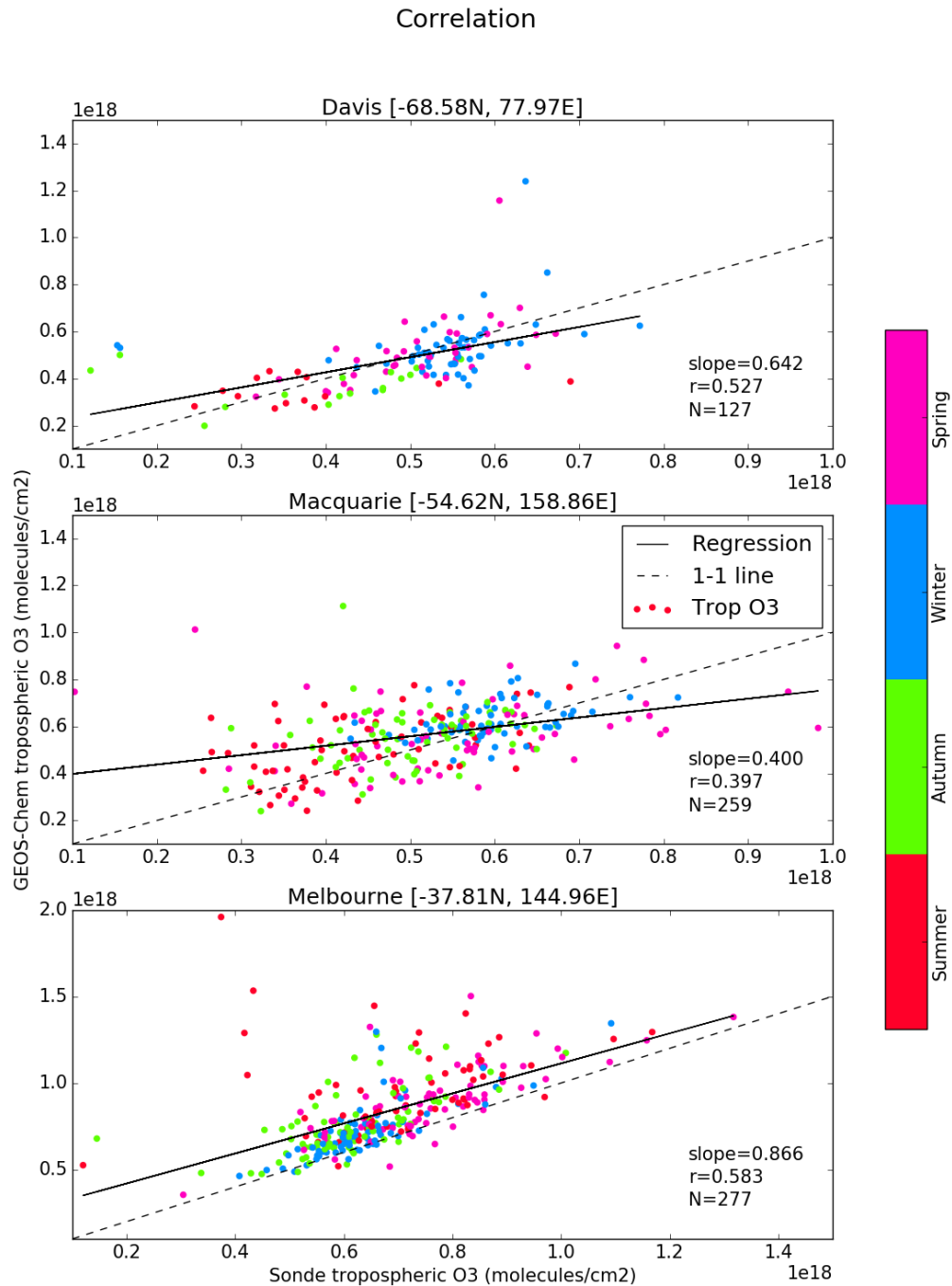


FIGURE 2.21: Correlation between tropospheric ozone column modelled by GEOS-Chem (vertical axes) and calculated from ozone sondes (horizontal axes). Points are coloured based on their season, shown by the colour bar on the right. The line of best fit (black) and one to one line (dashed) is also shown, note the axes are different for Melbourne.

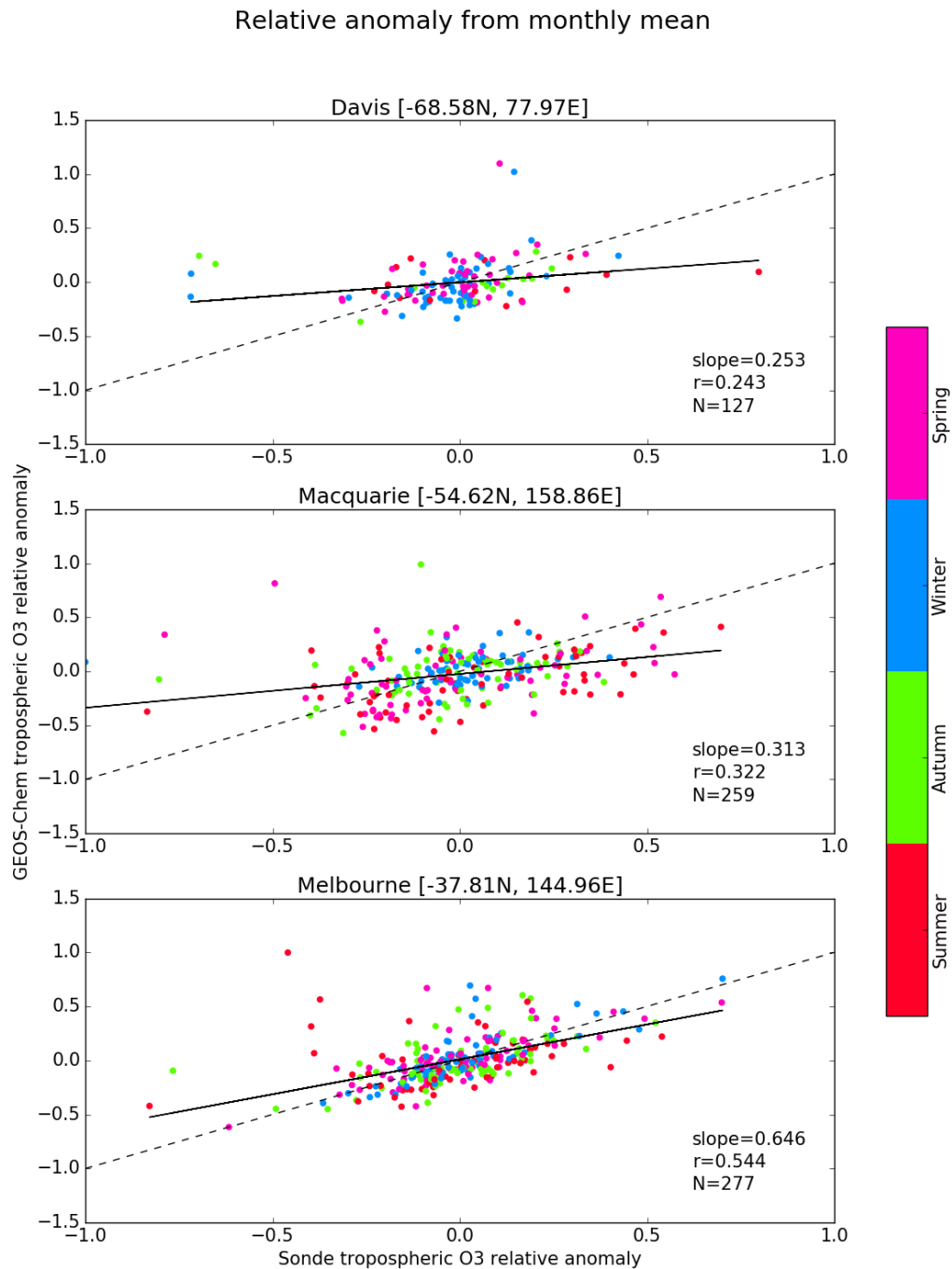


FIGURE 2.22: Correlation between relative difference of tropospheric ozone column from the monthly mean between profiles modelled by GEOS-Chem (vertical axes) and profiles calculated from ozone sondes (horizontal axes). The line of best fit (black) and one to one line (dashed) is also shown.

Site	direct		anomaly <sup>a</sup>		compared (N)
	r	r <sup>2</sup>	r	r <sup>2</sup>	
Davis	0.527	0.278	0.243		127
Macquarie Island	0.397	0.158	0.322		259
Melbourne	0.583	0.340	0.544		277

TABLE 2.1: Correlations between GEOS-Chem and ozonesonde tropospheric ozone column.

<sup>a</sup>Relative and normalised to monthly mean from GEOS-Chem and ozone sonde for respective data.

profile correlates reasonably well with the ozone sonde profiles, with correlation coefficients listed in table 2.1. Davis has a strong correlation ( $r = 0.527$ ) between sonde and simulated tropospheric column, which weakens greatly ( $r = 0.243$ ) when the season is removed. This suggests the model has the season and amplitude of tropospheric ozone fairly well simulated over larger time scales, but may lack accuracy when examining time periods of less than a few months. Macquarie and Melbourne are less affected by the removal of the seasonal cycle. Melbourne has a correlation coefficient greater than 0.5 with or without the seasonal cycle, showing that the model not only represents the larger time scales fairly well, but also has some accuracy catching days which are higher or lower than the monthly average.

TODO: show modelled daily cycle? Recall that the profiles are output every 6 hours, so as well as getting the overall profile average it is easy to determine the daytime and night time average by only looking at particular hours. GEOS-Chem uses GMT/UTC time, outputting 4 profiles per day at 0 hrs, 6 hrs, 12 hrs, and 18 hrs. The local offset in time at Davis, Macquarie Island, and Melbourne is 7 hrs, 11 hrs, 10 hrs respectively.

#### 2.6.4 Estimation of southern ocean STT flux

A simplistic calculation of how much ozone in the southern high latitudes is due to STT is made through the following method. STT event likelihood, multiplied by STT event tropospheric column contribution, multiplied by southern high latitude tropospheric ozone columns, averaged seasonally. The monthly likelihood of STT events is determined from the ratio of detected STT events over sonde launches. The monthly fraction of tropospheric ozone column due to STT is calculated from the averaging the STT contributions binned by month. The southern high latitude tropospheric column is computed from the monthly averaged tropospheric ozone columns output by GEOS-Chem, binned into months between 2005 and 2013 inclusive. This modelled ozone column is the average between 55°S and 85°S for all longitudes. The equation is straightforward once the required components are all computed:

$$Flux_i = l_i \times f_i \times tropO3_i$$

where i subscripts index the month (Jan - Dec), Flux is our estimate of STT contribution to the tropospheric ozone column, l and f represent the likelihood and contributary fraction of STT events respectively. Figure 2.23 shows the seasonal STT contribution calculated this way.

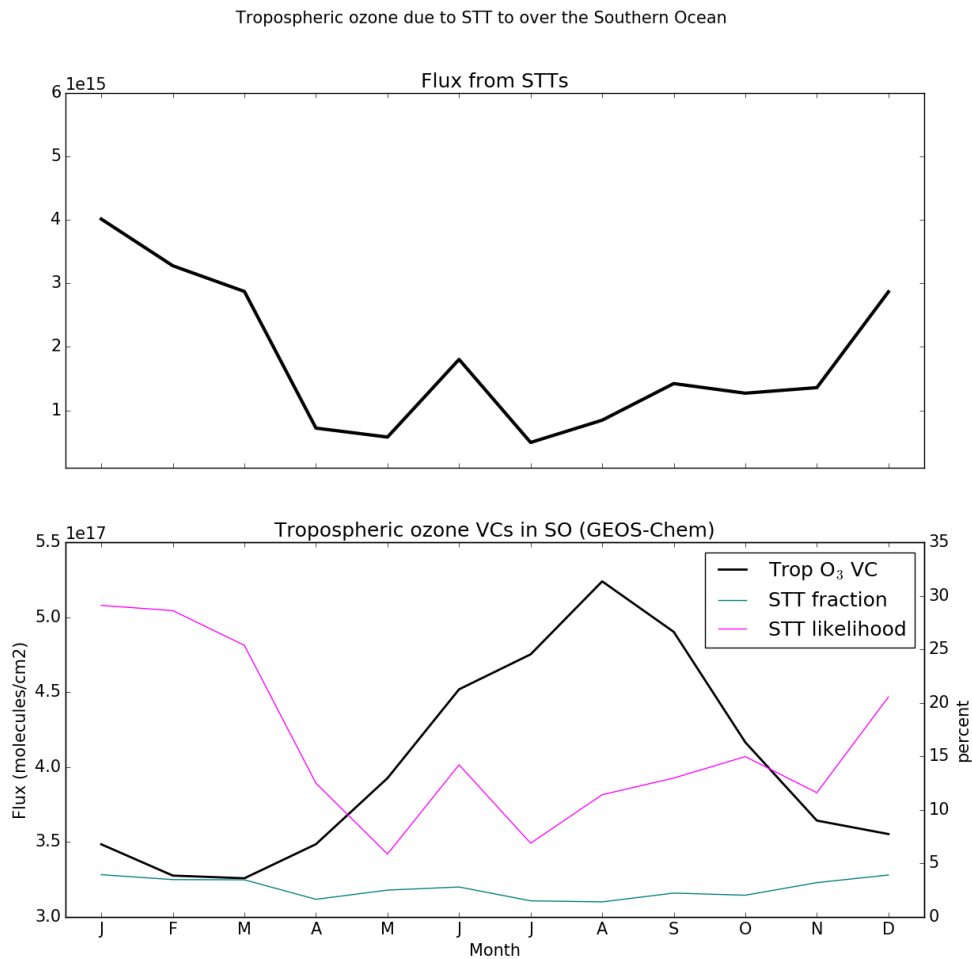


FIGURE 2.23: Top panel shows the estimated STT contribution to tropospheric ozone VC. Bottom panel shows the three factors multiplied together in order to produce the estimation. Units for l and f are on the right, while units for ozone VC amounts are on the left.

# Chapter 3

## Isoprene Emissions in Australia

### 3.1 Australian Biogenic Volatile Organic Compounds (BVOCs)

#### 3.1.1 Isoprene, Monoterpenes

Globally around 1150 Tg C yr<sup>-1</sup> of BVOCs are emitted (Guenther et al., 1995). 90% of these emissions come from plants and trees, with the most dominant species being isoprene ( $C_5H_8$ ) (about 61%), monoterpenes ( $C_{10}H_{16}$ ), and methanol ( $CH_3OH$ ) (Guenther et al., 2012; Lathière et al., 2006) (TODO: reread Guenther2012 for this sentence). Isoprene has a large impact on the oxidative properties of the atmosphere, as it reacts quickly with the OH radical to form  $RO_2$  and then in the presence of  $NO_x$  various OVOCs(largely HCHO) and other SOAs(notably ozone) are formed. The emissions of isoprene have been modelled at around 500  $Tg a^{-1}$  using relatively few plant phenotypes to set global emission factors, in Guenther et al., (1995).

Estimates of emissions of isoprene requires more work in order to generate confidence at a global scale. Due to isoprene being optically thin (see section 3.2.3) and having a short life time (around an hour) there are relatively few accurate measurements against which a comparison and verification can be made.

One problem with current estimates of biogenic VOC emissions in Australia is that the emission rates from various species of eucalypt and other flora are highly complex, depending on current and recent weather, temperature, tree age, tree health, etc (Guenther et al., 2012). With this complexity added to the diversity of tree species in Australia as well as sparse rural data collections it is hard to model and verify emissions. Isoprenoid emissions remain to be verified in Australia and the few monoterpene emission rates we have may be underestimated by a factor of 2-4 (Winters et al., 2009).

#### 3.1.2 Products and HCHO yield

Australian forests are strong emitters of both isoprene and monoterpenes, which go on to form various products including but not limited to secondary organic aerosols, oxygenated VOCs (OVOCs), ozone, OH, and  $HO_2$ . This production occurs over several steps, yields are often classed into at least two categories. First generation yield refers to the amount of HCHO produced per unit isoprene consumed by initial oxidation, total yield (sometimes molar yield) refers to time dependent yield of HCHO over multiple oxidation stages (Wolfe et al., 2016). Wolfe et al., (2016) define prompt yield as the change in formaldehyde measurement per unit change in initial isoprene emissions. Some argue that isoprene emissions are overestimated, due to the fact that they are based on relatively few measurements of isoprene emission factors (another; Winters et al., 2009; Fortems-Cheiney et al., 2012) TODO: read and cite paper mentioned in Fortems.

Species	Emissions <sup>a</sup> (Tg C per month)	Lifetime <sup>b</sup>	HCHO Yield <sup>c</sup> (per C reacted)	HCHO production <sup>d</sup> %
Isoprene	Y	n minutes	0.x	10
$\alpha$ -Pinene	Y	n minutes	0.x	10
$\beta$ -Pinene	Y	n minutes	0.x	10
HCHO	Y	n minutes	1.0	10

TABLE 3.1: HCHO yields from various species averaged over Australia during Summer.

<sup>a</sup>Calculated using GEOS-Chem emissions over Australia in January 2005.

<sup>b</sup>

<sup>c</sup>

<sup>d</sup>Production determined by dividing emission\*yield by the sum of all VOC emissions\*yields.

Isoprene production of HCHO depends on several factors, importantly  $\text{NO}_x$  levels have a direct effect on the fate of VOCs in the atmosphere. At higher NO mixing ratios (at least a few hundred pptv), organic peroxy radicals ( $\text{RO}_2$ ) react mostly with NO. At low NO (less than 10's of pptv), reaction with  $\text{HO}_2$ , other  $\text{RO}_2$ , and isomerization dominate the fate of  $\text{RO}_2$ . In low  $\text{NO}_x$  environments, reported HCHO yields from isoprene are from XtoY%, while in high  $\text{NO}_x$  environments this value is XtoY% TODO: these values from table. For monoterpenes the yields are around X, Y% for low, high  $\text{NO}_x$  respectively. Emissions and yields for various species including some terpenes can be seen in table 3.1. Wolfe et al., (2016) determine that going from  $\text{NO}_x = 0.1$  to 2.0 ppbv triples the prompt yield of HCHO, from 0.3 to 0.9 ppbv ppbv<sup>-1</sup> due to isoprene, while the background HCHO doubles. (TODO:and finish Wolfe2016 discussion paper for yields) TODO:go through atkinsenarey2003

Many of the HCHO yeilds from terpenoids are estimated through chamber studies which examine the products through their molecular mass and charge after mixing the compound of choice into a known volume of air. These conditions generally don't match those of the real world, where ambient air will have a coctail of these compounds as well as various reactants.

A proton transfer reaction mass spectrometer (PTR-MS) can be used to determine gas phase evolution of terpene oxidation products. This is done through analysis of mass to charge ratios ( $m/z$ ) which can be used identify chemical compounds.

Looking at Australian emissions from running GEOS-Chem and using using Yields provided by XYZ (another table) TODO: Fill out this table

Yields table looking at literature provided yields of HCHO.

### 3.1.3 Biomass Burning

One complication when computing HCHO yield from VOC emissions is biomass burning interference, as smoke plumes can contribute to column HCHO. Influence from biomass burning can be removed through measurements of acetonitrile and CO (eg: (Wolfe et al., 2016), TODO: other bb papers). Wolfe et al., (2016) disregard HCHO measurements when acetonitrile > 210 pptv and CO > 300 ppbv.

Species	HCHO Yield (molar % unless specified)	Notes	Source
Isoprene	63±10	High NO <sub>X</sub>	(Atkinson and Arey, 2003)
	57±6	High NO <sub>X</sub>	(Atkinson and Arey, 2003)
$\alpha$ -Pinene	28±3	20° C, Low NO <sub>X</sub>	(Lee et al., 2006) <sup>b</sup>
	X±3	X° C, X NO <sub>X</sub>	(Wolfe et al., 2016)
$\beta$ -Pinene	23±9	High NO <sub>X</sub>	(Atkinson and Arey, 2003)
	19±5	High NO <sub>X</sub>	(Atkinson and Arey, 2003)
$\beta$ -Pinene	65±3	20° C, Low NO <sub>X</sub>	(Lee et al., 2006)
	X±3	X° C, X NO <sub>X</sub>	(Wolfe et al., 2016)
$\beta$ -Pinene	54±5	High NO <sub>X</sub>	(Atkinson and Arey, 2003)
	45±8	High NO <sub>X</sub>	(Atkinson and Arey, 2003)

TABLE 3.2: HCHO yields from various species.

<sup>b</sup>Calculated through change in concentration of parent and product linear least squares regression.

<sup>c</sup>Calculated from satellite detected concentrations of HCHO.

<sup>d</sup>Calculated using PTR-MS and iWAS on SENEX campaign data.

### 3.1.4 MEGAN

One method used to estimate global isoprene (among other species) emissions is the Model of Emissions of Gases and Aerosols from Nature (MEGAN). MEGAN is a global model with resolution of around 1 km, and is used to generate the BVOC emissions used in various global chemistry models such as GEOS-Chem. MEGAN uses leaf area index, global meteorological data, and plant functional types (PFTs) to simulate terrestrial isoprene emissions. The various PFTs are used to generate emission factors which represent quantities of a compound released to the atmosphere through an associated activity. For example, an emission factor for isoprene within a forest would include the requirement of sunshine and suitable temperature. The schematic for MEGAN, taken from Guenther, (MEGAN), is shown in figure 3.1

MEGAN output in Australia is adversely affected by poor emission factor estimation, which is based on plant type classifications (PFTs) and local conditions like soil moisture and weather. An example can be seen in Müller et al., (2008) where MEGAN overestimates isoprene in northern Australia. Underestimates of monoterpenes emissions are also seen from MEGAN (TODO: ask Jenny what other paper showed this?), which may be due simply to underestimated emission rates for many Eucalypt species (Winters et al., 2009).

## 3.2 Satellite HCHO measurements

### 3.2.1 Satellite Retrievals

Satellites remotely sense atmospheric trace gases through irradiance measurements of solar light which has reflected off the earth's surface. These irradiances are affected by gases which exist along the reflected path of the light between the detector, the earth, and the sun. The irradiance is then used to estimate how much of a particular gas exists along the path of the incoming radiation, this estimate is called a slant column (SC). The retrieved SC of a particular gas (or species) can be transformed into a vertical column (VC) by scaling the path length in conjunction with accounting for the trace

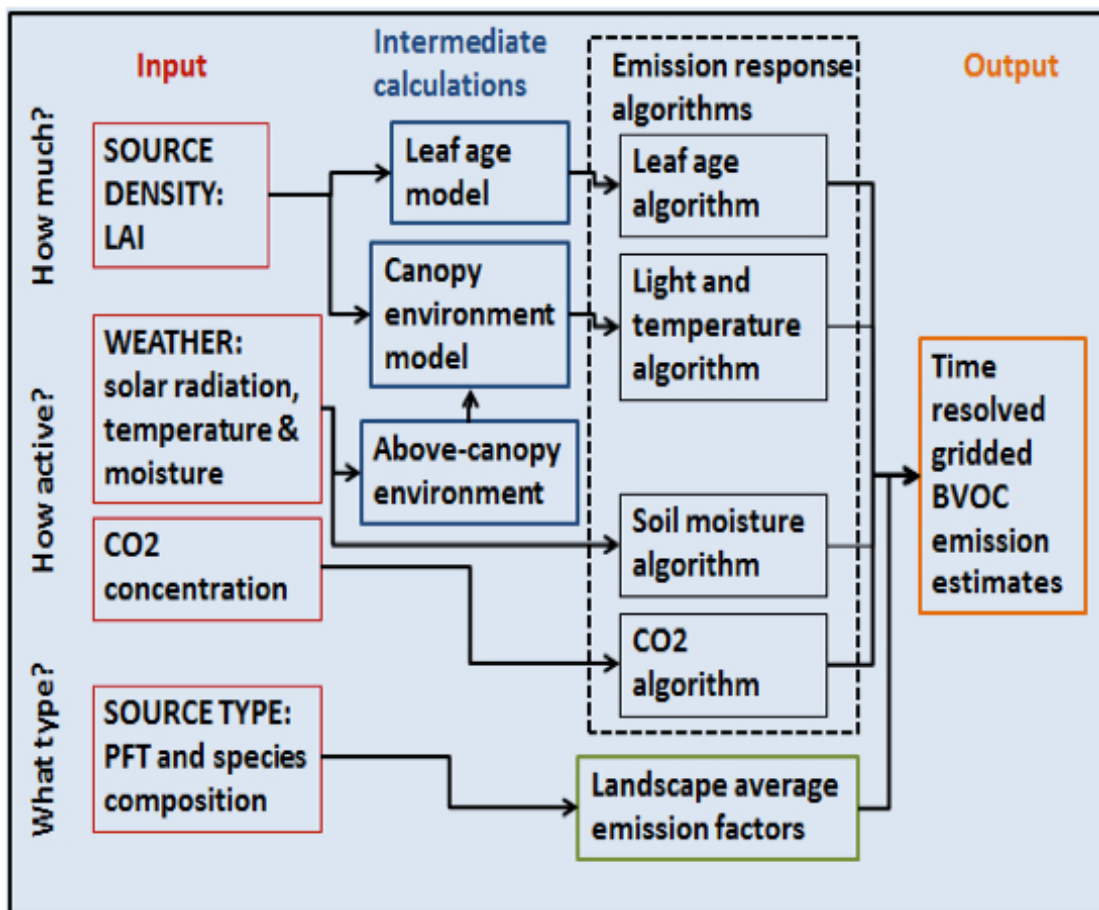


FIGURE 3.1: MEGAN schematic, copied from Guenther, ([MEGAN](#))

gas' light scattering properties. The scaling coefficient created to transform from SC to VC is called the Air Mass Factor (AMF).

One satellite is NASA's Earth Observing System's (EOS) Aura satellite, which houses the Ozone Monitoring Instrument (OMI), a near-UV/Visible Charged Coupled Device (CCD) spectrometer. Aura orbits the earth in a polar sun-synchronous pattern, circling the earth on a plane coincident with the sun and the north and south poles. OMI measurements are used to map several atmospheric trace gases, including NO<sub>2</sub>, SO<sub>2</sub>, BrO, HCHO, O<sub>3</sub>, and aerosols. OMI measurements occur from right to left on a band covering 115°, resulting in swaths of around 2600 km, with pixel sizes from 13x24 km<sup>2</sup> at nadir to 26x135 km<sup>2</sup> at the swath edges (Gonzalez Abad et al., 2015). The swaths cover the planet daily, although half of these are at night time and contain no useful near-UV/Visible information. From here on the word pixel is used to describe one data point retrieved by OMI, which will be located by latitude and longitude within OMI's data product.

Atmospheric HCHO can be measured using Differential Optical Absorption Spectroscopy (DOAS), as long as trace gases with similar features near the same wavelength are accounted for. TODO: Go through Vigouroux2012, Lee2005 or Volkamer2005 and detail the DOAS Retrieval of HCHO. A DOAS fit determines the total column amount of a trace gas along the path that the instrument views.

Uncertainty in a single pixel for OMI is quite high (todo: link to picture with one day average plus omi uncertainty). This can be reduced through temporal or spatial averaging, as the uncertainty decreases by a factor of  $1/\sqrt{N}$  where N is the number of observations being averaged. Taking the eight day gridded average with horizontal resolution of 0.25 by 0.3125 degrees (latitude by longitude) typically reduces the uncertainty from TODO: numbers. This can be seen more clearly in figure (TODO: image of OMI day retrieval compared to 8 day retrieval with uncertainties shown underneath).

### 3.2.2 OMI Algorithm (not DOAS)

The following information comes from the OMHCHO dataset documentation at Kurosu and Chance, (2014). The method of HCHO total column retrieval depends heavily on measured solar radiation. Radiance is directional radiant flux, expressed in Watts per square metre per steradian (a unit of angle used in three dimensional geometry). Irradiance is radiant flux received by a surface, expressed in watts per square metre. An OMI granule is the sunlit portion of an orbit (one day).

In version 3.0 of the OMI satellite data retrievals, HCHO is determined using the spectral window 328.5 nm–356.5 nm. The algorithm used is based on direct fitting of radiances and irradiances. An OMI radiance measurement over the remote Pacific ocean is used instead of an irradiance measurement. This means that the slant columns ( $\Omega_S$ ) are actually the difference with respect to the radiance reference column ( $\Omega_{S_0}$ ).

The model that is fitted to the measurements is made up of the radiance reference attenuated by HCHO contributions, inelastic (rotational Raman) scattering, and interferences from ozone, NO<sub>2</sub>, BrO, and the O<sub>2</sub>-O<sub>2</sub> collision complex. It includes additive and multiplicative closure polynomials and parameters for spectral shift and squeeze, and an undersampling correction and “common mode” spectrum. The spectral fitting results in HCHO slant columns, which are converted to vertical columns through a look-up table of AMFs (see section 3.2.6) Undersampling is a problem caused by the wavelength resolution of the instrument. Nyquist theorem requires that the sampling rate be at least twice the highest frequency of the signal in order to uniquely reconstruct it, otherwise the signal is undersampled (contains errors).

There are three main stages in the algorithm:

1. Radiance wavelength calibration, finding the optimum wavelength registration for a representative swath of radiance measurements, and determination of a common wavelength grid for auxiliary data (molecular reference cross sections, etc.).
2. On-line common mode spectrum calculation from residual fits of the central portion of the orbit. This accounts for systematic features not considered in the semi-empirical model.
3. Nonlinear least-squares fitting of all swath lines in the OMI granule. Fitting is performed individually for the 60 cross-track pixels in each swath line.

Cross-track striping is systematically higher or lower column values along a whole track. Several methods are used to reduce cross-track striping of the HCHO columns. These include soft calibration, which is the use of a daily radiance reference, and outlier screening in the fitting residuals.

### 3.2.3 Optical Depth ( $\tau$ )

Optical Depth, also called optical thickness, is the natural logarithm of the ratio of incident radiant power to transmitted radiant power through a material. In the atmosphere we are interested in the optical depth of various chemical species, and we use incoming solar radiation to determine this. The difference between solar radiation at the top of the atmosphere and the Earth's surface defines the atmospheric optical depth along the path of observation.

$$\tau = \ln \frac{\phi_e^i}{\phi_e^t}$$

where  $\phi_e^i$  is radiant flux seen at the earth surface,  $\phi_e^t$  is the solar radiant flux which arrives at the top of the atmosphere. In the atmosphere, optical depth can be due to several factors including scattering, chemical absorbance, and aerosols.

### 3.2.4 Scattering

Rayleigh and Mie scattering describe two kinds of particle effects on radiation passing through a medium. Rayleigh scattering is heavily wavelength dependent, and is the dominant form of scattering from particles up to roughly one tenth of the wavelength of the light. Mie scattering is more dominant from larger particles, and has less wavelength dependence. These scattering functions are described in detail at (TODO:section? reference?).

### 3.2.5 Absorption cross section and number density

TODO: Fill in this section, describe cross sections.

$\tau$  can be described using the attenuation cross section (the attenuation coefficient divided by its number density), with the following relation:

$$\tau = \int_0^l \alpha(z) \eta(z) dz$$

where  $\alpha(z)$  and  $\eta(z)$  represent absorption cross section in  $\text{m}^2 \text{ molecule}^{-1}$ , and number density in molecules  $\text{m}^{-3}$  respectively, and  $l$  represents the length of the path the light is travelling through.

### 3.2.6 Air Mass Factors

DOAS retrieval columns are an integration of a trace gas over the instrument's viewing path, in order to convert this total to a vertically distributed column a few assumptions and estimates are required. The vertical profile of a trace gas is assumed or estimated via a CTM, while its' scattering and radiative properties are calculated at all altitudes using an RTM. These properties are combined into a single array called the AMF which can be combined with a SC to produce a VC. AMFs are unique to each trace gas and due to their complexity and the influence of cloud cover they remain one of the larger error sources in remote sensing of BVOCs (TODO: source Millet 06 (Palmer et al., 2001)).

The latest OMI algorithm uses a shape factor determined from GEOS-Chem using 47 vertical levels at monthly temporal resolution and  $2^\circ$  latitude by  $2.5^\circ$  longitude horizontal resolution (Gonzalez Abad et al., 2015). The GEOS-Chem model has been substantially updated since then, and using the more recent version V10.01 to recalculate the AMF is performed within this thesis, details are shown in section 3.2.8.

The vertical distribution of a trace gas determined by CTM is independent of the vertically dependent observation sensitivity provided by RTM, which prevents model contamination of remotely sensed data. Two examples of this are GOME-2 products on the MetOp-A satellite and OMI products which use IMAGESv2 combined with LIDORT and GEOS-Chem with LIDORT for product processing respectively ( TODO: (Gonzalez Abad et al., 2015)). The actual formulation of an AMF is explained in section 3.2.8).

### 3.2.7 OMI HCHO data products

OMI Data products are generally classed into several categories, level 0 through to level 3. Level 0 products are sensor counts and orbital swath data, level 1B data calibrates and geo-locates the level 0 data. Level 2 products additionally have temporal, spatial, solar, and viewing geometry information, as well as quality flags. To create level 2 data slant column density is determined and then translated into vertical column density using an AMF calculated through radiative transfer models. Level 3 data is a temporally aggregated version of the this, for instance monthly or yearly averages.

In order to filter fire or anthropogenic influence on HCHO data one generally requires the level 2 data along with extra data such as MODIS and AATSR fire counts, and national or regional industrial emissions estimates.

### 3.2.8 HCHO Vertical Column Calculation

The method used here largely follows that of Palmer et al., (2001). The Beer-Lambert law of extinction allows spectroscopic measurement of absorbing chemical species (absorbers) in the atmosphere:

$$I_B = I_{B_0} e^{-\tau_s} \quad (3.1)$$

where  $I_B$ ,  $I_{B_0}$  is backscattered intensity with and without the absorber respectively, and  $\tau_s$  is the optical thickness of the slant column absorber (see section 3.2.3).

The AMF is needed to transform the slant column, as viewed by the satellite, into a vertical column:

$$AMF = \frac{\Omega_s}{\Omega_v} = \frac{\tau_s}{\tau_v} \quad (3.2)$$

where s and v subscripts refer to slant and vertical values, while  $\Omega$  represents a column of absorber in molecules  $\text{cm}^{-2}$ .

In the absence of atmospheric scattering a simple geometric AMF can be defined as a function of the zenith angle. The solar zenith angle ( $\theta_s$ ) and the satellite viewing angle ( $\theta_v$ ) are shown in image 3.2. However, in the UV-VIS region of the spectrum, Rayleigh and Mie scattering (see section 3.2.4) must be accounted for. Using equations 3.1 and 3.2 gives us an expression for the AMF which includes scattering:

$$AMF = \frac{\ln I_{B_0} - \ln I_B}{\tau_v} \quad (3.3)$$

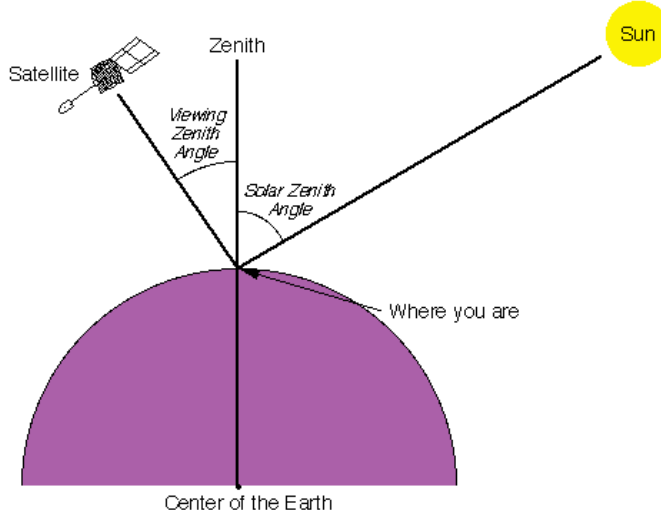


FIGURE 3.2: Solar and viewing zenith angles, image copied from Wikipedia, ([Solar zenith angle](#)), originally from a NASA website.

We use  $\nabla I = I_B - I_{B_0}$  to represent the change in intensity due to the absorber. Note that for optically thin absorption,  $\nabla I/I_B \ll 1$ , and we can use:

$$AMF = \frac{\ln \left(1 - \frac{\nabla I}{I_B}\right)}{\tau_v} \approx \frac{-\frac{\nabla I}{I_B}}{\tau_v} \quad (3.4)$$

$\nabla I$  can also be expressed as the integral of the absorption slices over optical depth increments:

$$\nabla I = \int_0^{\tau_v} \frac{\partial I_B}{\partial \tau} d\tau$$

which can be placed into equation 3.4:

$$AMF \approx \frac{-1}{\tau_v} \int_0^{\tau_v} \frac{\partial \ln I_B}{\partial \tau} d\tau$$

and rewritten as:

$$AMF = \frac{-1}{\tau_v} \int_0^\infty \frac{\partial \ln I_B}{\partial \tau} \alpha(z) \eta(z) dz \quad (3.5)$$

where  $\alpha(z)$  and  $\eta(z)$  represent absorption cross section in  $m^2 \text{ molecule}^{-1}$ , and number density in molecules  $m^{-3}$  respectively. This uses the attenuation cross section relationship to optical depth (see section 3.2.5).

To represent an average cross section weighted by the absorbing species' vertical distribution, intended to account for temperature and pressure dependence of  $\alpha(z)$ ,  $\alpha_e$  is defined as:

$$\alpha_e = \frac{1}{\Omega_v} \int_0^\infty \alpha(z) \eta(z) dz$$

This is the same as  $\tau_v = \Omega_v \alpha_e$ , which we can place into equation 3.5 to obtain:

$$AMF = - \int_0^\infty \frac{\partial \ln I_B}{\partial \tau} \frac{\alpha(z)}{\alpha_e} \frac{\eta(z)}{\Omega_v} dz$$

Defining  $w(z)$  as the scattering weights describing the sensitivity of the backscattered spectrum to the abundance of an absorber at altitude  $z$ :

$$w(z) = - \frac{1}{AMF_G} \frac{\alpha(z)}{\alpha_e} \frac{\partial \ln I_B}{\partial \tau} \quad (3.6)$$

and vertical shape factor  $S_z(z)$  representing a normalized vertical number density profile:

$$S_z(z) = \frac{\eta(z)}{\Omega_v} \quad (3.7)$$

Now the AMF can be expressed as

$$AMF = AMF_G \int_0^\infty w(z) S_z(z) dz \quad (3.8)$$

For this equation  $w$  is a function of atmospheric scattering which can be calculated using an RTM to determine the absorption cross section and optical thickness along the path.  $S_z(z)$  can be calculated using an apriori vertical profile, which may be sourced from any atmospheric chemistry model. Note that for level two non-gridded OMI satellite HCHO total column data, the  $w(z)$ ,  $S_z(z)$ , and  $AMF_G$  are all provided.

Mie scattering and clouds can complicate the calculation of  $w(z)$ , however tables of values for this function at various parameter values can be used with modeled vertical shape factors for local AMF calculations.

Using the vertical coordinate sigma ( $\sigma$ ), which is related to pressure ( $P$ ) by  $P = \sigma (P_S - P_T) + P_T$ , where subscripts S and T represent earth surface and top of the atmosphere respectively. The hydrostatic relation  $P = -\rho_a g z$ , with  $\rho_a$ ,  $g$ , being density of air, gravity, respectively lets us switch to the sigma coordinate using:

$$\begin{aligned} \rho_a g z &= \sigma (P_S - P_T) + P_T \\ d\sigma &= -\frac{\rho_a g}{P_S - P_T} dz \end{aligned}$$

Substitution into 3.8 gives AMF using the sigma coordinates:

$$AMF = AMF_G \int_0^1 w(\sigma) S_\sigma(\sigma) d\sigma \quad (3.9)$$

Where  $S_\sigma$  is defined as a vertical shape factor representing a normalised mixing ratio:

$$S_\sigma(\sigma) = \frac{\Omega_a}{\Omega_v} C(\sigma) \quad (3.10)$$

where  $\Omega_a$  is the vertical column of air and  $C(\sigma)$  is the mixing ratio of the absorber. This normalised shape factor is dimensionless. This can be useful when running global atmospheric models as the ground altitude is always at  $\sigma = 1$  and we need not worry about topography.

When comparing satellite observations to a chemical model, one needs to recalculate the satellite AMF using their own modelled vertical gas profiles as the a-priori shape factor in order to remove any total column bias which may be due to the satellite's apriori. Another way of removing this bias is through deconvolution (TODO: EQNS) of the averaging kernal of the satellite. The averaging kernal (AK) represents satellite sensitivities to various species at various altitudes through the atmosphere and can be approximated from the  $w(z)$  function as follows:

$$AK(z) = \frac{w(z)}{AMF} \quad (3.11)$$

Note that this is an approximation based on the OMI satellite HCHO dataset as performed in Gonzalez Abad et al., (2015).

### 3.2.9 Reference sector correction for comparison of products to various models

HCHO products from OMI and SCIAMACHY both use a median daily remote pacific ocean radiance reference spectrum, over 15°S-15°N, 140°-160°W where it is assumed that the only significant source of HCHO is methane oxidation (Desmedt2008; OMI\_README; Barkley et al., 2013). Since this oceanic background is used instead of a solar irradiance spectrum, in order to compare the output against different models, the vertical columns need to be corrected by an absolute amount. The corrected vertical column ( $\Omega_V$ ) is calculated as the slant column ( $\Omega_S$ ) minus the reference slant column ( $\Omega_{S_0}$ ) multiplied by the AMF, plus the modelled reference sector column ( $\Omega_{V_B}$ ):

$$\Omega_V = \frac{(\Omega_S - \Omega_{S_0})}{AMF} + \Omega_{V_B}$$

This method is used in various papers, including Desmedt2008; De Smedt et al., (2012), De Smedt et al., (2015), and Barkley et al., (2013).

Recently this correction was expanded (for OMI data) to include latitudinal and instrument track influence by Gonzalez Abad et al., (2015). The updated correction is explained in detail in section 3.3.8.

## 3.3 Creating a top-down isoprene inventory

### 3.3.1 Process Outline

First satellite slant columns of formaldehyde for the years 2004 - 2013 will be retrieved from NASA, BIRA, etc (TODO: list satellites + sources or reference section). This data needs to be quality assured and will undergo a basic analysis and filtering criteria as is done in several other studies, for example Marais et al., (2012), Barkley et al., (2013),

Bauwens et al., (2016), and Zhu et al., (2016) TODO: more cites. This filtering generally removes cloudy and uncertain data points, along with instrument anomalies such as the row anomaly experienced by OMI ( todo: cite row anomaly analysis/details ). A full account of the filters used when reading OMI satellite data is given in section 3.3.2.

In order to reduce uncertainty and increase the utility of the satellite data we regrid it from pointwise single time data points to 8-day averages on a latitude longitude grid which matches our model input and output grid spacing. Using the 8-day average reduces the uncertainty in each datapoint significantly, TODO: citet marais and barkley uncertainty improvements, and point to section with our estimates of the improvements over Australia.

Once the slant columns are quality filtered and gridded, additional data sources need to be used to account for anthropogenic and pyrogenic sources of HCHO. MODIS fire counts can be used in conjunction with NO<sub>2</sub> enhancements (also measured by satellite) to remove data points which may be affected by fires. TODO: If it is easier to use OMI smoke smoke aaod I'll do it that way instead of using the NO<sub>2</sub>, write here if that is the case. One possible solution to anthropogenic filtering is the national pollution index (TODO:cite:<http://www.npi.gov.au>) which contains industrial HCHO and NO<sub>X</sub> emissions from 2003 to 2014.

In order to visualise and analyse satellite column data it is generally transformed into vertical columns. Using AMF calculations as shown in section 3.2.8. Taking the biogenic slant columns, scattering weights, and apriori estimates of HCHO vertical profiles we determine vertical HCHO column amounts. This is an in depth process involving radiative transfer modelling in order to work out satellite sensitivities at various altitudes, as well as the effect from the local HCHO profile on those sensitivities. Several of these required data are available from the satellite data products, including the scattering weights and the zenith angles required to determine an AMF at any particular measured point. In this work the shape factor is recalculated from GOES-Chem, with the associated OMI per-pixel scattering weights unchanged.

Each satellite slant column measurement is corrected by some amount, based on the divergence from a modeled reference sector. The reference sector correction method corrects for several problems, however it introduces some apriori model influence. One of the problems removed through this correction method is instrument degradation, which can introduce bias over time. Another is the possible influence of varying dead/hot pixel masks across 2-D detector arrays such as OMI (De Smedt et al., 2015). This method also corrects for the errors introduced through correlations between BrO and HCHO absorption cross sections, which are especially significant at high latitudes (Gonzalez Abad et al., 2015).

The reference sector we use is defined over the pacific ocean at 140 to 160°W and 90°N to 90°S, as in Gonzalez Abad et al., (2015). HCHO concentrations are assumed to be at background levels over the pacific ocean, with their only source being CH<sub>4</sub> oxidation. A correction for each instrument pixel is created based on the difference between the background HCHO measurements from OMI and the GEOS-Chem modelled HCHO columns within the reference sector. This correction is calculated daily and applied to all good pixels based on their latitude.

When comparing satellite measurements against models it is important to recognise the impact of the apriori shape factor on the total column values. In order to remove the possible bias, the shape factor used by the satellite is often replaced using the profile from the model and then satellite total columns are recalculated (generally using equation 3.8). Without performing this step a bias between modeled and measured

total column values may be due to an apriori rather than actual chemistry or measurements. In part this is due to the sensitivity of instruments not being constant vertically through the atmosphere.

Once we have vertical columns of biogenic HCHO ( $\Omega_{HCHO}$ ) we can infer the local (grid space) isoprene emissions ( $E_{ISOP}$ ) using effective formaldehyde yield from isoprene ( $S$ ) (todo: cites with examples of this yield). This is simply expressed with the equation:

$$\Omega_{HCHO} = S \times E_{ISOP} + B \quad (3.12)$$

Where  $B$  is the background HCHO. This works as long as there is fast HCHO yield, so that the effect of chemical transport is minimal. The background HCHO is assumed to be equal to HCHO measured in the remote pacific at the same time, however transport needs to be carefully handled.

Isoprene quickly forms HCHO in the atmosphere when in the presence of high levels of  $NO_X$ . However, over Australia  $NO_X$  levels are generally not high enough and we must take extra care that we can account for the transport or 'smearing' caused by slower HCHO formation. Smearing sensitive grid boxes within the model can be detected by running the model with two uniformly differing isoprene emission levels, then finding the grid boxes where the changed HCHO column is greater than can be attributed to local emission difference. Using equation 3.12 at for two different isoprene emission levels:

$$\hat{S} = \frac{\Delta \Omega_{HCHO}}{\Delta E_{ISOP}}$$

Consider halving the isoprene emitted globally and rerunning the model, if the local grid HCHO is reduced by much more than half (factoring yield) then you can infer sensitivity to non-local isoprene emissions. This sensitivity may change with local or regional weather patterns, as greater wind speeds will reduce the time any emitted compound stays within the local grid box. As such smearing sensitivity is both spatially and temporally diverse, shown in figure TODO: is a picture of the smearing sensitivity at blahpow.

Once the smearing sensitive grid squares are filtered out, application of equation 3.12 gives us an estimate of isoprene emissions across the nation.

Most recently a Bauwens et al., (2016) undertook a similar process to what I am doing, although with slightly different focus, using the IMAGESv2 global CTM instead of GEOS-Chem. They calculate emissions which create the closest match between model and satellite vertical columns, and compare these posteriori data with the apriori (satellite data) and independent data sets. (TODO: simple outline of what they did and how my focus is different, this paper will also need to be summarised in the LitReview)

### 3.3.2 Quality filtering OMI HCHO slant columns

TODO: Quality flags and cloud cover metric uses, and discussion, along with statistics like how many datapoints are removed.

The OMI dataset has a quality flag which can be used to remove unlikely or poor satellite measurements. The states represented by this quality flag are shown in table 3.3 which is taken from Kurosu and Chance, (2014). Filtering bad or missing measurement pixels is preformed prior to any other filtering. Any pixel with a cloud fraction of greater than 40% is also removed, after the pixel is used in determining the reference sector correction, as is done in Gonzalez Abad et al., (2015) and De Smedt et al., (2015). In Martin2003 pixels with more than half of the backscattered intensity from the cloudy

sky fraction are removed, in effect removing pixels with more than 40% cloud fraction before calculating the AMF for NO<sub>2</sub> slant columns.

Value	Classification	Rational
0	Good	Column value present and passes all quality checks; data may be used with confidence.
1	Suspect	Caution advised because one or more of the following conditions are present: <ul style="list-style-type: none"> <li>• Fit convergence flag is &lt; 300 but &gt; 0: Convergence at noise level</li> <li>• Column +2<math>\sigma</math> uncertainty &lt; 0 &lt; Column +3<math>\sigma</math> uncertainty</li> <li>• Absolute column value &gt; Maximum column amount (1e19 mol/cm<sup>-2</sup>)</li> </ul>
2	Bad	Avoid using as one of the following conditions are present: <ul style="list-style-type: none"> <li>• Fit convergence flag is &lt; 0 : No convergence, abnormal termination</li> <li>• Column +3<math>\sigma</math> uncertainty &lt; 0</li> </ul>
< 0	Missing	No column values have been computed; entries are missing

TABLE 3.3: OMI quality flag values table from Kurosu and Chance, (2014)

The cloud fraction with each pixel is provided with the OMHCHO dataset, however its source is the OMI cloud product, OMCLDO2. To give an idea of how much data is filtered out, around 30% of the pixels which remain after filtering out the bad or missing data are subsequently removed due to cloudiness.

Further filtering is performed to remove the measurements which are most likely to be unrealistic: pixels with a solar zenith angle greater than 60°, and those with column density outside the range  $-0.5 \times 10^{16}$  to  $10^{17}$  molecules cm<sup>-2</sup>. These are similar filters to those applied in (TODO: read Zhu et al., (2016), add similar justification if succinct). This final filter is required due to currently unexplained large negative values which occur in the OMI HCHO product increasingly over time. Figure 3.3 shows how unfiltered HCHO columns are affected by a small set of highly negative values which heavily affect the mean column amount over any region. The histograms here show the negative (left) and positive (right) total column HCHO measurements from a subset of swaths over Australia, on the 18th of March 2013. The highly negative values can be seen around the  $-10^{19}$  molecules cm<sup>-2</sup> region.

One final selection of the data is removed prior to calculation and analysis due to instrument sensitivity issues. This removed data is based on the latitude of the satellite measurement, high northern and southern latitudes are removed as the effect of both the high solar zenith angle and (over arctic regions) the high albedo cause anomalous readings which are hard to correct. The latitudes removed from analysis for OMI satellite data are TODO: Option 1: based on the 95th( would need to choose percentile, and

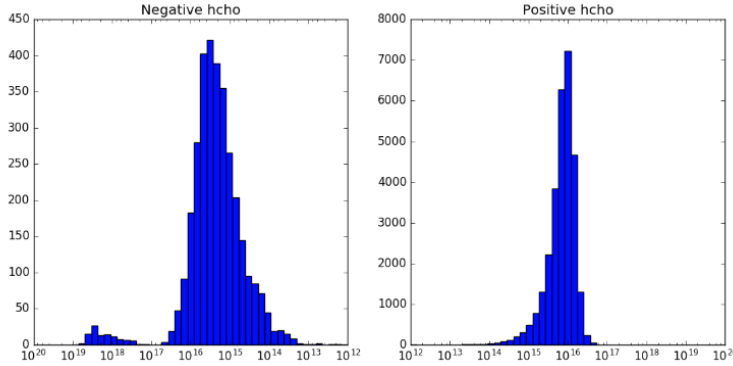


FIGURE 3.3: Column density histograms for a subset of OMI swaths over Australia on the 18th of March 2013. Negative entries are shown in the left panel, positive in the right, note the different scale between negative and positive panels.

implement moving latitude filter) percentile of ‘high’ scattering weight profiles, determined per month (or per 8 day average). Option 2: flat based on lats removed by other publications. eg remove all pixels outside of  $0^\circ \pm 60^\circ$ .

### 3.3.3 Reading OMHCHO daily slant columns

Each day the AURA satellite sweeps over the sunny side of the planet, with OMI recording roughly 90 k pixels, of which around 50 k – 80 k are classified as good. Each pixel contains several important pieces of data which are needed for recalculation of the HCHO vertical column: the total column of HCHO (molecules  $\text{cm}^{-2}$ ), cloud fraction, associated shape factor, AMF, geometric AMF, scattering weight, vertical altitudes (hPa) used with scattering weights, viewing zenith angle, solar zenith angle, latitude, longitude, OMI sensor track, main data quality flag, cross track flag, and total column uncertainty. All of these data are needed in order to reconstruct the total vertical column using a modelled apriori shape factor rather than NASA’s included apriori shape factor. Each pixel and its relevant data are saved in a long list, around 1.1 million pixels per day. As well as the data directly read from the OMI swath files, further information is added to each pixel. This is the new AMF calculated through replacing the apriori vertical profile with the newer GEOS-Chem simulated profile, which is described in section 3.3.7. The shape factors and scattering weights for each pixel lie along a z-axis which is vertically resolved to 47 layers and is shown in figure TODO: make figure showing this stuff and an example profile.

TODO: Show an example of OMI swaths.

### 3.3.4 Regridding to 0.25 by 0.3125 8-day averaged vertical columns

TODO: how this is done, and how we measure uncertainty, and how much uncertainty improved by this.

Regridded OMI HCHO columns from the are based on 14-15 daily swaths of measurements provided by NASA. Each swath contains roughly  $9 \times 10^4$  pixels, each of which contains various data including latitude, longitude vertical column HCHO, etc. In order to regrid these columns each pixel is mapped into a global grid of  $0.25^\circ \times 0.3125^\circ$  latitude by longitude (matching GEOS-5 native resolution) which may contain up to 15

entries from a particular day's orbits. Total vertical column amounts (both the satellite original and the columns reprocessed as follows) are averaged over each 8 days starting on January 1st 2005.

TODO: Discuss saving the list of daily entries into a gridded space.

TODO: time per regridding and reprocessing: This mapping requires some processing time as well as RAM and computer storage space, and has been performed on the National Computing Infrastructure (NCI) supercomputer cluster. In order to reprocess one year of swath files, X GB of daily data was downloaded and then transformed into Y GB of 8-day averaged gridded data. This takes around X minutes per day, and is very parallelisable as each 8 day block is completely independent. Using  $N \times 8$  concurrent processors on NCI's computer cluster running Python allows for very fast reprocessing of our entire timeline. As much as possible, processing is done using the HDF-EOS5 format, with GEOS-Chem output being read and processed from bitpunch to HDF-EOS5 prior to reprocessing. The scripts to regrid and reprocess the swath data set are available in the supplementary (TODO).

### 3.3.5 Filtering pyrogenic HCHO

TODO: How modis fire counts are used as well as statistics on removed data points.

On board NASA's AQUA satellite, the MODIS instrument is used to detect fire activity. The product used here is called MYD14C8H ((Giglio, Csiszar, and Justice, 2006)), which looks at fire activity over eight days on a  $0.5^\circ$  square grid globally. Regridding the product to the native meteorological grid of GEOS5 at  $0.25^\circ$  latitude by  $0.3125^\circ$  longitude is done in python with an interpolator which maps the values of the new grid rectangles to the value of the nearest grid square. An example of the change in resolution is provided in figure 3.4, where the grids are shown over a basic map of Tasmania. The direct affect of this interpolation is shown as an example in figure 3.5, which is showing the regridded MODIS fire count over Australia from January 2005 (avg of first 8 days) in two subplots.

Figure 3.6 shows an example of the total column HCHO calculated using GEOS-Chem aprioris ( $\Omega_{GEOS}$ ) before and after using the MYD14C8H product to exclude fire influenced pixels. (TODO: show time series of how many pixels are removed and discuss if this causes any issues down the line)

### 3.3.6 Filtering anthropogenic HCHO

TODO

### 3.3.7 Recalculating the AMF to create our own vertical HCHO columns

OMI's apriori shape factor is based on the GEOS-Chem model, which uses 47 layers between the earth's surface and the top of the atmosphere using a pressure-eta hybrid (the actual values are shown in table ??). Taking a more recent GEOS-Chem apriori shape factor and integrating along the vertical axis using equation 3.8 gives us a new AMF ( $AMF_n$ ). This is done in Python using simple rectangular integration. All that remains for recalculating the total vertical column using our new apriori shape factor is to apply the new AMF and remove the old:

$$\Omega_{new} = \Omega \frac{AMF}{AMF_n}$$

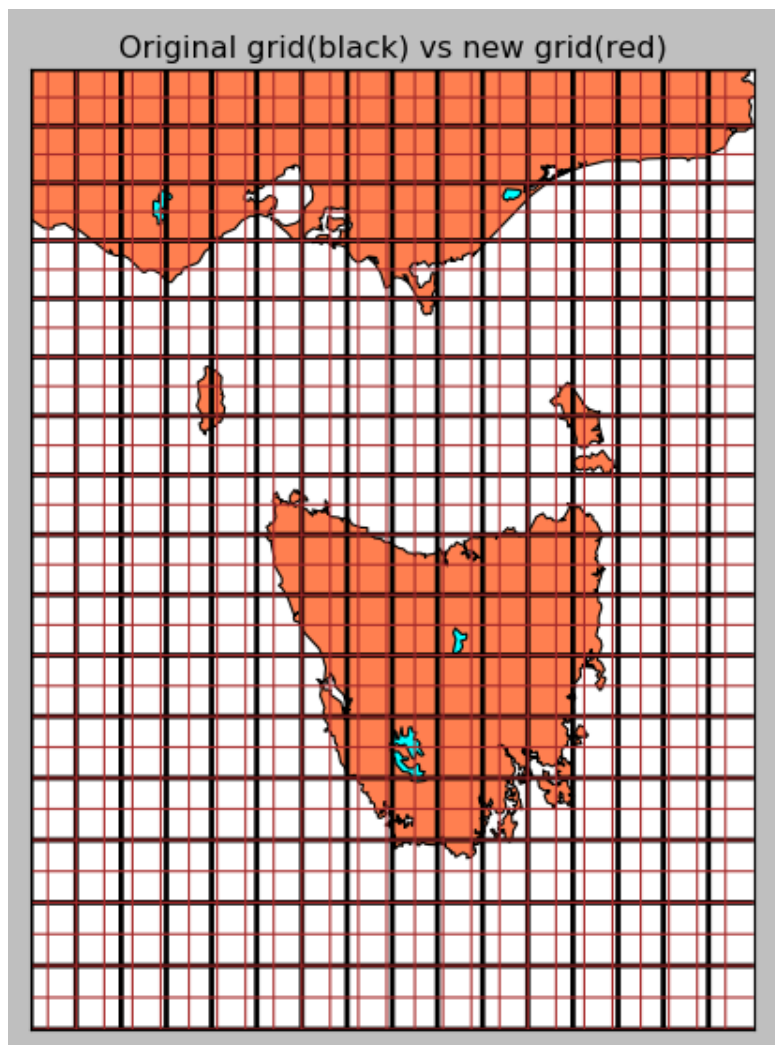


FIGURE 3.4: Example of grid space change using  $0.5 \times 0.5$  and  $0.25 \times 0.3125$  latitude by longitude resolution.

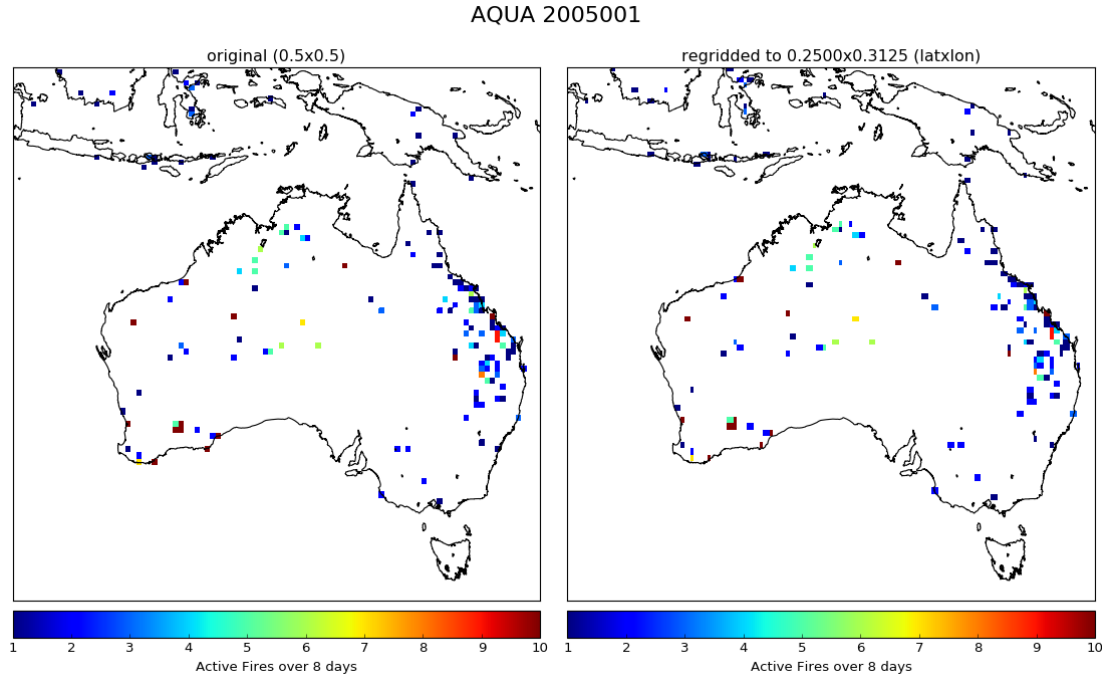


FIGURE 3.5: Example of MODIS 8 day grid interpolation from  $0.5 \times 0.5$  to  $0.25 \times 0.3125$  latitude by longitude resolution. This example uses MODIS fire counts for 1-8 January 2005.

The vertical column scattering weights and apriori shape factors provided in the OMHCHO dataset are defined on 47 levels. In order to reformulate the vertical column using updated GEOS-Chem hcho apriori shape factors I have run GEOS-Chem version 10.01 on the full 72 level vertical grid at 2 by 2.5 (lat by lon) degree monthly resolution. These monthly vertical profiles are then used to provide the apriori shape factor for the higher horizontally resolved satellite columns, which pick the nearest apriori from the model. The new apriori profiles are monthly averages, which is the same temporal resolution used by the OMI apriori shape factors.

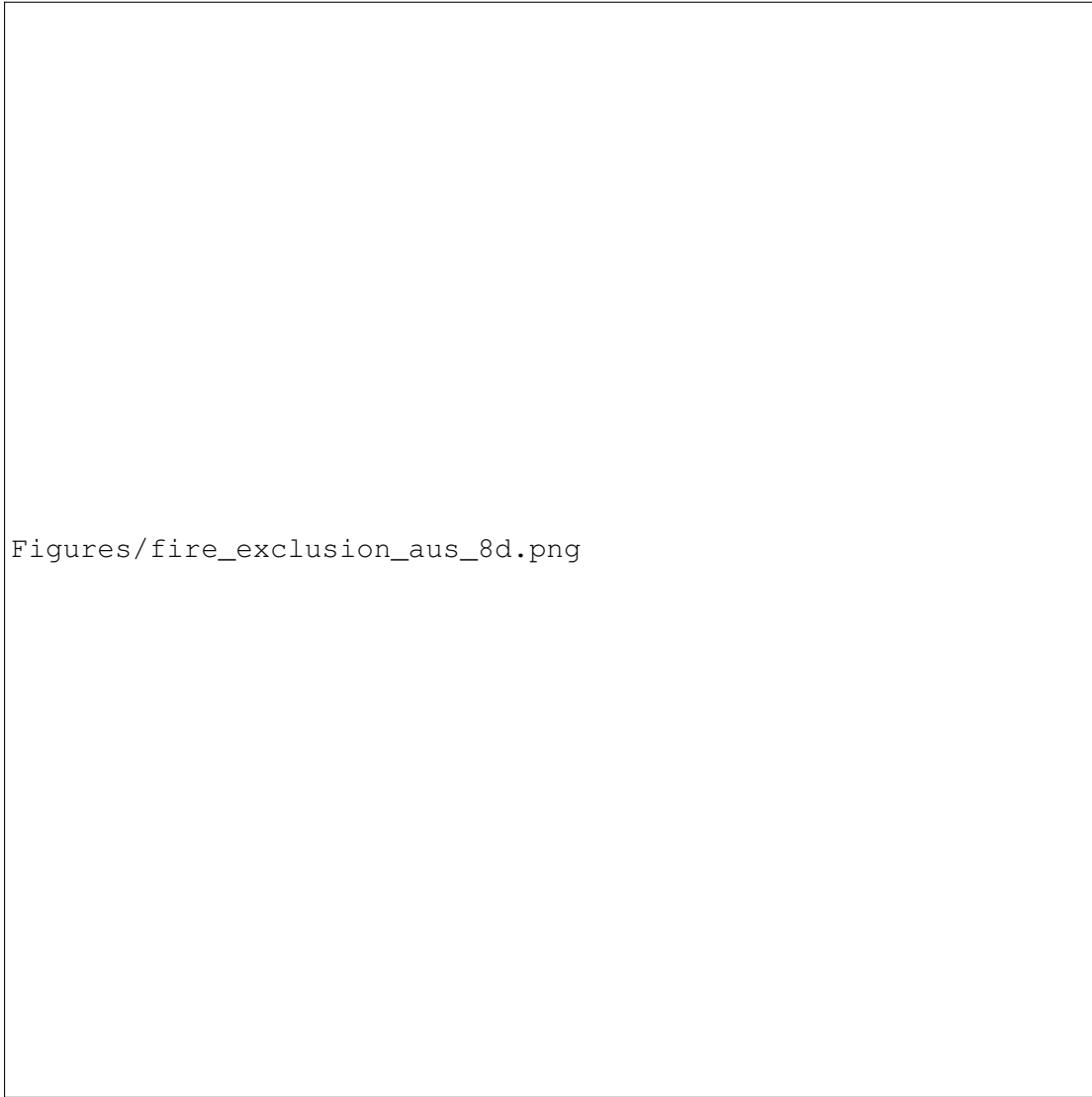
A new AMF is determined using equation 3.8) with the apriori shape factor set by our GEOS-Chem model run. In order to reformulate the AMF, the 72 level profile from my GEOS-Chem UCX run is transformed from ppb to a normalized number density profile in order to match equation 3.7. This conversion uses the following equation:

$$\eta_{HCHO} = ppb_{HCHO} \times \eta_a \times 10^{-9} \quad (3.13)$$

where  $\eta_{HCHO}$  is the number density of a HCHO, and  $ppb_{HCHO}$  is the molecules of that species per billion molecules of air. In order to normalize these vertical density profiles over the globe, we divide by the modelled total vertical column  $\Omega_{HCHO}$  which is determined by:

$$\Omega_{HCHO} = 2.12 \times 10^{13} \sum_z (ppb_{HCHO}(z)(P(z) - P(z + 1)))$$

where  $P(z)$  is the pressure (hPa) at the bottom of altitude level  $z$ , the constant  $2.12e13$  is determined from equation (TODO: run through this number in another section?). In effect this equation sums over the molecules per  $\text{cm}^2$  in each altitude level.



Figures/fire\_exclusion\_aus\_8d.png

FIGURE 3.6: Vertical column HCHO calculated using OMI satellite swaths with GEOS-Chem aprioris, averaged over 1-8 January 2005 with and without fire affected squares removed.

We have  $S_z(z)$  and  $\omega(z)$  over the vertical pressure coordinate  $z$  at all latitude and longitude points on whatever grid we wish. We convert to sigma ( $\sigma$ ) vertical coordinate using  $P = \sigma(P_S - P_T) + P_T$ , where  $P_T$  is the pressure at the top of the atmosphere and  $P_S$  is surface pressure. In the sigma coordinate system we calculate a different shape factor:

$$S_\sigma(\sigma) = \frac{\Omega_a}{\Omega_v} C_{HCHO}(\sigma) \quad (3.14)$$

where  $\Omega_a$  is the vertical column of air from the surface to the top of the atmosphere and  $C_{HCHO}(\sigma)$  is the mixing ratio of HCHO. This equation comes from Palmer et al., (2001), and is unitless since  $\Omega_a/\Omega_v$  is molecules of air per molecule of HCHO; the opposite of  $C_{HCHO}$ .

TODO: currently I'm assuming the surface pressure from omi measurements is just the bottom pressure level they provide. If I change this to use an inverted geometric midpoint calculation then I need to explain it, otherwise I will need to note the assumption  $\sqrt{(P_1 \times P_{surf})} = P_0$  becomes  $P_{surf} = \frac{P_0^2}{P_1}$  where currently I'm using  $P_0$  as the surface.

$S_\sigma(\sigma)$  is determined after running GEOS-Chem, which outputs vertical profiles of air density and HCHO mixing ratio, at 72 vertical levels with associated metadata such as vertical layer height and pressure, grid box location, height, and surface pressure. Using these outputs the vertical columns ( $\Omega_a, \Omega_v$ ) are calculated for each horizontal grid point ( $i, j$ ) as follows:

$$\begin{aligned} \Omega_a(i, j) &= \Sigma_z (N_a(i, j, z) \times H(i, j, z)) \\ \Omega_z(i, j) &= \Sigma_z (N_{HCHO}(i, j, z) \times H(i, j, z)) \end{aligned}$$

where  $N_a$ , and  $N_{HCHO}$  are the densities of air and HCHO,  $H$  is the layer height (for each grid box). Note that HCHO density is determined from the outputted mixing ratio:  $N_{HCHO} = C_{HCHO} \times N_a$ .

Once  $S_\sigma(\sigma)$  is determined it is then stored in HDF-EOS5 format, to be used in conjunction with the satellite measurements to calculate an AMF as shown in equation 3.8. As the GEOS-Chem V10.01 output is in bitpunch format, the code to read the data and create the shape factor is written in IDL, which has many procedures and functions which are already written to handle reading this format. The code is provided in supplementary TODO: put code into supplement section.

For each OMI slant column, a new AMF is calculated using  $S_\sigma(\sigma)$  and the provided scattering weights  $\omega(\sigma)$  using equation 3.8. This integral is applied in python by taking the sum of  $S_\sigma(\sigma) \times \omega(\sigma) \times d\sigma$  for each  $\sigma$  determined at 72 levels in GEOS-Chem, with the provided  $\omega$  interpolated linearly to these same levels. An example of these interpolations is shown in figure TODO: interpolation figure with symbols at original points and interpolated line overplotted for both functions over hPa. Globally this reprocessing changed the AMF by TODO: global total percent difference in AMF. In total this caused TODO: total column HCHO change globally/yearly In Summer over Australia the global AMF difference was TODO: Difference summers only. This changed Australia's HCHO amounts from TODO: X to Y Tg per year plus minus one std.

### 3.3.8 Determining and applying the pacific ocean reference sector normalisation

As is done in Gonzalez Abad et al., (2015), a reference sector defined over the Pacific ocean is used to handle OMI instrument errors. This correction is calculated

based on good satellite measurements over the pacific ocean reference sector; between 140°W and 160°W, covering every latitude. Corrections are made using apriori HCHO columns in the same reference sector modelled using GEOS-Chem. The apriori reference sector of HCHO vertical columns (VCs) is created by GEOS-Chem using 15 minute time resolution, with 2 by 2.5° latitude by longitude resolution. These simulated values use the GEOS-Chem output averaged between 1300 and 1400 local time at each grid box, in order to match the overpass time of OMI. The longitudinal average is taken within the apriori reference sector, as corrections are assumed to be longitudinally invariant. The modeled reference sector is interpolated to arbitrary latitude in order to be used in OMI measurement correction array creation. Figure TODO shows the simulated reference sector VCs as an example, calculated on January 1st 2005. In this figure the vertical resolution is increased from 2° to 0.36°, through linear interpolation, in order to form 500 vertical bins which are used in correcting the satellite data.

Each day, good satellite measurements taken over the reference sector are used to determine a correction array. The correction is based on the difference between measured slant column and the modeled slant column within the reference sector. The model does not produce slant columns associated with each measurement, however one is created by multiplying the VC with the associated slant column's AMF.

For OMI swaths, each row of measured data contains 60 'Across track'(track) measurements. The track index (*i*) relates a the measurement to one of the 60 left to right columns of data. Corrections for each measurement are calculated by taking the difference between the measured slant column and the apriori slant column as follows:

$$\text{Correction}(i, j) = SC_{HCHO}(i, j) - VC_{GEOS-Chem}(\text{lat}(j)) \times AMF_{OMI}(i, j) \quad (3.15)$$

where *j* represents a latitude index and  $VC_{GEOS-Chem}(\text{lat})$  represents the apriori reference sector vertical column HCHO at the latitude corresponding to *j*. Note that the correction is in molecules per cm<sup>2</sup>.

This correction is independently calculated for each of the 60 tracks, at each latitude where a good satellite measurement exists which used that track. TODO: median binned RSC method  $\text{Correction}(i, \text{lat}(j))$  is determined by sorting the corrections for each track based into 500 latitude bins.

Due incomplete latitudinal coverage, the correction for each track is interpolated linearly between measurements, with corrections outside of the highest measured latitudes being equal to the corrections at the highest measured latitudes. Figure 3.7 shows an example of the 60 track corrections for January 1st 2005, the points are satellite measurements and the lines are the interpolations for each track.

One correction is associated with every good satellite measurement which is used to create a reference sector corrected measurement (Vertical Column Corrected or VCC) through the following equation:

$$VCC(i, j) = \frac{SC_{HCHO}(i, j) - \text{Correction}(i, \text{lat}(j))}{AMF(i, j)} \quad (3.16)$$

Finally, for each day, the good satellite measurements are averaged into our own latitude longitude resolution bins along with the associated corrected SC, VC, VCC, AMF, and bin entry count. The bin entry count is used to create an 8-day average out of the one day averages, as it is the daily mean multiplied by the daily count summed over 8 days divided by the total count for each bin.

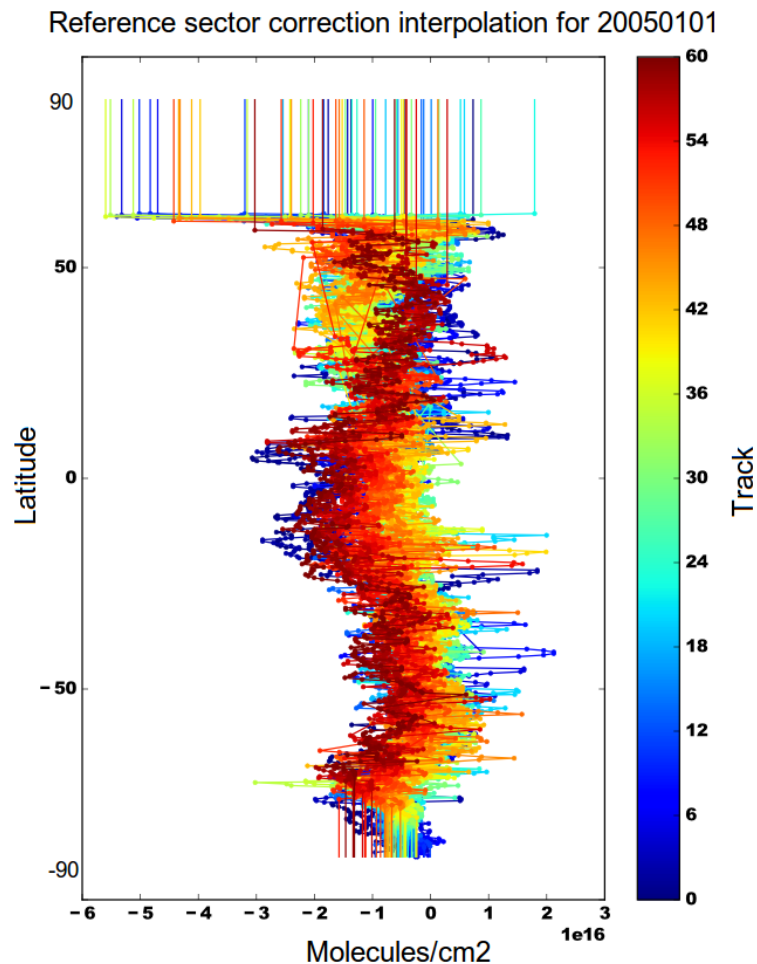


FIGURE 3.7: Example of track correction interpolations for January 1st 2005, points represent satellite slant column measurements, with lines interpolating and extrapolating along the latitudinal direction.

### **3.3.9 Determining S, the isoprene emissions**

TODOs los zapatos

### **3.3.10 Extrapolating the circadian cycle**

Isoprene emissions occur with regular daily cycles caused by things like local temperature, sunlight, drought, and other environmental factors (TODO: find/cite eucalypt isoprene paper, daily cycle plot if can find).

(TODO: following stuff, add some basic plots and error analysis eventually also) Using a model of the daily isoprene emissions fit to the offset determined by satellite HCHO based estimates, we produce a high temporal resolution isoprene emissions inventory. During days with more than one HCHO column measurement we can more confidently fit the cycle. For example EOS AURA's OMI measurements from 2004 can be combined with MetOp-A's GOME2 after October 2006, with daily overpasses by OMI and GOME2 at 1345 and 0930 respectively. This allows a better retrieval of the daily amplitude of isoprene emissions.

### **3.3.11 Comparison with MEGAN**

TODO: Direct comparison here, maps of differences for some metrics(monthly average,?). comparison of model run results using different inventory shown in section (reference here)

### **3.3.12 Comparison with in-situ measurements**

## **3.4 Model comparison with and without satellite HCHO based inventory**

# Bibliography

- Guenther, Alex et al. (1995). "A global model of natural volatile organic compound emissions". In: *Journal of Geophysical Research* 100.D5, pp. 8873–8892. ISSN: 0148-0227. DOI: [10.1029/94JD02950](https://doi.org/10.1029/94JD02950). URL: <http://onlinelibrary.wiley.com/doi/10.1029/94JD02950/full>.
- Glasius, Marianne and Allen H. Goldstein (2016). "Recent Discoveries and Future Challenges in Atmospheric Organic Chemistry". In: *Environmental Science and Technology* 50.6, pp. 2754–2764. ISSN: 15205851. DOI: [10.1021/acs.est.5b05105](https://doi.org/10.1021/acs.est.5b05105).
- Yue, X., N. Unger, and Y. Zheng (2015). "Distinguishing the drivers of trends in land carbon fluxes and plant volatile emissions over the past 3 decades". In: *Atmospheric Chemistry and Physics* 15.20, pp. 11931–11948. ISSN: 16807324. DOI: [10.5194/acp-15-11931-2015](https://doi.org/10.5194/acp-15-11931-2015).
- Hsieh, Nan-Hung and Chung-Min Liao (2013). "Fluctuations in air pollution give risk warning signals of asthma hospitalization". In: *Atmospheric Environment* 75, pp. 206–216. DOI: [10.1016/j.atmosenv.2013.04.043](https://doi.org/10.1016/j.atmosenv.2013.04.043). URL: <http://dx.doi.org/10.1016/j.atmosenv.2013.04.043>.
- Avnery, Shiri et al. (2013). "Global crop yield reductions due to surface ozone exposure: 2. Year 2030 potential crop production losses and economic damage under two scenarios of O<sub>3</sub> pollution". In: *Atmospheric Environment* 71.13, pp. 408–409. ISSN: 13522310. DOI: [10.1016/j.atmosenv.2012.12.045](https://doi.org/10.1016/j.atmosenv.2012.12.045). URL: <http://dx.doi.org/10.1016/j.atmosenv.2011.01.002>.
- Myhre, G and D Shindell (2013). *Chapter 8: Anthropogenic and Natural Radiative Forcing, in Climate Change 2013: The Physical Science Basis, Working Group 1 Contribution to the Fifth Assessment Report of the Intergovernmental Panel on Climate Change*, 2013. Fifth Assessment Report of the Intergovernmental Panel on Climate Change, 2013.
- Hoek, Gerard et al. (2013). "Long-term air pollution exposure and cardio-respiratory mortality: a review". In: *Environmental Health* 12.1, p. 43. DOI: [10.1186/1476-069x-12-43](https://doi.org/10.1186/1476-069x-12-43). URL: <http://dx.doi.org/10.1186/1476-069x-12-43>.
- Krewski, D et al. (2009). "Extended follow-up and spatial analysis of the American Cancer Society study linking particulate air pollution and mortality". In: *Res Rep Health Eff Inst* 140, pp. 5–36. ISSN: 1041-5505 (Print) 1041-5505 (Linking). URL: <http://www.ncbi.nlm.nih.gov/pubmed/19627030>.
- Silva, Raquel A et al. (2013). "Global premature mortality due to anthropogenic outdoor air pollution and the contribution of past climate change". In: *Environ. Res. Lett.* 8.3, p. 34005. DOI: [10.1088/1748-9326/8/3/034005](https://doi.org/10.1088/1748-9326/8/3/034005). URL: <http://dx.doi.org/10.1088/1748-9326/8/3/034005>.
- Lelieveld, J et al. (2015). "The contribution of outdoor air pollution sources to premature mortality on a global scale". In: *Nature* 525.7569, pp. 367–371. DOI: [10.1038/nature15371](https://doi.org/10.1038/nature15371). URL: <http://dx.doi.org/10.1038/nature15371>.
- VanDerA, R J et al. (2008). "Trends seasonal variability and dominant NO x source derived from a ten year record of NO<sub>2</sub> measured from space". In: *J. Geophys. Res.* 113.D4. DOI: [10.1029/2007jd009021](https://doi.org/10.1029/2007jd009021). URL: <http://dx.doi.org/10.1029/2007jd009021>.

- Guenther, A et al. (2006). "Estimates of global terrestrial isoprene emissions using MEGAN (Model of Emissions of Gases and Aerosols from Nature)". In: *Atmospheric Chemistry and Physics* 6.11, pp. 3181–3210. DOI: [10.5194/acp-6-3181-2006](https://doi.org/10.5194/acp-6-3181-2006). URL: <http://dx.doi.org/10.5194/acp-6-3181-2006>.
- Monks, P. S. et al. (2015). "Tropospheric ozone and its precursors from the urban to the global scale from air quality to short-lived climate forcer". In: *Atmospheric Chemistry and Physics* 15.15, pp. 8889–8973. ISSN: 1680-7324. DOI: [10.5194/acp-15-8889-2015](https://doi.org/10.5194/acp-15-8889-2015). URL: <http://www.atmos-chem-phys.net/15/8889/2015/>.
- Marais, E A et al. (2012). "Isoprene emissions in Africa inferred from OMI observations of formaldehyde columns". In: *Atmospheric Chemistry and Physics Discussions* 12.3, pp. 7475–7520. DOI: [10.5194/acpd-12-7475-2012](https://doi.org/10.5194/acpd-12-7475-2012). URL: <http://dx.doi.org/10.5194/acpd-12-7475-2012>.
- Bauwens, M et al. (2013). "Satellite-based isoprene emission estimates (2007–2012) from the GlobEmission project". In: *Proceedings of the ACCENT-Plus Symposium, Atmospheric Composition Change-Policy Support and Science, Urbino*, pp. 17–20.
- Kefauver, Shawn C., Iolanda Filella, and Josep Peñuelas (2014). "Remote sensing of atmospheric biogenic volatile organic compounds (BVOCs) via satellite-based formaldehyde vertical column assessments". In: *International Journal of Remote Sensing*. URL: <http://www.tandfonline.com/doi/abs/10.1080/01431161.2014.968690#.VkjEubNM61M>.
- Hewitt, C N et al. (2011). "Ground-level ozone influenced by circadian control of isoprene emissions". In: *Nature Geoscience* 4.10, pp. 671–674. DOI: [10.1038/ngeo1271](https://doi.org/10.1038/ngeo1271). URL: <http://dx.doi.org/10.1038/ngeo1271>.
- Fan, Jiwen and Renyi Zhang (2004). "Atmospheric oxidation mechanism of isoprene". In: *Environmental Chemistry* 1.3, pp. 140–149. ISSN: 14482517. DOI: [10.1071/EN04045](https://doi.org/10.1071/EN04045). URL: <http://dx.doi.org/10.1071/en04045>.
- Stavrakou, T et al. (2009). "Evaluating the performance of pyrogenic and biogenic emission inventories against one decade of space-based formaldehyde columns". In: *Atmospheric Chemistry and Physics* 9.3, pp. 1037–1060. DOI: [10.5194/acp-9-1037-2009](https://doi.org/10.5194/acp-9-1037-2009). URL: <http://dx.doi.org/10.5194/acp-9-1037-2009>.
- Niinemets, ?? Et al. (2010). "The emission factor of volatile isoprenoids: Stress, acclimation, and developmental responses". In: *Biogeosciences* 7.7, pp. 2203–2223. ISSN: 17264170. DOI: [10.5194/bg-7-2203-2010](https://doi.org/10.5194/bg-7-2203-2010).
- Abbot, Dorian S. (2003). "Seasonal and interannual variability of North American isoprene emissions as determined by formaldehyde column measurements from space". In: *Geophysical Research Letters* 30.17, pp. 1999–2002. ISSN: 0094-8276. DOI: [10.1029/2003GL017336](https://doi.org/10.1029/2003GL017336). URL: <http://doi.wiley.com/10.1029/2003GL017336>.
- Millet, Dylan B et al. (2006). "Formaldehyde distribution over North America: Implications for satellite retrievals of formaldehyde columns and isoprene emission". In: *J. Geophys. Res.* 111.D24. DOI: [10.1029/2005jd006853](https://doi.org/10.1029/2005jd006853). URL: <http://dx.doi.org/10.1029/2005jd006853>.
- Marais, E A et al. (2014). "Improved model of isoprene emissions in Africa using Ozone Monitoring Instrument (OMI) satellite observations of formaldehyde: implications for oxidants and particulate matter". In: *Atmospheric Chemistry and Physics* 14.15, pp. 7693–7703. DOI: [10.5194/acp-14-7693-2014](https://doi.org/10.5194/acp-14-7693-2014). URL: <http://dx.doi.org/10.5194/acp-14-7693-2014>.
- Barkley, Michael P. et al. (2013). "Top-down isoprene emissions over tropical South America inferred from SCIAMACHY and OMI formaldehyde columns". In: *Journal of Geophysical Research Atmospheres* 118.12, pp. 6849–6868. ISSN: 21698996. DOI: [10.1002/jgrd.50552](https://doi.org/10.1002/jgrd.50552). URL: <http://dx.doi.org/10.1002/jgrd.50552>.

- Palmer, Paul I (2003). "Mapping isoprene emissions over North America using formaldehyde column observations from space". In: *J. Geophys. Res.* 108.D6. DOI: [10.1029/2002jd002153](https://doi.org/10.1029/2002jd002153). URL: <http://dx.doi.org/10.1029/2002jd002153>.
- Li, Fuyu, Paul Ginoux, and V Ramaswamy (2008). "Distribution transport, and deposition of mineral dust in the Southern Ocean and Antarctica: Contribution of major sources". In: *J. Geophys. Res.* 113.D10. DOI: [10.1029/2007jd009190](https://doi.org/10.1029/2007jd009190). URL: <http://dx.doi.org/10.1029/2007jd009190>.
- Duncan Fairlie, T., Daniel J. Jacob, and Rokjin J. Park (2007). "The impact of transpacific transport of mineral dust in the United States". In: *Atmospheric Environment* 41.6, pp. 1251–1266. ISSN: 13522310. DOI: [10.1016/j.atmosenv.2006.09.048](https://doi.org/10.1016/j.atmosenv.2006.09.048). URL: <http://dx.doi.org/10.1016/j.atmosenv.2006.09.048>.
- Ridley, D A et al. (2013). "Toward resolution-independent dust emissions in global models: Impacts on the seasonal and spatial distribution of dust". In: *Geophys. Res. Lett.* 40.11, pp. 2873–2877. DOI: [10.1002/grl.50409](https://doi.org/10.1002/grl.50409). URL: <http://dx.doi.org/10.1002/grl.50409>.
- Shao, Yaping et al. (2007). "Numerical simulation of the October 2002 dust event in Australia". In: *J. Geophys. Res.* 112.D8. DOI: [10.1029/2006jd007767](https://doi.org/10.1029/2006jd007767). URL: <http://dx.doi.org/10.1029/2006jd007767>.
- Rotstayn, L D et al. (2011). "Simulated enhancement of ENSO-related rainfall variability due to Australian dust". In: *Atmos. Chem. Phys. Discuss.* 11.1, pp. 1595–1639. DOI: [10.5194/acpd-11-1595-2011](https://doi.org/10.5194/acpd-11-1595-2011). URL: <http://dx.doi.org/10.5194/acpd-11-1595-2011>.
- Zender, Charles S (2003). "Mineral Dust Entrainment and Deposition (DEAD) model: Description and 1990s dust climatology". In: *J. Geophys. Res.* 108.D14. DOI: [10.1029/2002jd002775](https://doi.org/10.1029/2002jd002775). URL: <http://dx.doi.org/10.1029/2002jd002775>.
- Grand, Maxime M. et al. (2015). "Dust deposition in the eastern Indian Ocean: The ocean perspective from Antarctica to the Bay of Bengal". In: *Global Biogeochemical Cycles* 29.3, pp. 357–374. ISSN: 19449224. DOI: [10.1002/2014gb004898](https://doi.org/10.1002/2014gb004898). URL: <http://dx.doi.org/10.1002/2014gb004898>.
- Rijkenberg, Micha J A et al. (2014). "The Distribution of Dissolved Iron in the West Atlantic Ocean". In: *PLoS ONE* 9.6. Ed. by Fanis Missirlis, e101323. DOI: [10.1371/journal.pone.0101323](https://doi.org/10.1371/journal.pone.0101323). URL: <http://dx.doi.org/10.1371/journal.pone.0101323>.
- Myriokefalitakis, S et al. (2015). "Changes in dissolved iron deposition to the oceans driven by human activity: a 3-D global modelling study". In: *Biogeosciences Discussions* 12.5, pp. 3943–3990. DOI: [10.5194/bgd-12-3943-2015](https://doi.org/10.5194/bgd-12-3943-2015). URL: <http://dx.doi.org/10.5194/bgd-12-3943-2015>.
- Jacob, Daniel J (1999). *Introduction to Atmospheric Chemistry*. Ed. by Daniel J Jacob. Princeton University Press. URL: <http://acmg.seas.harvard.edu/people/faculty/djj/book/index.html>.
- EUMETSAT (2015). GOME2. URL: <http://www.eumetsat.int/website/home/Satellites/CurrentSatellites/Metop/MetopDesign/GOME2/index.html>.
- Leue, C et al. (2001). "Quantitative analysis of NO x emissions from Global Ozone Monitoring Experiment satellite image sequences". In: *J. Geophys. Res.* 106.D6, p. 5493. DOI: [10.1029/2000jd900572](https://doi.org/10.1029/2000jd900572). URL: <http://dx.doi.org/10.1029/2000jd900572>.
- Eskes, H J and K F Boersma (2003). "Averaging kernels for DOAS total-column satellite retrievals". In: *Atmospheric Chemistry and Physics* 3.1, pp. 1285–1291. ISSN: 1680-7324.

- DOI: [10.5194/acpd-3-1285-2003](https://doi.org/10.5194/acpd-3-1285-2003). URL: <http://dx.doi.org/10.5194/acpd-3-1285-2003>.
- Forster, Piers M. et al. (2007). "Effects of ozone cooling in the tropical lower stratosphere and upper troposphere". In: *Geophysical Research Letters* 34.23, pp. 1–5. ISSN: 00948276. DOI: [10.1029/2007GL031994](https://doi.org/10.1029/2007GL031994).
- Stevenson, D S et al. (2006). "Multimodel ensemble simulations of present-day and near-future tropospheric ozone". In: *J. Geophys. Res.* 111.D8. DOI: [10.1029/2005JD006338](https://doi.org/10.1029/2005JD006338). URL: <http://dx.doi.org/10.1029/2005JD006338>.
- Jerrett, Michael et al. (2009). "Long-Term Ozone Exposure and Mortality". In: *New England Journal of Medicine* 360.11, pp. 1085–1095. DOI: [10.1056/nejmoa0803894](https://doi.org/10.1056/nejmoa0803894). URL: <http://dx.doi.org/10.1056/nejmoa0803894>.
- Environment, Former Standing Council on and Water (incorporating the National Environment Protection Council) (2015). NEPC Annual Reports. URL: <http://www.scew.gov.au/publications/nepc-annual-reports>.
- Delmas, R, D Serca, and C Jambert (1997). "Global inventory of NOx sources". In: *Nutrient cycling in agroecosystems* 48.x, pp. 51–60. ISSN: 1385-1314. DOI: [10.1023/A:1009793806086](https://doi.org/10.1023/A:1009793806086). URL: <http://link.springer.com/article/10.1023/A:1009793806086>.
- Miyazaki, K, H J Eskes, and K Sudo (2011). "Global NOx emission estimates derived from an assimilation of OMI tropospheric NO2 columns". In: *Atmospheric Chemistry and Physics Discussions* 11.12, pp. 31523–31583. DOI: [10.5194/acpd-11-31523-2011](https://doi.org/10.5194/acpd-11-31523-2011). URL: <http://dx.doi.org/10.5194/acpd-11-31523-2011>.
- Sillman, Sanford (2002). "Some theoretical results concerning O<sub>3</sub>-NO<sub>x</sub>-VOC chemistry and NO<sub>x</sub>-VOC indicators". In: *J. Geophys. Res.* 107.D22. DOI: [10.1029/2001jd001123](https://doi.org/10.1029/2001jd001123). URL: <http://dx.doi.org/10.1029/2001jd001123>.
- Mahajan, Anoop S et al. (2015). "Inter-annual variations in satellite observations of nitrogen dioxide and formaldehyde over India". In: *Atmospheric Environment* 116, pp. 194–201. DOI: [10.1016/j.atmosenv.2015.06.004](https://doi.org/10.1016/j.atmosenv.2015.06.004). URL: <http://dx.doi.org/10.1016/j.atmosenv.2015.06.004>.
- Sprenger, Michael, Mischa Croci Maspoch, and Heini Wernli (2003). "Tropopause folds and cross-tropopause exchange: A global investigation based upon ECMWF analyses for the time period March 2000 to February 2001". In: *Journal of Geophysical Research: Atmospheres* 108.D12, n/a-n/a. ISSN: 2156-2202. DOI: [10.1029/2002JD002587](https://doi.org/10.1029/2002JD002587). URL: <http://dx.doi.org/10.1029/2002JD002587>.
- Mihalikova, M et al. (2012). "Observation of a tropopause fold by MARA VHF wind-profiler radar and ozonesonde at Wasa, Antarctica: comparison with ECMWF analysis and a WRF model simulation". In: *Annales Geophysicae* 30.9, pp. 1411–1421. DOI: [10.5194/angeo-30-1411-2012](https://doi.org/10.5194/angeo-30-1411-2012). URL: <http://www.ann-geophys.net/30/1411/2012/>.
- Zanis, P et al. (2003). "Forecast, observation and modelling of a deep stratospheric intrusion event over Europe". In: *Atmospheric Chemistry and Physics* 3.3, pp. 763–777. DOI: [10.5194/acp-3-763-2003](https://doi.org/10.5194/acp-3-763-2003). URL: <http://www.atmos-chem-phys.net/3/763/2003/>.
- Langford, A O et al. (2009). "Stratospheric contribution to high surface ozone in Colorado during springtime". In: *Geophys. Res. Lett.* 36.12. DOI: [10.1029/2009gl038367](https://doi.org/10.1029/2009gl038367). URL: <http://dx.doi.org/10.1029/2009gl038367>.
- Terao, Yukio et al. (2008). "Contribution of stratospheric ozone to the interannual variability of tropospheric ozone in the northern extratropics". In: *J. Geophys. Res.* 113.D18. DOI: [10.1029/2008jd009854](https://doi.org/10.1029/2008jd009854). URL: <http://dx.doi.org/10.1029/2008jd009854>.

- Tang, Q. and M. J. Prather (2010). "Correlating tropospheric column ozone with tropopause folds: The Aura-OMI satellite data". In: *Atmospheric Chemistry and Physics* 10.19, pp. 9681–9688. ISSN: 16807316. DOI: [10.5194/acp-10-9681-2010](https://doi.org/10.5194/acp-10-9681-2010).
- Zhang, L et al. (2014). "Sources contributing to background surface ozone in the US Intermountain West". In: *Atmos. Chem. Phys.* 14.11, pp. 5295–5309. DOI: [10.5194/acp-14-5295-2014](https://doi.org/10.5194/acp-14-5295-2014). URL: <http://dx.doi.org/10.5194/acp-14-5295-2014>.
- Hegglin, Michaela I and Theodore G Shepherd (2009). "Large climate-induced changes in ultraviolet index and stratosphere-to-troposphere ozone flux". In: *Nature Geoscience* 2.10, pp. 687–691. DOI: [10.1038/ngeo604](https://doi.org/10.1038/ngeo604). URL: <http://dx.doi.org/10.1038/ngeo604>.
- AIRS3STD (2013). DOI: [doi:10.5067/AQUA/AIRS/DATA303](https://doi.org/10.5067/AQUA/AIRS/DATA303).
- Alexander, S. P., D. J. Murphy, and A. R. Klekociuk (2013). "High resolution VHF radar measurements of tropopause structure and variability at Davis, Antarctica (69?? S, 78?? E)". In: *Atmospheric Chemistry and Physics* 13.6, pp. 3121–3132. ISSN: 16807324. DOI: [10.5194/acp-13-3121-2013](https://doi.org/10.5194/acp-13-3121-2013). URL: <http://www.atmos-chem-phys.net/13/3121/2013/>.
- Dee, D P et al. (2011). "The ERA-Interim reanalysis: configuration and performance of the data assimilation system". In: *Quarterly Journal of the Royal Meteorological Society* 137.656, pp. 553–597. ISSN: 1477-870X. DOI: [10.1002/qj.828](https://doi.org/10.1002/qj.828). URL: <http://dx.doi.org/10.1002/qj.828>.
- WMO, World Meteorological Organization (1957). "Meteorology A Three-Dimensional Science". In: *Geneva, Second Session of the Commission for Aerology* 4, pp. 134–138.
- Bethan, S., G. Vaughan, and S. J. Reid (1996). "A comparison of ozone and thermal tropopause heights and the impact of tropopause definition on quantifying the ozone content of the troposphere". In: *Quarterly Journal of the Royal Meteorological Society* 122.532, pp. 929–944. ISSN: 00359009. DOI: [10.1002/qj.49712253207](https://doi.org/10.1002/qj.49712253207). URL: <http://doi.wiley.com/10.1002/qj.49712253207>.
- Tomikawa, Yoshihiro, Yashiro Nishimura, and Takashi Yamanouchi (2009). "Characteristics of Tropopause and Tropopause Inversion Layer in the Polar Region". In: *SOLA* 5, pp. 141–144. DOI: [10.2151/sola.2009-036](https://doi.org/10.2151/sola.2009-036). URL: <http://dx.doi.org/10.2151/sola.2009-036>.
- Jaffe, Daniel a. and Nicole L. Wigder (2012). "Ozone production from wildfires: A critical review". In: *Atmospheric Environment* 51, pp. 1–10. ISSN: 13522310. DOI: [10.1016/j.atmosenv.2011.11.063](https://doi.org/10.1016/j.atmosenv.2011.11.063). URL: <http://dx.doi.org/10.1016/j.atmosenv.2011.11.063>.
- Pak, B.C.a et al. (2003). "Measurements of biomass burning influences in the troposphere over southeast Australia during the SAFARI 2000 dry season campaign". In: *Journal of Geophysical Research D: Atmospheres* 108.13, SAF 16–1 –SAF 16–10. ISSN: 0148-0227. DOI: [10.1029/2002JD002343](https://doi.org/10.1029/2002JD002343). URL: <http://www.scopus.com/inward/record.url?eid=2-s2.0-0742322536&partnerID=40&md5=cafaf03b948fb456696583ed3ab9a5>.
- Sinha, Parikhit et al. (2004). "Transport of biomass burning emissions from southern Africa". In: *Journal of Geophysical Research* 109, p. D20204. ISSN: 01480227. DOI: [10.1029/2004JD005044](https://doi.org/10.1029/2004JD005044).
- Edwards, D. P. (2003). "Tropospheric ozone over the tropical Atlantic: A satellite perspective". In: *Journal of Geophysical Research* 108.D8, p. 4237. ISSN: 0148-0227. DOI: [10.1029/2002JD002927](https://doi.org/10.1029/2002JD002927). URL: <http://doi.wiley.com/10.1029/2002JD002927>.

- Edwards, D. P. et al. (2006). "Satellite-observed pollution from Southern Hemisphere biomass burning". In: *Journal of Geophysical Research Atmospheres* 111.14, pp. 1–17. ISSN: 01480227. DOI: [10.1029/2005JD006655](https://doi.org/10.1029/2005JD006655).
- Mari, C H et al. (2008). "Tracing biomass burning plumes from the Southern Hemisphere during the AMMA 2006 wet season experiment, Atmos". In: *Atmospheric Chemistry and Physics* 8, pp. 3951–3961. ISSN: 1680-7324. DOI: [10.5194/acpd-7-17339-2007](https://doi.org/10.5194/acpd-7-17339-2007).
- Bey, Isabelle et al. (2001). "Global Modeling of Tropospheric Chemistry with Assimilated Meteorology: Model Description and Evaluation". In: *Journal of Geophysical Research* 106, pp. 73–95. ISSN: 0148-0227. DOI: [10.1029/2001JD000807](https://doi.org/10.1029/2001JD000807).
- Eastham, Sebastian D., Debra K. Weisenstein, and Steven R H Barrett (2014). "Development and evaluation of the unified tropospheric-stratospheric chemistry extension (UCX) for the global chemistry-transport model GEOS-Chem". In: *Atmospheric Environment* 89, pp. 52–63. ISSN: 13522310. DOI: [10.1016/j.atmosenv.2014.02.001](https://doi.org/10.1016/j.atmosenv.2014.02.001). URL: <http://dx.doi.org/10.1016/j.atmosenv.2014.02.001>.
- Guenther, A. B. et al. (2012). "The model of emissions of gases and aerosols from nature version 2.1 (MEGAN2.1): An extended and updated framework for modeling biogenic emissions". In: *Geoscientific Model Development* 5.6, pp. 1471–1492. ISSN: 1991959X. DOI: [10.5194/gmd-5-1471-2012](https://doi.org/10.5194/gmd-5-1471-2012).
- Lathière, J et al. (2006). "Impact of climate variability and land use changes on global biogenic volatile organic compound emissions". In: *Atmospheric Chemistry and Physics* 6.2003, pp. 2129–2146. ISSN: 16807324. DOI: [10.5194/acp-6-2129-2006](https://doi.org/10.5194/acp-6-2129-2006). URL: [www.atmos-chem-phys.net/6/2129/2006/](http://www.atmos-chem-phys.net/6/2129/2006/).
- Winters, Anthony J. et al. (2009). "Emissions of isoprene, monoterpene and short-chained carbonyl compounds from Eucalyptus spp. in southern Australia". In: *Atmospheric Environment* 43.19, pp. 3035–3043. ISSN: 13522310. DOI: [10.1016/j.atmosenv.2009.03.026](https://doi.org/10.1016/j.atmosenv.2009.03.026).
- Wolfe, G M et al. (2016). "Formaldehyde production from isoprene oxidation". In: *Atmospheric Chemistry and Physics* x, pp. 2597–2610. DOI: [10.5194/acp-16-2597-2016](https://doi.org/10.5194/acp-16-2597-2016).
- Fortems-Cheiney, A. et al. (2012). "The formaldehyde budget as seen by a global-scale multi-constraint and multi-species inversion system". In: *Atmospheric Chemistry and Physics* 12.15, pp. 6699–6721. ISSN: 16807316. DOI: [10.5194/acp-12-6699-2012](https://doi.org/10.5194/acp-12-6699-2012).
- Atkinson, Roger and Janet Arey (2003). "Gas-phase tropospheric chemistry of biogenic volatile organic compounds: A review". In: *Atmospheric Environment* 37.SUPPL. 2. ISSN: 13522310. DOI: [10.1016/S1352-2310\(03\)00391-1](https://doi.org/10.1016/S1352-2310(03)00391-1).
- Lee, Anita et al. (2006). "Gas-phase products and secondary aerosol yields from the photooxidation of 16 different terpenes". In: *Journal of Geophysical Research Atmospheres* 111.17, pp. 1–18. ISSN: 01480227. DOI: [10.1029/2006JD007050](https://doi.org/10.1029/2006JD007050).
- Guenther, Alex. MEGAN. URL: <http://lar.wsu.edu/megan/>.
- Müller, J.-F. et al. (2008). "Global isoprene emissions estimated using MEGAN ECMWF analyses and a detailed canopy environment model". In: *Atmospheric Chemistry and Physics Discussions* 7.6, pp. 15373–15407. DOI: [10.5194/acpd-7-15373-2007](https://doi.org/10.5194/acpd-7-15373-2007). URL: <http://dx.doi.org/10.5194/acpd-7-15373-2007>.
- Kurosu, T and K Chance (2014). OMIReadme. URL: [https://www.cfa.harvard.edu/atmosphere/Instruments/OMI/PGEReleases/READMEs/OMHCHO\\_README\\_v3.0.pdf](https://www.cfa.harvard.edu/atmosphere/Instruments/OMI/PGEReleases/READMEs/OMHCHO_README_v3.0.pdf).
- Palmer, Paul I et al. (2001). "Air mass factor formulation for spectroscopic measurements from satellites' Application to formaldehyde retrievals from the Global Ozone Monitoring Experiment". In: 106.

- Wikipedia. *Solar zenith angle*. DOI: [10.1016/B978-012369407-2/50005-X](https://doi.org/10.1016/B978-012369407-2/50005-X). URL: <http://sacs.aeronomie.be/info/sza.php>.
- De Smedt, I. et al. (2012). "Improved retrieval of global tropospheric formaldehyde columns from GOME-2/MetOp-A addressing noise reduction and instrumental degradation issues". In: *Atmospheric Measurement Techniques* 5.11, pp. 2933–2949. ISSN: 18671381. DOI: [10.5194/amt-5-2933-2012](https://doi.org/10.5194/amt-5-2933-2012).
- De Smedt, I. et al. (2015). "Diurnal, seasonal and long-term variations of global formaldehyde columns inferred from combined OMI and GOME-2 observations". In: *Atmospheric Chemistry and Physics* 15.21, pp. 12519–12545. ISSN: 16807324. DOI: [10.5194/acp-15-12519-2015](https://doi.org/10.5194/acp-15-12519-2015). URL: <http://www.atmos-chem-phys-discuss.net/15/12241/2015/> \n<http://www.atmos-chem-phys-discuss.net/15/12241/2015/acpd-15-12241-2015.pdf>.
- Gonzalez Abad, G. et al. (2015). "Updated Smithsonian Astrophysical Observatory Ozone Monitoring Instrument (SAO OMI) formaldehyde retrieval". In: *Atmospheric Measurement Techniques* 8.1, pp. 19–32. ISSN: 18678548. DOI: [10.5194/amt-8-19-2015](https://doi.org/10.5194/amt-8-19-2015).
- Bauwens, Maite et al. (2016). "Nine years of global hydrocarbon emissions based on source inversion of OMI formaldehyde observations". In: *Atmospheric Chemistry and Physics Discussions* March, pp. 1–45. ISSN: 1680-7375. DOI: [10.5194/acp-2016-221](https://doi.org/10.5194/acp-2016-221). URL: <http://www.atmos-chem-phys-discuss.net/acp-2016-221/>.
- Zhu, Lei et al. (2016). "Observing atmospheric formaldehyde (HCHO) from space: validation and intercomparison of six retrievals from four satellites (OMI, GOME2A, GOME2B, OMPS) with SEAC<sup>4</sup>RS aircraft observations over the Southeast US". In: *Atmospheric Chemistry and Physics Discussions* 0.March, pp. 1–24. ISSN: 1680-7375. DOI: [10.5194/acp-2016-162](https://doi.org/10.5194/acp-2016-162). URL: <http://www.atmos-chem-phys-discuss.net/acp-2016-162/>.
- Giglio, Louis, Ivan Csiszar, and Christopher O. Justice (2006). "Global distribution and seasonality of active fires as observed with the Terra and Aqua Moderate Resolution Imaging Spectroradiometer (MODIS) sensors". In: *Journal of Geophysical Research: Biogeosciences* 111.2, pp. 1–12. ISSN: 01480227. DOI: [10.1029/2005JG000142](https://doi.org/10.1029/2005JG000142).